ELECTROCHEMICAL SYSTEMS TO RECOVER LOW-GRADE WASTE HEAT FOR ELECTRICAL ENERGY GENERATION

CHENG CHUN

PhD

The Hong Kong Polytechnic University

2023

The Hong Kong Polytechnic University

Department of Building and Real Estate

Electrochemical Systems to Recover Low-grade Waste Heat for Electrical Energy Generation

CHENG Chun

A thesis submitted in partial fulfillment of the requirements for the degree of Doctor of Philosophy

November 2022

CERTIFICATE OF ORGINALITY

I hereby declare that this thesis is my own work and that, to the best of my knowledge and belief, it reproduces no material previously published or written, nor material that has been accepted for the award of any other degree or diploma, except where due acknowledgement has been made in the text.

_____ (Signed)

CHENG Chun (Name of student)

ABSTRACT

A considerable amount of waste heat from industrial facilities and solar radiation is discarded into the environment without being efficiently utilized every year. A large proportion of this waste heat is low-grade waste heat, commonly defined as heat with temperatures below 150ºC. Therefore, numerous approaches to generate electricity from low-grade waste heat have been emerging to better take advantage of low-grade waste heat over the past few decades, most of which are liquid-based electrochemical approaches.

Thermally regenerative electrochemical cycles (TREC) are one of the promising liquid-based electrochemical systems for converting low-grade heat to electrical power. In this thesis, the TREC with nickel hexacyanoferrate (NiHCF) cathode and Zn anode achieves a markedly high thermopower (α) of -1.575 mV K^{-1} and a heat-to-electricity efficiency of 2.41% at the temperature difference of 30℃ (equivalent to 25.15% of Carnot efficiency), surpassing all the existing TREC systems. For the first time, the mixed membranes with mixed pH electrolytes are introduced into the TREC systems to boost α to a record-high value of -2.270 mV K^{-1}. The proposed thermodynamic framework advances the understanding of the origin of α and electrochemical potential, which will guide people to engineer TRECs. By looking more deeply into the optimization in both thermopower and device design, the resultant efficiency is excellent but the power density of TREC is still unsatisfactory. Additionally with the discontinuous operation through a TREC, practical application of TREC is impeded. To

address these challenges, efforts should be made to develop novel approaches possessing high power density, reliable and flexible assembly, and long-standing discharging times.

Considering the current primary energy generation systems also produce a significant amount of waste CO_2 coupled with low-grade heat, this study also proposes a thermally regenerative CO_2-induced pH-gradient cell (TRCPC) that simultaneously utilizes CO_2 and low-grade heat for waste to electricity conversion. CO_2 is absorbed in one side of the symmetric electrolyte and causes a change in the pH of the cell to induce voltage generation, achieving a peak power density of 0.578 W m^{-2} (~ 10 times that of TREC). After discharging, the system can be regenerated using low-grade heat while the CO_2 can then be stored and transported. This research proposes a promising way for economic and environmental benefits to exploit CO_2 and waste heat into electricity before further CO_2 storage.

However, the power density and discharging time of TRCPC are limited by the sluggish kinetics of electrodes and unoptimized cell design. By replacing the electrode with an H_2/H^+ catalytic electrode and rationally improving the cell design, we further investigate an advanced pH-sensitive thermally regenerative cell (pH-TRC) with circulating hydrogen to achieve both long discharging time and high-power output. Between the H_2/H^+ catalytic electrodes, we have flowing anolyte and catholyte with various pH values, which can be neutralized through discharging reactions and then thermally regenerated to reset the initial state. The underlying mechanism of pH-TRC, kinetics, open circuit voltage (OCV) generation, cell design, and parameter study are scrutinized both computationally and experimentally verified. With this new design and the intrinsically faster kinetics of H_2/H^+ catalytic electrodes, a favorable peak

power density of 5.296 W m^{-2} (approximately 10 times TRCPC) is obtained. More importantly, an incredibly long discharging time of over 40 hours enables the powering of a smartphone in comparison to only hundreds-of-seconds discharging time of previous TRCPC.

This work presents a comprehensive study of new methods for low-grade waste heat harvesting, particularly in practical industrial applications. In our first attempt to generate electricity in a TREC, the intrinsic energy conversion mechanism including the thermodynamics and kinetics processes are discussed in detail. In approaching the emerging issues of TREC, TRCPC and pH-TRC are subsequently proposed, where the design strategy and underlying mechanism are fully studied in this thesis, which helps to establish effective follow-up industrial implementations aimed at thermal energy conversion.

AUTHOR'S PUBLICATIONS

1. **Cheng, C**. et al. pH-sensitive thermally regenerative cell (pH-TRC) with circulating hydrogen for long discharging time and high-power output. Chemical Engineering Journal 449, 137772 (2022).

2. **Cheng, C**. et al. Numerical Study of Electrochemical Thermocells for Harvesting Low-grade Waste Heat. HKIE (2022).

3. **Cheng, C**. et al. Thermally Regenerative CO_2 -Induced pH-Gradient Cell for Waste-to-Energy Conversion. ACS Energy Letters. 6, 3221–3227 (2021).

4. **Cheng, C**. et al. Review of Liquid-Based Systems to Recover Low-Grade Waste Heat for Electrical Energy Generation. Energy&Fuels 35, 161–175 (2021).

5. **Cheng, C**. et al. Insights into the Thermopower of Thermally Regenerative Electrochemical Cycle for Low-Grade Heat Harvesting. ACS Energy Letters. 329–336 (2020).

ACKNOWLEDGEMENTS

I would like to express my gratitude to all those who help me during my Ph.D. study. I would like to show my heartfelt gratitude to my chief supervisor, Professor NI Meng, for his constructive suggestions, strong support, and warm encouragement. To me, he is more than a teacher because he cares about us as friends. His insightful suggestions, and upbeat attitude gave me unprecedented determination, courage, and passion to confront any difficulties in life and in work. His tolerance, understanding, and respect for students allowed me more freedom and opportunities to try out different approaches and lifestyles. He was unstintingly generous with his resources, time, and experiences to help his students. Under his guidance, I gradually grew into a qualified research student, moreover, an independent, and mature adult. I am delighted to be one of his Ph.D. students. In my opinion, he is the best teacher I have ever met.

I would like to extend my sincere gratitude to my co-supervisor, Professor FENG Shien-Ping, for all his kindness and help. I am deeply grateful for his helpful discussion, and theoretical insights, especially his kind sharing of laboratory resources, otherwise my research would not have gone smoothly. I have learned a lot from him. Every time I heard or witnessed his setbacks in his life, I was overwhelmed by his strength and resilience in the face of difficulties. I believe his inner charisma and critical scientific manner have influenced each of his Ph.D. students and will benefit them for life.

I also gratefully acknowledge the help from Professor TAN Peng from the University of Science and Technology of China. During the challenging time of the COVID-19 pandemic,

he provided me with crucial support in accessing laboratory facilities, which was instrumental in the successful completion of my research. I am deeply grateful for his kindness and generosity, and I will always remember his invaluable contribution to my Ph.D. study.

Thanks to all my group mates for their help in experiments, analysis, and spiritual encouragement. They are Dr. Yawen Dai, Dr. GUO Meiting, Dr. YU Jie, Dr. ZHANG Zhenbao, Dr. LIU Tong, Dr. GUAN Daqin, Dr. ZHANG Zhiqi, Dr. HUANG Zhenhua, Dr.LIN Xuemei, Dr. CHENG Rui, Dr. WANG Xun, XU Qidong, HE Qijiao, XIA Lingchao, LI Zheng, YU Na, WANG Chen, ZHAO Siyuan, HE Qun, CHEN Cong, WU Xinya and PANG Chunlin.

I appreciate the emotional support, understanding and admission from my close friends, BAO Sijia, ZHANG Wenzhuo, WANG jin, ZHANG Yanlin and TANG Yucan.

I would like to express my deep gratitude to my best friend and colleague, WANG Sijia. Her wise analysis, inspiring advice, and warm comfort enlighten me not only in research but also in my future study and life.

Special thanks should go to my family for their unwavering love and solid support. I am especially grateful to my mother for taking care of me when I was sick. Her selflessness, sacrifice, and boundless love have instilled in me the confidence to love and be loved.

Finally, I would like to express my gratitude to my best friend, soulmate, and "comrade" in life, CHEN Wei, who is incredibly talented in engineering. His intelligence has helped me overcome every research difficulty and expand the frontiers of knowledge. His warm company is the longest confession of love.

TABLE OF CONTENTS

ABSTRACT ..... **I**

AUTHOR'S PUBLICATIONS ..... **IV**

ACKNOWLEDGEMENTS ..... **V**

TABLE OF CONTENTS ..... **VII**

LIST OF FIGURES ..... **X**

LIST OF TABLES ..... **XVII**

LIST OF ABBREVIATIONS ..... **XVIII**

CHAPTER 1 Introduction **1**

1.1 Background 1

1.2 Research Objectives 4

1.3 Outline of This Thesis 7

CHAPTER 2 Literature Review **9**

2.1 TECs (thermos-electrochemical cells) 9

2.2 Thermally Regenerative Electrochemical Cycles (TRECs) 23

2.2.1 Non-metal Solid Electrode 27

2.2.2 Redox Flow Batteries (RFBs) 32

2.2.3 Thermal Regenerative Ammonia-based Batteries (TRABs) 35

2.2.4 Electrical Double-layer-based Cycle 40

2.2.5 Direct Thermal Charging Cell (DTCC) 41

2.3 Thermo-osmotic Energy Conversion (TOEC) 42

2.4 Summary and Perspectives 44

CHAPTER 3 Methodology **48**

3.1 Evaluation of The Efficiency and Power Density 48

3.2 Material Characterization 49

3.3 Performance Test of TREC, TRCPC and pH-TRC system 49

CHAPTER 4 Investigations in TREC of High Thermopower 51

4.1 Introduction 51

4.2 Experimental Section 52

4.2.1 Experimental Overview 52

4.2.2 Electrode preparation 53

4.2.3 Cell Fabrication 54

4.2.4 Temperature Control 55

4.3 Optimizations in Thermopower 56

4.4 Effects of Temperature 70

4.5 Performances 74

4.6 Conclusions 84

CHAPTER 5 Thermally Regenerative CO_2-induced PH-Gradient Cell for Waste to Energy Conversion 86

5.1 Introduction 86

5.2 Experimental Section 89

5.2.1 Experimental Overview 89

5.2.2 Synthesis of the MnO_2 Powder 90

5.2.3 Preparation of the Electrodes 91

5.2.4 Fabrication of the Cell 91

5.2.5 Flow Rate 92

5.2.6 XPS 92

5.3 Requirements of TRCPC 93

5.4 Performances of TRCPC 97

5.5 Theoretical Analysis 103

5.5.1 Effect of Na^+ 103

5.5.2 Effect of Ion Concentration 105

5.5.3 Calculation of Efficiency in TRCPC 106

5.6 Conclusions 112

CHAPTER 6 PH-Sensitive Thermally Regenerative Cell (pH-TRC) with Circulating Hydrogen 113

6.1 Introduction 113

6.2 Experimental Section 116

6.2.1 Experimental Overview 116

6.2.2 Preparation of Pt/C Electrodes 117

6.2.3 PH-TRC System Configuration and Operation 117

6.2.4 Characterization 119

6.3 OCV Generation 119

6.4 Working Characteristics of PH-TRC 124

6.5 System Stability and Effect of Operation Temperature 127

6.6 Effect of Flow Rate and Supporting Electrolyte 131

6.7 PH-TRC Efficiency Calculation 138

6.8 Challenges and Future Perspectives of PH-TRC 141

6.9 Conclusions 142

CHAPTER 7 Conclusions and Outlook 144

7.1 Conclusions 144

7.2 Outlook 146

REFERENCES 149

LIST OF FIGURES

Figure 1.1. Research overview of these three works. 6

Figure 2.1. Power generation of the cell using 24 M urea and 2.6 M GdmCl with cyanide electrolyte. Reprinted with permission from ref. 18. Copyright 2018 Nature. 17

Figure 2.2. The thermopower of thermoelectric materials for both p-type and n-type. Reprinted with permission from ref. 9. Copyright 2015 Royal Society of Chemistry. 20

Figure 2.3. Comparison of low-grade thermal energy conversion approaches, **a)** The power density and efficiency relative to the Carnot **b)** The research time of different approaches, TEC with platinum (TEC-Pt)[53] or with carbon nanotube electrodes (TEC-CNT); [36,37,44,54] SGE (salinity gradient energy) systems including RED (reverse electro-dialysis)[55–58] and PRO (pressure retarded osmosis);[59,60] TREC; [51] TRB[61, 62] and TOEC.[63,64] Reprinted with permission from ref. 48. Copyright 2018 Royal Society of Chemistry.....26

Figure 2.4. Schematic of the battery design, 0.5 M $K_3Fe(CN)_6$/0.1 M $K_4Fe(CN)_6$ (catholyte) versus 0.1 M I_2/2 M KI (anolyte). Reprinted with permission from ref. 52. Copyright 2019 Royal Society of Chemistry. 30

Figure 2.5. The structure of VRFB. Reprinted with permission from ref. 72. Copyright 2019 Elsevier. 33

Figure 2.6. The principle for harvesting heat of VRFB, **a)** The temperature-entropy plot for a TREC when thermopower is negative **b)** The thermodynamic cycle of TREC-VRFB system. Reprinted with permission from ref. 73. Copyright 2018 Elsevier.....33

Figure 2.7. The closed-cycle system for TRAB. Reprinted with permission from ref. 61. Copyright 2015 Royal Society of Chemistry. 36

Figure 2.8. a) A supercapacitor model with two parallel plates. **b)** The open-circuit potential change when cycling the fully charged cell between 0 and 65 °C. Reprinted with permission from ref. 91. Copyright 2015 Royal Society of Chemistry.....40

Figure 2.9. Working principle of TOEC system, a, Schematic diagram of water vapour transport across a membrane, b, Hydraulic pressure that can be theoretically generated with a certain temperature difference across a membrane. Reprinted with permission from ref. 63. Copyright 2018 Royal Society of Chemistry. 43

Figure 4.1. The cell fabrication**. a)** The assembled pouch cell to test thermopower with K_2SO_4 electrolyte. **b)** The cell fabrication: the battery shell is made of 4×5 cm polypropylene (PP) membrane and sealant is applied along the edges. Filter paper is set under the electrode in order to absorb the electrolyte. Catholyte and anolyte are injected by needle tube after sealing membrane. **c)** The totally sealed device with CEM and AEM inside. **d)** The cell with sealed method by silicone pad, fluoro-rubber and Vaseline. 55

Figure 4.2. Working diagram of TREC and α performance of cathode, anode and the cell. **a)** The four steps working principle of TREC and the discharging reaction of NiHCF/Zn and NiHCF/ZnNH_3 system. **b)** The cathode voltage response to the temperature from 0℃ to 40℃. **c)** The NiHCF, Zn vs. RE (AgCl/Ag) and full cell voltage difference change with temperature difference of 30℃. 1 represents NiHCF/K_2SO_4/Zn system, 2 represents NiHCF/ K_2SO_4//NH_3+$(NH_4)_2SO_4$ +$ZnSO_4$/Zn system. **d)** The comparison on absolute α value of different systems including CuHCF/Cu, [47] NiHCF/AgCl, [48] CoHCF/pp[98] and LMO/CuHCF,[72] green marked bars are our work..... 56

Figure 4.3. Morphology of NiHCF powder. **a)** The SEM image of NiHCF power after settling down overnight. **b)** The SEM image of grinding NiHCF particle with carbon black and binder (PVDF). 57

Figure 4.4. The entropy change and energy change of discharging electrochemical reaction. **a)** Schematic diagram of entropy and energy change of the reaction. **b)** α change of NiHCF and Zn electrode among the 10℃ to 60℃ temperature range. **c)** Overall heat capacity change $\Delta Cpreaction$ of cathode and anode reaction. **d)** Schematic diagram of temperature influence in reaction energy change. 62

Figure 4.5. Raman spectra of 0.5 M K_2SO_4 at 25℃ room temperature and 50℃..... 66

Figure 4.6. Pure water heat capacity change with temperature.[102] 66

Figure 4.7. The cyclic voltammetry (CV) curves of NiHCF in 0.5 M K_2SO_4 and kinetics parameters analysis in electrode reaction. **a)** The half CV curve of NiHCF from 10℃ to 40℃ with the sweeping speed of 1 mV s^{-1}. E_{eq} is the equilibrium potential, η_e is the overpotential controlled by charge transfer step. **b)** The various potentials of NiHCF from 10℃ to 40℃. $E^{\theta'}$, E_{pH} and E_{pL} represent formal potential, high and low peak voltage respectively, the sweeping speed is 1 mV s^{-1}. **c)** The linear fitting to extrapolate exchange current density from 10℃ to 40℃. The overpotential can be expressed linearly to lg j where j is current density. The intercept on the x axis represents lg j_0, j_0 is exchange current density. **d)** The obtained exchange current density from **Figure 4.7c** and peak current from **Figure 4.7a**. 71

Figure 4.8. The XRD pattern of NiHCF particles. **a)** The XRD pattern of NiHCF, indicating its face-centered cubic Fm-3m space group. **b)** The (400) and (420) peak shift with temperature from 10℃ to 60℃. 73

Figure 4.9. The full cell performance with NiHCF cathode and Zn anode. **a)** The voltage change for the whole cell during a full TREC cycle. The NiHCF-Zn cell was operated between 10℃ to 40℃ at a current density of 5.4 mA g^{-1}, including C-1 heating up, C-2 charging, C-3 cooling down, and C-4 discharging. **b)** The voltage change for the whole cell during a full TREC cycle. The NiHCF-$ZnNH_3$ cell was operated between 10℃ to 40℃ at a current density of 5.4 mA g^{-1}. **c)** The full NiHCF/Zn cell capacity plot versus voltage of the whole cycle consistent to Figure 2.6a and b. The corresponding energy density is 5.8346 J g^{-1} (per electrode mass). The full NiHCF/$ZnNH_3$ cell capacity plot versus charging-discharging voltage with 0.1 C current density (5.4 mA g^{-1}) which is as same as the charging-discharging condition as NiHCF-Zn. The corresponding energy density is 9.8912 J g^{-1} (per electrode mass). **d)** The relative efficiency, efficiency, energy density and harvested output power of 0.1 C, 0.15 C, 0.2 C current density with 5.4 mA g^{-1}, 8.1 mA g^{-1}, 10.8 mA g^{-1} within 10℃ to 40℃ temperature range (ηHR=0). 1 represents NiHCF/Zn system. **e)** The relative efficiency, efficiency, energy density and harvested output power at current of 0.1 C (5.4 mA g^{-1}), 0.5 C (27.0 mA g^{-1}), 1 C

(54.0 mA g^{-1}), 1.5 C (81 mA g^{-1}) and at temperature gap of 30°C (10°C to 40°C) (ηHr= 0). 2 represents NiHCF/$ZnNH_3$ system. **f)** The performance comparison including efficiency, relative efficiency and α. The systems include CuHCF/Cu, [47] NiHCF/AgCl, [48] CoHCF/pp[98] and LMO/CuHCF.[72] **g)** The relative efficiency and power density of different systems. 75

Figure 4.10. The performance of NiHCF/Zn system (from 80% SOC to 100% SOC). **a)** The TREC cycle with 30℃ temperature difference at 5.4 mA g^{-1} (0.1 C). **b)** The TREC cycle with 30℃ temperature difference at 8.1 mA g^{-1} (0.15 C). **c)** The TREC cycle with 30℃ temperature difference at 10.8 mA g^{-1} (0.2 C). **d)** The power density at different current density. **e)** The relative efficiency and absolute efficiency ($\boldsymbol{\eta HR = 0}$) at different current density. 77

Figure 4.11. The cycle life of NiHCF/K_2SO_4/Zn system. **a)** The TREC cycle life with 30℃ temperature difference at 5.4 mA g^{-1} (0.1 C). The 50 cycles with 30℃ temperature difference at 5.4 mA g^{-1} current density, the cell is fully charged and discharged. The cycling end discharging voltage is 0.65 V and the end charging voltage is 1.6 V. **b)** The relative efficiency, absolute efficiency ($\boldsymbol{\eta HR = 0}$) and coulomb efficiency of 50 cycles. 78

Figure 5.1. Schematic of the cell components and operation of the proposed heat-induced CO_2-based electrochemical cycle. **a)** Mechanism of the TRCPC. **b)** Structure of a TRCPC cell. Two 10 cm silicone tubes (ϕ 1.5×0.25 mm) were sealed in PMMA frame with two corresponding 2 mm air vents. The electrodes and anion exchange membrane are separated by two silicone sheets. One-third of the cell is left empty to prevent overflow of the 0.5 M Na_2CO_3 electrolyte. 88

Figure 5.2. Fabrication of the cell. **a)** The components of the cell. **b)** The complete cell after fabrication. Two 10 cm silicone tubes were sealed in PMMA frame with two corresponding 1.5 mm air vents. The electrodes and anion exchange membrane are separated by two silicone sheets. One-third of the cell is left empty to prevent overflow of the 0.5 M Na_2CO_3 electrolyte. 92

Figure 5.3. The schematic of CO_2-induced voltage. **a)** Systematic diagram of the CO_2 cycle in the cell at hot temperature (HT) and room temperature (RT). **b)** Open circuit potential before,

during, and after CO_2 pumping. The flow rate of CO_2 is 2 mL min^{-1}, the overall volume of CO_2 is 60 mL. **c)** $MnOOH/MnO_2$ electrode potential and pH versus $NaHCO_3$ molar percentage in $NaHCO_3/Na_2CO_3$ solution. The remaining total $c(Na^+)$ is 1 M. **d)** $MnOOH/MnO_2$ electrode potential versus pH value. 95

Figure 5.4. a) CV curves of $MnOOH/MnO_2$ electrode in 0.5 M Na_2CO_3 electrolyte at a scanning rate of 50 mV s^{-1}. The $c(Na^+)$ is maintained at 1 M. **b)** SEM image of MnO_2 particles on the electrode. **c)** XPS survey spectrum of $MnOOH/MnO_2$ electrode and the narrow XPS spectrum of **d)** Mn 2p, **e)** O 1s corresponding to different reduction states. 96

Figure 5.5. a) Current-potential curve and corresponding power density output with 2 mL min^{-1} and 20 mL CO_2 pumping. **b)** Potential-time curve during discharging with a constant current of 1 mA after establishing the potential of 20 mL and 60 mL CO_2 respectively. **c)** 30 cycles of CO_2 charging and 1 mA discharging (2 mL min^{-1}, 20 mL) whose potential changes are compared with the control group of pure $NaHCO_3$. **d)** the discharging performance of the reversed electrode. The electrode was reversed after the previous charge-discharge cycle. ... 99

Figure 5.6. Heat regenerative electrolyte. **a)** The pH changes of the 1 M $NaHCO_3$ towards time under the 70℃ and 90℃ environmental temperature. **b)** The demonstration of decomposition of 1 M $NaHCO_3$ solution which is sealed in a glass container under the 90℃ environmental temperature. The continuous bubbles in the cell are decomposed CO_2 gas. **c)** The discharging performance with 10 Ω resistance. 102

Figure 5.7. Potential change of $MnOOH/MnO_2$ electrode in **a)** Na_2CO_3-$NaHCO_3$ solution with consistent $c(Na^+)$ = 1 M, **b)** in NaCl solution with consistent $c(H^+) \approx 10^{-6.06}$. Energy dispersive spectroscopy (EDS) elemental mapping images showing the distribution of Mn and Na on, **c)** and **d)**, reference electrode immersed in 1 M $NaHCO_3$ solution. **e)** and **f)**, working electrode in TRCPC. **g)** and **h)**, counter electrode in TRCPC. 104

Figure 5.8. The energy balance diagram of TRCPC. 107

Figure 5.9. Cycle performance of one complete electrolyte conversion. **a)** Charge-discharge curve of 30 cycles. **b)** The average discharge voltage for each cycle. 107

Figure 5.10. The theoretical calculated results of **a)** ΔpHn and **b)** En during electron transfer, corresponding to 1 L catholyte/anolyte. **c)** Ion movements during discharge. 109
Figure 6.1. Working mechanism of pH-TRC to convert heat into electricity. **a)** Schematic of typical TRC; **b)** Schematic of pH-TRC; **c)** Single cell structure of pH-TRC.....116
Figure 6.2. Open circuit voltage (OCV) change in pH-TRC. **a)** The OCV and **b)** pH difference change with electron transfer during discharging; **c)** OCV of cell, **d)** anode and **e)** cathode change by hydrogen supply; **f)** Voltage change with electrolyte state. 123
Figure 6.3. Results in power. **a-c)** LSV results of anode and cathode at sweep speed of 5 mV s^{-1}; **d)** Power density of a single cell pH-TRC (electrolyte flow rate: 40 mL min-1, gas flow rate: 5 mL min-1); **e-f)** Demonstrations of pH-TRC powering a smart phone and LED array. 126
Figure 6.4. Discharging performance at room temperature and higher temperature. **a)** Discharging curve with 1.2 mL anolyte and 2 L catholyte at room temperature; **b)** Mechanism of pH value change of electrolytes during discharging, and comparison of anolyte and catholyte after long-time discharging; **c)** Calculated pH value change of electrolytes during discharging; **d)** Discharging curve with 50 mL anolyte and 50 mL catholyte at room temperature; **e)** Comparison of energy density with different electrolyte volume and temperature; **f)** Power densities with different temperatures; **g)** A discharging curve with equal volume of 50 mL of electrolytes at 50 Celsius; **h)** Gas chromatography curve of discharging product from catholyte. 130
Figure 6.5. Effects of flow rate, supporting electrolyte and exchange current density of anode. Comparison of experimental and computational power densities with **a)** various working voltage, **b)** different gas flow rate, and **c)** different electrolyte flow rate; **d)** Powers generated by a pH-TRC of 2×2 cm electrode area under different discharging current, where pumping powers under various electrolyte flow rate are plotted in dash line, suggesting a reasonable

flow rate under a certain discharging current; **e)** Power density changes with exchange current densities of anode and **f)** a range of concentrations of supporting electrolyte.....137
Figure 7.1. Research overview of these three works. 145

LIST OF TABLES

Table 2.1. Thermopower α of typically different redox couples. 12

Table 2.2. The comparison of parameters in various system. 37

Table 4.1. The experimental information. 52

Table 4.2. The meaning and unit of referred physical quantities. 69

Table 4.3. The information of parameters related to performances. 74

Table 4.4. The performance comparison. Parameters include α, temperature difference ΔT, energy density W, efficiency η, relative efficiency ηr and recuperation efficiency ηHR. The systems include CuHCF/Cu, [47] NiHCF/AgCl, [48] CoHCF/pp[98] and LMO/CuHCF.[72] 79

Table 4.5. Performance comparison among different systems. 82

Table 5.1. The experimental information. 89

Table 5.2. The average discharging voltage U and time *t* in the cycling experiments. The inlet of CO_2 is 20 mL per cycle. The discharging current *I* is 1 mA. 108

Table 6.1. The experimental information. 117

Table 6.2. The experimental information. 119

Table 6.3. Parameters used in this model. 133

Table 6.4. The overall pump powers (anolyte and catholyte) related to flow rates. 139

Table 6.5. The efficiency results by applying heat exchange. 141

LIST OF ABBREVIATIONS

ACE	Anode coulombic efficiency
AEM	Anion exchange membrane
AM	Acrylamide
AMPS	2-acrylamide-2-methylpropane sulfonic acid
CCS	Carbon capture and storage
CEE	Cathode coulombic efficiency
CEM	Cation exchange membrane
CoHCF	Cobalt hexacyanoferrate
Cu/Zn – TRAFB	copper/zinc bimetallic thermally-regenerative ammonia-based battery
CuHCF	Copper hexacrynoferrate
DTCC	Direct thermal charging cell
EAN	Ethylammonium nitrate
EIS	Electrochemical impedance spectroscopy
FTIR	Fourier-transsform infrared spectroscopy
GdmCl	Guanidinium chloride
GO	Graphene oxide
HER	Hydrogen evolution reaction
HOR	Hydrogen oxidation reaction
LMO	Lithium manganese oxide
LSV	Linear scan voltammetry
MWNT	Multi-walled carbon nanotubes
NiHCF	Nickel hexacyanoferrate

NMP	1-Methyl-2-pyrrolidone
OCV	Open circuit voltage
PANI	Polyaniline
PBA	Prussian blue analogs
PFC	Perfluorochemicals
pH-TRC	PH-sensitive thermally regenerative cell
PMMA	Poly (methyl methacrylate)
pNIPAm	poly (N-isopropylacrylamide)
PPF	Poly(propylene fumarate)
PTFE	Polytetrafluoroethylene
PVA	Polyvinyl alcohol
PVDF	Polyvinylidene fluoride
QSPR	Quantitative structure–property relationship
RFBs	Redox flow batteries
rGO	Reduced graphene oxide
SEM	Scanning electron microscope
SOC	States of charge
SWNT	Single-walled carbon nanotube
TE	Thermoelectric
TECs	Thermo-electrochemical cells
TGCs	Thermogalvanic cells
TOEC	Thermo-osmotic energy conversion
TRABs	Thermal regenerative ammonia-based batteries
TRCPC	Thermally regenerative CO2-induced pH-Gradient cell

TRECs	Thermally regenerative electrochemical cycles
TRENB	Ethylenediamine-based battery
VRFB	All-vanadium redox flow battery
XPS	X-ray photoelectron spectroscopy
XRD	X-ray diffraction
α-CD	Cyclodextrins

CHAPTER 1 Introduction

1.1 Background

A huge amount of low-grade heat (<150ºC) from solar thermal, geothermal, and industrial facilities is heavily wasted every year. For example, the rejected energy accounted for 67.5% of the total energy consumption of the US in 2019.[1] Even worse, a large proportion of waste heat is low-grade heat.[2] For example, 92.4% of total waste heat from power plants was below 150ºC in 2007.[3] Also, all of the waste heat in food processing, and commercial and building sector almost belong to the low-grade waste heat.[3] In the UK, thermal energy accounts for 72% of industrial energy consumption, and low-temperature process accounts for 31%.[4] Thus, a large amount of waste heat is discarded without being utilized. How to effectively and economically recover low-grade heat is critical to enhance the overall energy efficiency and alleviate heat island effects for a sustainable future.

There are two main methods for converting low-grade waste heat into electrical power. The first one is based on the Seebeck effect of solid semiconductors, or even conducting polymer electrodes (PEDOT-PSS).[5–7] The other one mainly relies on the liquid-based entropy change electrochemical system like temperature-dependent redox couple to use heat as a driving force for power generation. In addition to these two main methods, some researchers

recently developed electrochemical sodium heat engines for thermal-to-electric energy conversion, which based on phase change reactions.[8]

The Seebeck effect was discovered by Thomas Johann Seebeck in the early 19th century. It was found that the electrical field was generated when connecting two different metal wires with different temperatures were applied to the two nodes. It was explained as thermoelectricity (Seebeck effect). This effect depends on the different thermal responses of different materials, that create a potential difference. For example, more holes are formed at the hot end of the p-type semiconductor, creating a hole gradient. As a result, holes tend to diffuse from the high concentration region (hot end) to the low concentration region (cold end) inside the material, establishing a potential difference. When a balance is reached between potential-caused current and thermal-induced current, a stable voltage can be formed between the two ends. However, the temperature-induced voltage of typical thermoelectric (TE) is generally at $\mu V\ K^{-1}$ level,[9] which is much lower than that of thermo-electrochemical cells (TECs) ($mV\ K^{-1}$). Moreover, the generated current density is small, resulting in a low power density. For example, the reported power density of flexible inorganic Ag_2S-based thermoelectric semiconductor material is only 0.08 $W\ m^{-2}$, and the power density of an organic thermoelectric device is even 2 orders of magnitude lower.[10] For comparison, the power density of liquid-based systems such as Cu/Zn–TRAFB (copper/zinc bimetallic thermally-regenerative ammonia-based battery) is much higher (280 $W\ m^{-2}$).[11] Additionally, the thermoelectric semiconductor materials require advanced manufacturing process, resulting in a high cost and difficulty in large scale commercial application. The average cost of thermoelectric semiconductor materials is

hundreds to thousands of dollars per kilogram, contributing to 50%-80% of the total cost of semiconductor-based thermoelectric devices.[12-13] Nowadays, some scientists focus on thermal photovoltaic conversion to harvest waste heat. The electrical power generated from a broadband blackbody thermal source was demonstrated with a maximum value, i.e. 0.61 W m^{-2} with a temperature difference of 150 ºC.[14] The optimization in power density, efficiency, and figure of merit is inherently constrained (which will be discussed below in detail) as the intrinsic properties such as Seebeck coefficient, thermal conductivity, and electrical resistivity are often coupled together. For comparison, the liquid-based electrochemical system avoids these problems and introduces more possible improvement approaches.

The liquid-based electrochemical systems rely on redox couples to carry charges in the electrolyte. Several liquid-based novel systems have been recently developed to harvest heat including TECs (thermo-electrochemical cells), TRECs (thermally regenerative electrochemical cycles), thermal regenerative ammonia-based batteries (TRABs), DTCC (direct thermal charging cell), and so on. These cells or cycles are based on early thermogalvanic cells (TGCs) and exhibit the features and merits of galvanic cells such as metal-ion batteries. Especially, TOEC (thermo-osmotic energy conversion) is based on the large salinity differences to generate power, which requires a robust membrane to create a pressurized flux (by a temperature difference) to drive a turbine for electric power generation. TRECs, TOEC, TRABs, and DTCC show significant advantages over other types of thermal-to-electric energy conversion technologies.

Despite numerous liquid-based electrochemical systems that have emerged, the current developing state of heat-to-electricity conversion based on liquid-based electrochemical systems is still far away from practical application. These liquid-based electrochemical systems are facing problems regarding efficiency, power density, and scalability. Therefore, newly designed systems are desired to make the practical implementation of heat-to-electricity conversion. Consequently, new strategies for exploring the improved mechanism of heat-to-electricity should be proposed, additionally, the structure should also be carefully engineered and optimized to achieve high efficiency, and power density and facilitate industrial scalability.

1.2 Research Objectives

Current heat-to-electricity technologies suffer from shortcomings including a low power density, a short life span, weak ability for continuous power generation, high material and/or operational costs, lack of capacities for energy storage, system complexity and low heat-to-electricity conversion efficiencies.

For example, traditional thermoelectric semiconductor materials are unable to sustain continuous operation due to their inability to maintain a stable temperature difference over a long time. Conventional TRECs typically provide low power densities below 1 W m^{-2} and long-time spans, while TRABs offer high power densities but short lifetimes due to electrode corrosion. Under this circumstance, a reliable system possesses both higher power density and long-lasting runtime is urgently needed.

Therefore, this study focuses on the key issues of liquid-based electrochemical systems for low-grade heat harvesting, with the aim of achieving the following objectives:

1) continuous power generation (with a discharge time of more than 2 hours);

2) promotion power density to over 5 W m^{-2};

3) realization of good scalability;

4) extension of working time;

5) acceptable cost to enable board-scale implementation.

To achieve these goals, an optimized TREC is firstly studied due to its long-life span, low cost, good scalability and ability to generate continuous power generation. Then, new systems of TRCPC and pH-TRC are developed and studied in detail in this thesis, as listed below. The research overview is given in **Figure 1.1**.

First, to increase the power density for traditional TRECs, we propose applying different electrode reactions to adjust the reaction entropy change in a hybrid-membrane TREC system. This can enhance thermopower, thereby increasing the power density and efficiency. A comprehensive thermodynamic framework is also proposed to provide a clear guiding principle for selection of suitable reactions and analyzing thermopower.

Second, to further enhance the power density, and solve the problem of intermittent operation of TREC, a continuously operating system of TRCPC is presented. We propose applying a symmetrical electrode structure in a TRCPC system and introducing a continuous feed of CO_2 to obtain greater power density and continuous operation time.

Third, to enhance the cycle life and power density of TRCPC, we propose an advanced pH-TRC with circulating hydrogen by replacing the early consumable electrode with an H_2/H^+ catalytic electrode and rationally improving the cell design. In this way, the corrosion of the electrode is anticipated to be alleviated during the discharging-regenerating process.

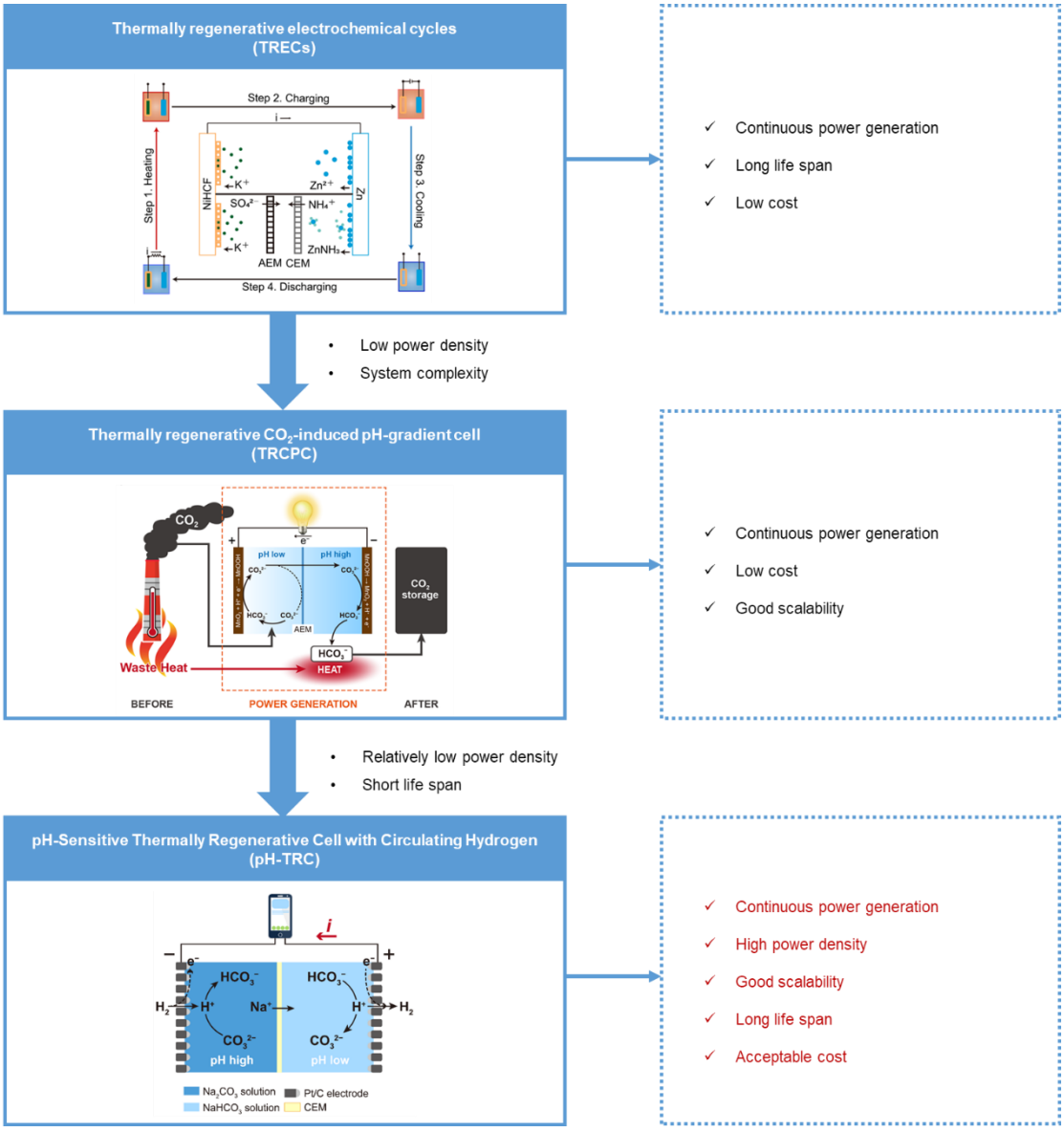

Figure 1.1. Research overview of these three works.

1.3 Outline of This Thesis

This thesis presents the development of high-performance and long-stable liquid-based electrochemical systems for low-grade waste heat harvesting from the aspects of system design, thermodynamics analysis, and electrode engineering. The paper is structured as follows:

Chapter 1: Introduction. This chapter briefly describes the background of low-grade waste heat to electricity, including the actual conditions of heat em issions, current heat-to-electricity technologies, and the research gap of this research. The importance, objectives, and outline are displayed in this chapter.

Chapter 2: Literature review. In this chapter, an overview of various liquid-based systems for converting low-grade heat into electric energy is introduced. Their performances, fundamental mechanism, and optimization strategies are discussed in detail.

Chapter 3: Methodology. In this chapter, the methods for system construction, material characterization, and data collection are summarized.

Chapter 4: Investigations in a TREC of high thermopower. This chapter presents the fundamental study of a TREC with nickel hexacyanoferrate (NiHCF) cathode and Zn anode. Through the theoretical calculation, a modified Nernst equation is derived to determine the theoretical voltage and temperature-dependent reaction energy. The fundamental thermodynamics and kinetics process of potassium ion (K^+) intercalation to NiHCF electrode is also established to build a theoretical framework. Under this theoretical framework, the

efficiency analysis is conducted to compare with other liquid-based systems. Moreover, an optimization strategy is further introduced to boost the thermopower.

Chapter 5: Thermally regenerative CO_2-induced pH-gradient cell (TRCPC) for waste-to-energy conversion. In this chapter, a novel design is developed to address the key issue of TREC by simultaneously utilizing CO_2 and low-grade heat. The theoretical and experimental feasibility are studied. The proof-of-concept implementation is demonstrated to facilitate practical application in industry.

Chapter 6: PH-Sensitive thermally regenerative cell (pH-TRC) with circulating hydrogen. In this chapter, pH-TRC is designed with H_2/H^+ catalytic electrodes to improve the sluggish kinetics of TRCPC thereby enhancing the power density. The theoretical OCV generation and working mechanism are discussed, and the parameter study including the shape, temperature, and flow rate effects are conducted both experimentally and computationally.

Chapter 7: Conclusions and outlook. In this chapter, the conclusions of the aforementioned studies are summarized. We highlight the achievements and contributions of each study and discuss their implications for the development of liquid-based electrochemical systems for low-grade waste heat harvesting. Additionally, suggestions are provided for future research directions in this field.

CHAPTER 2 Literature Review

In this chapter, we provide a comprehensive literature review on various liquid-based systems for converting low-grade heat into electric energy in potentially practical applications. Not only TRECs, but also other technologies, such as TOEC, TRABs, and DTCC are included. The working principles of each system are introduced and summarized. We also compare the different systems in terms of efficiency, power density, stability, and scalability. In addition, the challenges and limitations of each technology are discussed. Finally, the future research directions in this field are discussed.

2.1 TECs (thermos-electrochemical cells)

Thermo-electrochemical cells (TECs), consist of an anode, cathode, electrolyte, and a separator. TECs are non-isothermal electrochemical cell systems. A voltage is established by holding two electrodes at different temperatures within the electrolyte. Electrical current can be produced by connecting the two electrodes. Compared with the semiconductor-based thermal-electrical conversion technology, the principle of TECs is based on a temperature-dependent redox couple. The oxidation and reduction reactions happen on the two electrodes and the oxidized and reduced species transport through the electrolyte. The reactions produce a continuous and stable voltage if there is no degradation of components of TECs. The 3D and 2D schematic representations of TEC are shown in **Figure 2.1**.

The whole energy conversion process is a combination of heat transfer, thermodynamics, electrode kinetics, and mass transfer.[15] Some parameters derived from solid-state thermoelectric systems have been introduced to the TECs to evaluate their efficiency and performance.

The parameter of thermopower (also called temperature coefficient in TECs or Seebeck coefficient in TE) is the ratio of potential difference to the temperature change, describing the ability to produce voltage per unit temperature difference. Thermopower is an intrinsic property of a material. For TE, it is positive if the current flows from the hot side to the cold side inside the semiconductor, which means the thermopower is positive when the current flow direction in the external circuit is opposite to the temperature decreasing direction, the electric field $-dV/dx$ and the temperature gradient dT/dx have the same direction. Therefore, the thermopower of n-type semiconductor is negative while p-type is positive. The thermopower α^* of TE is defined as the ratio of electric field $-dV/dx$ and the temperature gradient dT/dx.[16] And it is given below:

$$\alpha^* = -\frac{dV/dx}{dT/dx} = -\frac{V(T_H)-V(T_L)}{T_H-T_L} \quad (1)$$

where V is the voltage, T_H and T_L are the temperatures of hot side and cold side respectively. For a redox reaction:

$$\mathrm{A} + \mathrm{ne}^- \rightarrow \mathrm{B} \quad (2)$$

The common thermopower α^* calculation equation in most of papers is given below:

$$\alpha^* = \frac{V(T_H)-V(T_L)}{T_H-T_L} = \frac{\Delta S}{nF} \quad (3)$$

where n is the number of transferred electrons of this reaction, F is Faraday's constant, ΔS is the entropy change of this reaction. Regardless of Eastman entropies and transported entropies, ΔS is equal to S_B - S_A. As the thermopower is related to the entropies, it can indicate the spontaneity of reactions. Taking Fe^{2+}/Fe^{3+} redox couple as an example, the entropy is positive up to 1.76 mV K^{-1}.[17]

However, the current carriers are ions but not electrons inside TECs. In order to follow the definition of thermopower in TE, as the thermopower is positive when the current flow direction in the external circuit is opposite to the temperature decreasing direction, a more appropriate definition is given based on the electric field and temperature gradient. Taking this into consideration, the equation needs to be corrected. The corrected thermopower is as below.

$$\alpha = -\frac{V(T_H)-V(T_L)}{T_H-T_L} = -\frac{\Delta S}{nF} \quad (4)$$

Therefore, the thermopower for Fe^{2+}/Fe^{3+} redox couple should be -1.76 mV K^{-1}. The Fe^{3+} obtains an electron at the hot side of TECs (cathode) while Fe^{2+} losses an electron at the cold side (anode). The current direction is exactly the same to the temperature decreasing direction. When introducing the TE definition into TECs, the p-type electrolyte is in the same direction between electric field and the temperature gradient. So, the n-type electrolyte is with positive corrected thermopower, the p-type is with negative corrected thermopower. Briefly, if the hot side is the cathode, cold side is the anode then it is a p-type electrolyte in negative corrected thermopower. The inconsistencies in experimental methods and calculations attribute to the confusion in thermopower data. This paper will provide the original thermopower to show the

respect of the authors. The thermopower data of typical redox couples will be given and the p-type or n-type electrolyte will be noted according to the actual situation mentioned in each paper in **Table 2.1**.

Table 2.1. Thermopower α of typically different redox couples.

Redox couple	Original thermopower α (mV K^{-1})	p/n type*	Electrolyte	Ref.
$[Fe(CN)_6]^{3-}/[Fe(CN)_6]^{4-}$	-1.42	n	0.4 M in water	[17]
$[Fe(CN)_6]^{3-}/[Fe(CN)_6]^{4-}$	4.2	n	24 M urea and 2.6 M GdmCl	[18]
$[Fe(CN)_6]^{3-}/[Fe(CN)_6]^{4-}$	3.73	n	3 M Guanidinium chloride (GdmCl)	[19]
$[Fe(CN)_6]^{3-}/[Fe(CN)_6]^{4-}$	4.8	p	Gelatin	[16]
$[Fe(CN)_6]^{3-}/[Fe(CN)_6]^{4-}$	12.7-17	p	Gelatin and KCl	[16]
$[Fe(CN)_6]^{3-}/[Fe(CN)_6]^{4-}$	-1.21	n	Polyvinyl alcohol (PVA)	[20]
$[Fe(CN)_6]^{3-}/[Fe(CN)_6]^{4-}$	-1.38	n	5 wt % Cellulose	[21]
$[Fe(CN)_6]^{3-}/[Fe(CN)_6]^{4-}$	1.5-1.6	p	P(AM-co-AMPS)/NaCl	[22]
Fe^{3+}/Fe^{2+}	1.76	p	0.8 M in water	[17]
Fe^{3+}/Fe^{2+}	1.02	n	PVA	[20]
I^-/I_3^-	0.86	n	2.5 mM KI_3 and 10 mM KI	[23]
I^-/I_3^-	0.97	n	0.01 M in in ethylammonium nitrate (EAN) ionic liquid	[24]
I^-/I_3^-	1.97	n	cyclodextrins (α-CD, 4 mM), KCl (200 mM)	[23]
I^-/I_3^-	0.71	n	5 mM KI and 2.5 mM I_2	[25]
I^-/I_3^-	-1.91	p	poly (N-isopropylacrylamide) (pNIPAm)	[25]
I^-/I_3^-	−1.32-1.48	n, p	Methylcellulose (MC)	[26]
I^-/I_3^-	−8.18-9.62	n, p	2 wt % MC and KCl	[26]

I^-/I_3^-	1.67	n	30 mM [DiBoylFc][I_3] in [Emim] [NTf_2]	[27]
$[Co(py\text{-}pz)_3]^{2+/3+}$	2.36	p	0.1M in 3:1 DMSO:[C_2mim][eFAP]	[28]
$[Co(bpy)_3]^{2+/3+}$	1.21	n	0.05 M $[Co(bpy)_3]Cl_2$/$[Co(bpy)_3]Cl_3$ in water	[29]
$Cu^{2+}/Cu(s)$	0.73	p	1 M $CuSO_4$ in water	[30]
$Zn^{2+}/Zn(s)$	0.64	p	1 M $ZnSO_4$ in water	[30]
NiO/NiOOH	1.05/2.83	p	1 M $NiSO_4$ in water	[30]*

*According to the unified concept in this perspective, the p-type electrolyte is with negative corrected thermopower, the n-type electrolyte is with positive corrected thermopower.

*1.05 is for range ΔT = 5–30 °C and 2.83 for the range of ΔT = 30–60 °C

In addition to the thermopower, the figure of merit Z is another important parameter for evaluating the energy performance of thermoelectric systems,[31]

$$Z = \alpha^2 \frac{\sigma}{\kappa} \quad (5)$$

where σ is ionic conductivity and κ is thermal conductivity of the material. While the modified figure of merit has been introduced in some materials for TECs applications,[32]

$$Z = \alpha^2 \frac{D_{lim} c z^2 F^2}{\kappa R} \quad (6)$$

where z is the charge of the ion, c is the concentration of the redox couple, R is the gas constant, D_{lim} is the limiting diffusion coefficient. The largest power generation efficiency is determined by a figure of merit under a certain temperature difference. Though the desirable Z is more than 2 for efficient devices,[33] the practical Z value is still very low. High Z values can be obtained from high ionic conductivity and thermopower as well as low thermal conductivity. The ordinary thermoelectric semiconductor materials are usually with high conductivity, and high thermal conductivity but low thermopower, since the carrier contributes to heat transfer and conduction, increasing Z becomes an intrinsic problem. However, for liquid-based systems,

ionic conductivity, thermal conductivity, and thermopower are influenced by more factors. Therefore, more methods are available to improve Z.

The last parameter is thermal-electrical efficiency (related to Carnot efficiency) which is named as power conversion efficiency. The efficiency is expressed as:

$$\eta = \eta_c * \eta_r = \eta_r \frac{T_H - T_L}{T_H} \quad (7)$$

$$\eta = \frac{1/4 V_{oc} I_{sc}}{Ak(\Delta T/d)} \quad (8)$$

where η is thermal-electrical efficiency, η_c is Carnot efficiency, η_r is relative power conversion efficiency which indicates the final heat conversion occupies a proportion of heat from Carnot cycle, T_H and T_L are the temperatures of hot side and cold side respectively, V_{oc} is the open circuit voltage, I_{sc} is the short circuit current, A is the cross-sectional area, d is the electrode separation distance.[34] As the maximum mean power density is reached near half of the open circuit potential,[15] the term $1/4 V_{oc} I_{sc}$ represents the maximum power output. While the term $Ak(\Delta T/d)$ is the input thermal energy to maintain the temperature difference. However, due to the low current, the output of TECs is small. When thermal-electrical efficiency is combined with the above equations, the thermal-electrical efficiency is given as:

$$\eta = \frac{\frac{1}{4\Delta S j_{sc} R_T}}{nF} \quad (9)$$

$$j_{sc} = \frac{I_{sc}}{A} \quad (10)$$

$$R_T = \frac{d}{k} \quad (11)$$

where j_{sc} is the short circuit current density, R_T is the thermal resistance of TECs. Since the heat-to-electricity efficiency is usually less than 1%, lower than the expected efficiency

(2%-5%) for practical energy harvesting applications.[35] Further efficiency improvement of TEC requires the development of electrolytes with low thermal conductivity, redox couple with high reaction entropy, and electrodes with high ionic conductivity and fast kinetics.[15]

Firstly, in order to increase the Carnot efficiency, a larger difference in operating temperature is required. Hence the electrolyte system and separator need to be explored for operating with higher temperature differences. Some non-aqueous electrolytes have a higher maximum working temperature. With the low boiling point of an aqueous system, various ionic liquid-based electrolytes have been explored due to their high boiling point, high ionic conductivity, and low thermal conductivity, which theoretically indicate a higher Z at a higher temperature. What's more, a large temperature gradient can be produced by lowering the thermal conductivity, which means that higher power is available. For instance, the improved electrolyte led to a 66% increase in ionic conductivity and a nearly 6% decrease in the thermal conductivity, and thus produced the highest thermocell power density (12 W m^{-2}) of TECs with a temperature difference of 90 ^{o}C.[36]

However, the thermopower of the redox couple highly depends on the nature of the ionic liquid. It is shown that the thermopower of 0.4 M I^-/I_3^- in ionic liquid (from 0.03-0.26 mV K^{-1}) is lower than that in aqueous (0.53 mV K^{-1}) or organic solvents (0.34 mV K^{-1}). Particularly the value increases with decreasing concentration of redox couple because more solvent ions are available to solvate the redox ions in ionic liquid with a lower concentration, thereby the environment of solvation environment is accentuated.[37] The relationship between thermopower and concentration of redox couple matches Sosnowska's modeling prediction very well.

Moreover, as introduced by the authors, quantitative structure-property relationship (QSPR) and read-across techniques could be utilized to explore higher thermopower ionic liquids with particular structure features. For example, the ionic liquids with smaller size, symmetric and less branching of ionic ions cation, and high vertical electro-binding energy of the anion are predicted to have higher thermopower.[38]

Especially, the biggest challenge for utilizing ionic liquid is the high viscosity of some types of ionic liquid. Thus, organic mixed electrolyte systems have been investigated in terms of improving mass transport properties which can be indicated by the diffusion coefficient. The results have been shown as expected, the diffusion coefficients of mixed electrolyte systems (1:1 ionic liquid: PC (Propylene carbonate)) are much higher than those of pure ionic liquids. For example, it is around 7.7×10^{-11} m^2 s^{-1} of $[Co(bpy)_3]^{2+/3+}$ in mixed electrolyte systems ($[C_4mim]$ $[NTf_2]$ and PC) but 1.2×10^{-11} m^2 s^{-1} in neat ionic liquid ($[C_4mim]$ $[NTf_2]$), leading to a higher power density of mixed electrolyte systems. The power density is 7.78 mW m^{-2} of mixed electrolyte systems and 2.04 mW m^{-2} of neat ionic liquid.[39]

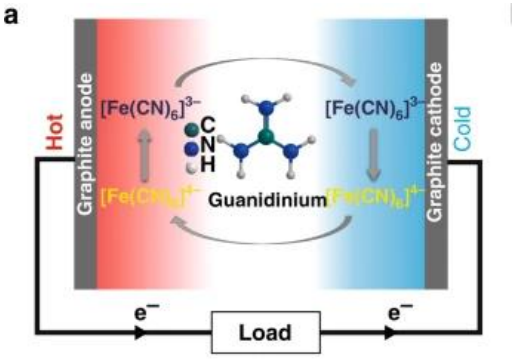

Figure 2.1. Power generation of the cell using 24 M urea and 2.6 M GdmCl with cyanide electrolyte. Reprinted with permission from ref. 18. Copyright 2018 Nature.

Secondly, improving the intrinsic character is a practical way to increase the potential and current generated from the cell, which requires redox coupled with high thermopower. A series of aqueous and non-aqueous redox couples have been extensively investigated. Most of the redox couples are metal ion-based couples. It is reported that ($Fe(ClO_4)_2/Fe(ClO_4)_3$ has the highest thermopower(1.76 mV K^{-1}) among the reported Fe^{2+}/Fe^{3+} salt system with different counter ions due to altered solvation shells of Fe^{2+}/Fe^{3+} because of the non-covalent interactions.[17] Particularly, the thermopower of aqueous ferri/ferrocyanide ($[Fe(CN)_6]^{3-}/[Fe(CN)_6]^{4-}$) is less concentration-dependent than other redox couples. The high thermopower of aqueous ferri/ferrocyanide ($[Fe(CN)_6]^{3-}/[Fe(CN)_6]^{4-}$) is attributed to the large reaction entropy.[40] The impressive 4.2 mV K^{-1} thermopower is achieved by enlarging the entropy change by guanidine chloride (GdmCl) and urea (**Figure 2.1**). The higher charge of $[Fe(CN)_6]^{4-}$ causes a "packed" solvation shell, resulting in a stronger reaction with Gdm^-. While urea tends to bond with $[Fe(CN)_6]^{3-}$, leading to the synergistic effect of the significant entropy change.[18] And by utilizing the similar crystallization effect with the reactant ions, the reaction balance is changed to a preferable direction,[19] which brings a high power density of 6.86 W m^{-2} and thermopower of 3.73 mV K^{-1} with a temperature difference of 51 ºC. Besides GdmCl, a series of redox inactive ions have been added to the $[Fe(CN)_6]^{3-/4-}$, $[Fe(H_2O)_6]^{3+/2+}$ electrolyte to explore the non-covalent interactions, reaction entropy change, water structure in reaction

kinetics. The entropy change in $[Fe(H_2O)_6]^{3+/2+}$ significantly depends on the anion structure breaker such as ClO^{4-} and Cl^- while the entropy change in $[Fe(CN)_6]^{3-/4-}$ relies on the cation structure making such as Li^+. The phenomenon is due to the non-covalent interactions induced by the inert ions as supporting electrolytes, leading to the altered solvation shells. By adding the structure making or breaking ions, the negatively charged electrostatic center will attract or repel the new ions through electrostatic interaction. This leads to the rearrangement of the water-CN structure. The interaction within the solvation shell of redox specie can be observed by FTIR (Fourier-transform infrared spectroscopy), where different structure-making/breaking abilities will result in lesser peak displacement. The higher thermopower can be obtained by adding suitable inactive ions to produce the larger entropy. However, the reaction kinetics should be carefully considered because the ions may tightly couple with the water molecules after adding structure making cation, which requires higher energy to restructure and consequently lowers the reaction kinetics.[41] In addition to a series of inactive ions as shown in **Table 2.1**, chemically crosslinked networks such as gelatin,[16] PVA,[20] and AM-co-AMPS[22] can also be introduced into liquid-based TECs to adjust thermopower. In these cases, though thermopower is adjustable, power densities are usually below 1 W m^{-2} due to their slow mass transfer through networks, therefore impeding large-scale industrial applications.

Cobalt-based redox couple has been demonstrated to perform well in both aqueous and non-aqueous systems, which provides an optional substitute for iron-based redox couple. The thermopower of cobalt-based redox couple in the ionic liquid is relatively high. The highest thermopower is 2.36 mV K^{-1} using $Co^{2+/3+}(py\text{-}pz)_3$ complex owing to the small radius, the bi-

dentate ligands, lower degree of charge delocalization and the change in electronic spin state, compared to the other complexes investigated.[28] The reported highest output can reach up to 880 mW m^{-2}.[42] While the thermopower of $Co^{2+/3+}(bpy)_3$ redox couple is influenced by the solubility, supporting electrolyte, electrode surface area, and diffusion rate.[42] However, though the thermopower of $[Co(bpy)_3]^{2+/3+}$ in water (1.21 mV K^{-1}) is lower than that in organic solvents, the diffusion rate is higher than that in organic solvents, which offers faster mass transport and higher current.[29]

With the very early redox couples (such as ferric/ferrous and ferri/ferrocyanide redox couple) widely applied, iodide/triiodide redox couple (0.97 mV K^{-1}) [24] and other metal-based redox couples are under development. However, the reported redox couple combined with the solid metal and aqueous ion requires the consumption of metal, which is not available for continuous power generation. Burmistrov's group used the traditional scheme of a thermogalvanic cell to investigate metal electrodes. The high thermopower of the nickel electrode may be attributed to the nickel and hydroxides on the electrode surface. The possible decay process of transformation of hydroxides of three and divalent nickel results in the 2.83 mV K^{-1} thermopower.[30] The thermopower of different redox couples is listed in **Table 2.1** which is compared with the thermopower of thermoelectric materials in **Figure 2.2**.[9]

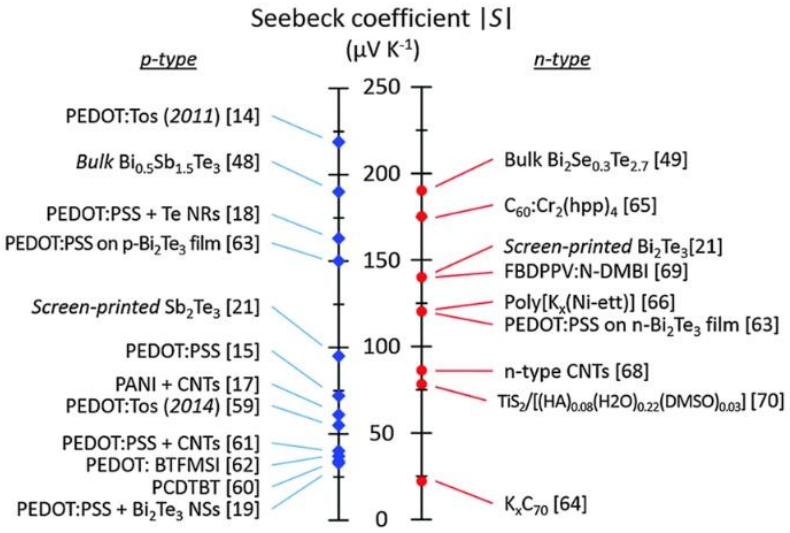

Figure 2.2. The thermopower of thermoelectric materials for both p-type and n-type. Reprinted with permission from ref. 9. Copyright 2015 Royal Society of Chemistry.

Thirdly, more and more researches aim to increase the I_{sc} and lower the R_T, which in turn can boost the power output. The current density depends on the voltage according to the Bulter-Volmer equation, the diffusion rate, effective surface area of the electrode, the electro-kinetic rate constant, cell thickness, and the convection.[15] According to Nernst-Plank equation, I_{sc} consists of migration current density j_m and diffusion current density j_d. j_{sc} tends to increase with the enhanced diffusion effect because j_m and j_d are positively related to concentration gradient and diffusion rate. This was proved by Salazar's group. The kinetic and mass transfer resistance analysis of 0.4 M potassium ferri/ferocyanide demonstrates that the current density is mainly limited by the low diffusion rate at the cold electrode. The greater consumption of redox couple at cold electrode results in current density reaching the limiting value.[15] However, a high diffusion rate does not always provide a higher current density. Kim and co-workers[43]

explored the diffusion and current generation in the porous electrode by both quantitative description and experimental method. $Fe(ClO_4)_2/Fe(ClO_4)_3$ is utilized in their TEC. They tried to increase the current by increasing the volume of the porous electrode. However, the current density increases from 11.3 A m^{-2} with one-layer carbon fiber lamination to 16.4 A m^{-2} with four-layer carbon fiber lamination. The average current density per layer even decreases from 11.3 A m^{-2} with one-layer carbon fiber lamination to 4.1 A m^{-2} with four-layer carbon fiber lamination. The decreased effectiveness can be explained that the ion concentration decreases with ion diffusing through the electrode. The generated current becomes smaller due to the consumption of ions along the way into the electrode layer. It means that the ion diffusion hampers the high current density inside the porous electrode.[43]

The j_{sc} can also be improved by increasing the effective area. The carbon-based electrode shows a promising potential to increase the j_{sc} and efficiency because of its large surface area. Carbon-based electrodes are possible alternatives to Pt electrodes for their low cost. The highest energy relative power conversion efficiency η_r reported is up to 3.95% , and the maximum power density is 6.6 W m^{-2} when applying a high surface area carbon-nanotube aerogel electrode with a temperature difference of 51 ºC.[44] As excellent nanometer thermoelectric materials, carbon-based materials including MWNT,[34] carbon single-walled nanotube (SWNT)/reduced graphene oxide (rGO)[45] show potential to be applied to TECs with high energy efficiency. The reason is explained by Hu et al. [34] that the large j_{sc} generated by MWNT is caused by the large number of redox reaction sites established by the large surface

of the electrode. Consequently, the electron transfer at the electrode-electrolyte surface is enhanced by the fast kinetics.

Finally, the structural design of the thermoelectric devices also significantly influences energy efficiency. Teflon cell, Mark II TEC, coin-type TEC, and Teflon flow cell are introduced and examined with MWNT electrode. The mass transfer is strengthened by decreasing the distance between electrodes. The relative power conversion efficiency η_r is up to 1.4%, which is higher than other structures.[34]

The structure of adjustable series-connected TEC arrays shows promising potential in wearable devices. Due to the low voltage of a single TEC, adjustable series-connected TEC arrays may expand the working voltage window. A basic simple TEC device is established based on p-type electrolyte and n-type electrolytes corresponding to the n-type and p-type elements of a conventional thermoelectric generator. p-type electrolyte ($[Fe(CN)_6]^{3-}$/$[Fe(CN)_6]^{4-}$, -1.42 mV K^{-1}) and n-type electrolyte ($Fe(ClO_4)_2/Fe(ClO_4)_3$, *1.76 mV* K^{-1}) use redox couple of opposite thermopower, leading to the same current direction in possible series path[17]. However, the $Fe(ClO_4)_2/Fe(ClO_4)_3$ electrolyte is actually a p-type electrolyte and the ($[Fe(CN)_6]^{3-}$/$[Fe(CN)_6]^{4-}$ electrolyte is actually a n-type electrolyte according to our definition. The TEC arrays with solidified electrolytes can be explored in such long cycle time applications as wearable electronic systems because of the outstanding mechanical properties without leakage problems. The solid-state of semisolid state electrolytes enables the integration of TECs in a large scale. Yang et al.[20] assembled an integrated gel-based flexible thermocell. The gel electrolyte contains Poly(vinyl alcohol) (PVA) and redox couples ($FeCl_2/FeCl_3$ and

$K_4Fe(CN)_6/K_3Fe(CN)_6$). The thermopower of PFC gels ($FeCl_2/FeCl_3$) is 1.02 mV K^{-1} while that of PPF gels ($K_4Fe(CN)_6/K_3Fe(CN)_6$) side is -1.21 mV K^{-1}. But the mean thermopower is 0.6 mV K^{-1} which is lower than those of PFC and PPF because of the significant thermal contact resistance. The generated voltage varies linearly with the temperature. The device containing 59 PFC and PPF can deliver a voltage of 0.85 V and a power output of 0.3 μW with a temperature difference of 12 ºC.[20] Although it provides high voltage, maximum power output is still low, which is possibly owing to the poor mass transportation of solidified electrolytes.

However, with researches focusing on efficiency, the researches on optimization of the power output of TEC are limited. The reported highest power is 12 W m^{-2} by improving electrolyte (0.9 M $K_3Fe(CN)_6/(NH_4)_4Fe(CN)_6$), electrolyte-filled thermal separators (sponge thermal separator), carbon electrode materials (activated carbon cloth).[36]

2.2 Thermally Regenerative Electrochemical Cycles (TRECs)

In order to create the temperature gradient to utilize the Seebeck effect, the TEC is designed to separate the hot and cold electrodes, which produces a distance between two electrodes. Therefore, the relatively high ohmic resistance caused by the significant distance between the two electrodes leads to low energy efficiency. This ohmic loss can be reduced by narrowing the distance while setting the temperature-dependent redox couples at different times. Thermally regenerative electrochemical cycles (TRECs), convert a full electrochemical

process in spatial dimension at a certain time into four steps including charging and discharging processes in sequential.

TREC is designed to possess two electrodes with opposite thermopower. According to recent reports, the thermopower of cathode and anode are mostly negative and positive respectively. As above mentioned, the thermopower of the cell is determined by the total entropy change in the full cell reaction. If α_{cell} is negative, the cycle is correspondingly cooling - discharging - heating - charging while if the α_{cell} is positive, the process turns to heating - discharging - cooling - charging.

A dimensionless parameter *y* has been introduced to adjust to TRECs electrode material. Compared with Z, the electric conductivity is changed to a specific charge capacity while the thermal conductivity is replaced by specific heat. *y* is used to describe the character related to efficiency which is also similar to Z merit of figure ($y = \alpha q_c/c_p$), where q_c is the specific charge capacity, c_p is the specific heat of an electrode. *y* is calculated to evaluate the efficiency. Apparently, *y* is increased with the higher thermopower and specific charge capacity and lower specific heat of an electrolyte.[46]

The calculation of conversion efficiency can be defined as the net work (*W*) divided by the input heat (*Q*). For the net work, the maximum output is $\Delta T \Delta S$ minus the energy loss both at high and low temperatures (mainly because of the resistance). The input heat can be divided into two steps. In the first heating step, the energy of raising temperatures of system Q_{HR} is relevant to the heat recuperation efficiency. It is expressed as $Q_{HR} = (1-\eta_{HR})C_p\Delta T$, where η_{HR} is the efficiency of recuperation efficiency and C_p is the total heat capacity of the whole cell.

In the second heating charging process, the total input energy at high temperature is Q_H (Q_H = $T_H \Delta S$). So the efficiency of heat to electricity is given below: [47,48]

$$\eta = \frac{\Delta T\Delta S - W_{loss}}{T_H\Delta S + (1-\eta_{HR})C_p\Delta T} \quad (12)$$

while:

$$\Delta T\Delta S = \alpha_{cell} Q_c \Delta T \quad (13)$$

$$W_{loss} = I(R_H + R_L) \quad (14)$$

$$\mathrm{Y} = \frac{\alpha_{cell} Q_c}{C_p} \quad (15)$$

$$\eta_c = \frac{T_H - T_L}{T_H} \quad (16)$$

where Q_c is the charge capacity of the cell, C_p is the total heat capacity of the cell, α_{cell} is the thermopower of the whole cell, R_H and R_L are internal resistance at high and low temperatures respectively, I is the current used in charging and discharging processes. The efficiency related to Carnot efficiency is shown below:

$$\eta = \eta_c \frac{1 - I(R_H + R_L)/|\alpha_{cell}|\Delta T}{1 + \eta_c(1-\eta_{HR})/|Y|} \quad (17)$$

$$\eta_r = \frac{1 - I(R_H + R_L)/|\alpha_{cell}|\Delta T}{1 + \eta_c(1-\eta_{HR})/|Y|} \quad (18)$$

Besides the efficiency, the maximum power output (P_{max}) is obtained when the load resistance is equal to the resistance of the cell.

$$I = \frac{\alpha_{cell}\Delta T}{2(R_H + R_L)} \quad (19)$$

$$P_{max} = \frac{(\alpha_{cell}\Delta T)^2}{8(R_H + R_L)} \quad (20)$$

However, the efficiency formula does not take consideration of the effect of energy loss W_{loss} on the heat exchange. The modified equation is given by Chen.[49]

$$\eta = \frac{\Delta T\Delta S - W_{loss}}{T_H\Delta S + (1-\eta_{HR})C_p\Delta T - W_{loss}/2} \quad (21)$$

Figure 2.3 shows the development and performance of different thermoelectric technologies including their power densities and relative efficiency relative to Carnot. The power density of TREC is approximately ranging from 1 to 10 W m^{-2},[50] however, actually this value should be lower than 1 W m^{-2} based on our calculations. The point is the unit conversion of non-metal solid electrode TREC from W g^{-1} to W m^{-2}. The typical power density cases are given as approximately 0.178 W m^{-2},[47] 0.015 W m^{-2},[48] 0.015 W m^{-2},[51] and 0.332 W m^{-2}.[52] The power density is hindered by the resistance of the cell including the resistance of the solution and the cell structure, more importantly, caused by low mass transfer of ions. In comparison with the theoretical voltage value, the potential of the whole cell is relatively low with the small output current. This overpotential arises from the mass transfer problem. This still requires further research to enhance the power density.

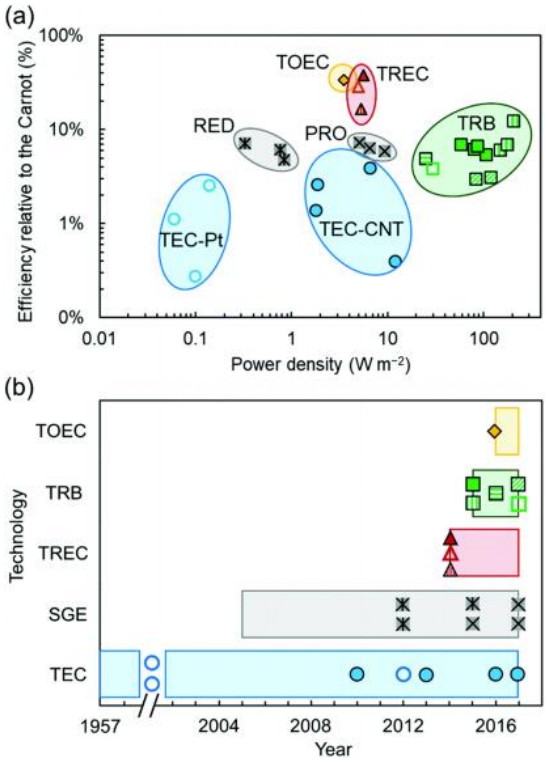

Figure 2.3. Comparison of low-grade thermal energy conversion approaches, **a)** The power

density and efficiency relative to the Carnot **b)** The research time of different approaches, TEC with platinum (TEC-Pt)[53] or with carbon nanotube electrodes (TEC-CNT); [36,37,44,54] SGE (salinity gradient energy) systems including RED (reverse electro-dialysis)[55–58] and PRO (pressure retarded osmosis);[59,60] TREC; [51] TRB[61, 62] and TOEC.[63,64] Reprinted with permission from ref. 48. Copyright 2018 Royal Society of Chemistry.

TREC was first reported in the 19th century. Nowadays research of TRECs have turned from harvesting high-temperature heat (such as from fuel cell) [65,66,67] to harvesting low-grade waste heat. The entropy change during a charging-discharging cycle is also applied in the desalination field to explore solar, geothermal, and wind energy.[68,69,70] Combining the deintercalation process of sodium ion and potassium ion battery, with applying Prussian blue analog (PBA), TRECs show advantages of good stability and long cycle life of this reversible process.

2.2.1 Non-metal Solid Electrode

Typical cases are TRECs based on PBA.[47] A copper hexacrynoferrate (CuHCF) cathode and Cu/Cu^{2+} anode with ion-selective membrane and aqueous copper nitrate (anolyte) and sodium nitrate (catholyte) electrolyte form the main parts of this cell. The thermopower α_{cell} of the whole system is up to -1.20 mV K^{-1}, while -0.36 mV K^{-1} of the cathode and 0.83 mV K^{-1} of the anode respectively. When discharging at a low temperature of 10 ºC (charging temperature at 60 ºC), sodium ions insert into the cathode material and copper dissolves into the anolyte. The maximum thermal conversion efficiency is up to 5.7% with the thermal-electrical efficiency relative to Carnot efficiency η_r of 38%.

One issue in this TREC is the anion exchange membrane, which is designed to prevent the side reaction between Cu and CuHCF. It might lose perm-selectivity at high temperatures after cycles. A membrane-free PBA-based TREC has been developed by switching the redox couple. Using NiHCF cathode (-0.62 mV K^{-1}), Ag/AgCl anode (0.12 mV K^{-1}), and KCl electrolyte, this TREC reaches maximum thermal efficiency of 3.5% with the thermal-electrical efficiency relative to Carnot efficiency η_r of 29% between 15 ºC and 55 ºC. Reactions are shown below.[48]

$$KNiFe(CN)_6 + K^+ + e^- \rightarrow K_2NiFe(CN)_6 \quad (22)$$

$$Ag + Cl^- \rightarrow AgCl + e^- \quad (23)$$

A similar cobalt hexacyanoferrate (CoHCF)-based system was also investigated, using the same Ag/AgCl anode. The thermopower (0.89 mV K^{-1}) and energy conversion efficiency (1.91%) of CoHCF with helical carbon nanotubes (HCNTs) appeared to be higher than those of the pure CoHCF (0.69 mV K^{-1}, 0.77%). This indicates that complexed PBA with carbon material may promote the efficiency.[71]

Most of the research as mentioned above focus on materials with negative thermopower. Spinel lithium manganese oxide (LMO) is introduced as a possible material with 0.48 mV K^{-1} thermopower in organic electrolyte with its fast kinetics during the intercalation/deintercalation process. An aqueous electrochemical system is assembled with LMO (0.62 mV K^{-1}) cathode and CuHCF anode.[72] The whole cell thermopower is 1.061 mV K^{-1}, which determines that the generated voltage of high temperature is higher than that of low temperature. It results in the cooling-discharging-heating-charging cycle, which is more of a thermally regenerative electrochemical refrigerator. The efficiency reaches 1.8% with a 10-40 ºC temperature scale. The LMO cathode and CuHCF anode are based on the lithium ion and potassium ion intercalation/deintercalation reaction respectively.[72]

The TREC performance may be limited for harvesting at higher temperatures due to the degradation and side reactions. High temperature causes capacity decay problems. The

authors also investigated the effects of the electrolyte component and states of charge (SOC) on thermopower. The entropy change varies from the SOC, which means temperature response closely corresponds to SOC. Another heat harvesting system based on organic $LiCoO_2$/Li cells is constructed as stacks. The efficiency of a dual-temperature dual-stack system based on homemade $LiCoO_2$/Li coin cells is 0.22%. Though the efficiency is not high, the system is attractive for self-powered sensor networks.[73]

The above-mentioned TRECs need an additional charging process as the deintercalation cannot happen spontaneously after metal ions insertion. Therefore, the additional potential is needed to initiate the status. A charging-free system has been reported by using an increasing temperature pour cell and initiating the state. This charging-free electrochemical system consists of inexpensive ferri/ferrocyanide redox couple and solid Prussian blue particles as active materials at both electrodes. The voltages of the two electrodes change respectively due to their different thermopower. The two voltages start at different initial potentials and cross over at a point, which indicates the self-conversion of cathode and anode induced by temperature. When this TREC works at 20 ºC and 60 ºC, the heat to electricity conversion efficiency is 2.0%.[51]

Actually, the complete cell requires the two electrodes to have a positive thermopower and negative thermopower respectively. Usually, the thermopower can be enlarged by more negative thermopower of cathode and more positive thermopower of anode, which ensures the negative α_{cell} (the cycle is correspondingly cooling - discharging - heating - charging) to harvest heat.

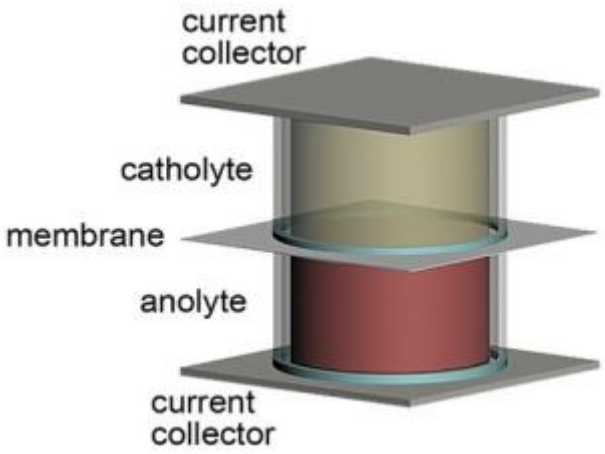

Figure 2.4. Schematic of the battery design, 0.5 M $K_3Fe(CN)_6$/0.1 M $K_4Fe(CN)_6$ (catholyte) versus 0.1 M I_2/2 M KI (anolyte). Reprinted with permission from ref. 52. Copyright 2019 Royal Society of Chemistry.

Apart from the traditional method for heat utilization, a novel system (**Figure 2.4**) for simultaneous energy conversion and storage via solar-driven regenerative electrochemical cycles is designed by Ding et al..[52] The anode functions as both a bifunctional current collector and a solar absorber under solar irradiation. $K_4Fe(CN)_6$/$K_3Fe(CN)_6$ and KI/KI_3 are selected by evaluating the limiting diffusion current and reaction rate constant, which show fast kinetics to overcome the sluggish mass transport and reaction activation. The catholyte ($K_4Fe(CN)_6$/$K_3Fe(CN)_6$, negative thermopower) and anolyte (KI/KI_3, positive thermopower) are separated by a cation-exchange membrane, leading to the whole thermopower of -1.8 mV K^{-1}. Moreover, the carbon felt wrapped by reduced graphene oxide (rGO) acts as a solar absorber and a current collector, which greatly boosts the temperature. A good efficiency of 1.23% is achieved with a small temperature difference of 35 ºC.[52]

As the equilibrium potential, reaction kinetics, and mass transport properties are temperature-dependent, the activation, ohmic loss, concentration loss, and overpotential are

affected by temperature. In fact, all three overpotentials decrease with increasing temperature. The activation overpotential loss decreases with increasing temperature due to reduced energy barrier decreases at a higher temperature. The concentration overpotential loss also decreases with increasing temperature as the viscosity of the liquid decreases with increasing temperature, leading to favorable mass transport. In addition, the ohmic loss decreases with increasing temperature due to the higher ionic conductivity of the electrolyte at a higher temperature. Thus, the performance of the TRECs can be significantly improved by increasing the temperature. However, in order to reduce ohmic and concentration loss, large current density operations should be avoided. At a high current density, concentration loss can be a limiting factor especially when the system is working at a limiting current density. In addition, the ohmic loss increases almost linearly with increasing current density. Obviously, the effective power output is limited by the current density.

Based on the experimental work, the performance characteristics of TRECs are also analyzed by modeling.[49,67,74,75] Finite-time analysis is utilized to study the impacts of various operating and material parameters on the performance of TRECs, giving the criterion for optimizing the performance.[67] The authors suggest the material with larger isothermal coefficients, specific charge/discharge capacities, appropriate internal resistance, and lower heat is appealing. Since the regenerative efficiency does not influence the maximum power output, it means that the regenerative loss $(1-\eta_{HR})C_p\Delta T$ referred as Q_{HR} above does not affect the power output. This is also proved by Wong et al. [74] that regenerative loss does not influence the corresponding $P_{max} = m\alpha^2\Delta T/8R$ is the number of cell charged simultaneously, where R is the resistance in both series connection and parallel connection. However, regenerative efficiency does have a significant impact on efficiency. The efficiency equation depicted by Wong reveals that the efficiency increases with decreasing regenerative losses. As

the power output decreases with the efficiency increase when $\eta \geq \eta_p$, the objective function ηP is given to determine the operation region of the current. The optimal range of the electric current should be $I_{\eta P} \leq I \leq I_P$, so $P_{\eta P} \leq P \leq P_{max}$, $\eta_P \leq \eta \leq \eta_{\eta P}$, where the subscripts ηP are the maximum efficiency-power product, *P* is maximum power, *max* is maximum.[74]

2.2.2 Redox Flow Batteries (RFBs)

At present, redox flow batteries (RFBs) have been applied in energy store systems. Due to the ability to storage large-scale energy, and long cycle lifetime,[76] researchers investigate the all-vanadium redox flow battery (VRFB) to explore the feasibility of capturing low-grade heat. The principle is based on the reversible reaction of V (II) / V (III) in the negative electrolyte and V (IV)/V (V) in the positive electrolyte. As shown in **Figure 2.5**, V (II) is oxidized to V (III) at the negative reservoir while V (V) is reduced to V (IV) during discharge (reverse reaction of equation 24-25). Protons move from negative to the cathode through the proton Nafion membrane to maintain electrical neutrality. The electrolyte continuously flows between the reservoirs and the electrode, bringing ions to the electrode surface where an electrochemical reaction takes place.[77] Owing to the different temperature responses of negative electrolytes and positive electrolytes, general TRECs can be introduced into RFBs. The created thermodynamic cycle of the TREC-VRFB system is displayed in **Figure 2.6**.

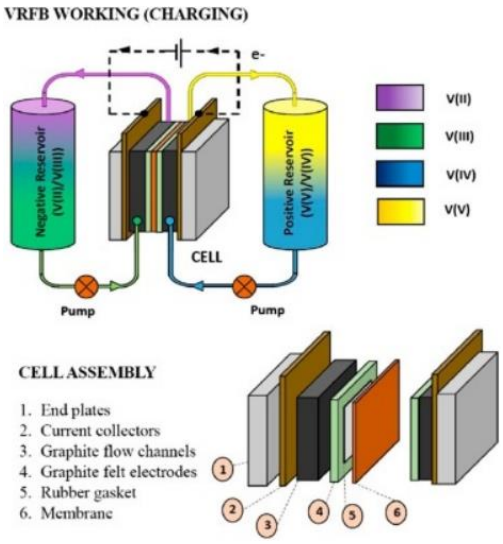

Figure 2.5. The structure of VRFB. Reprinted with permission from ref. 72. Copyright 2019 Elsevier.

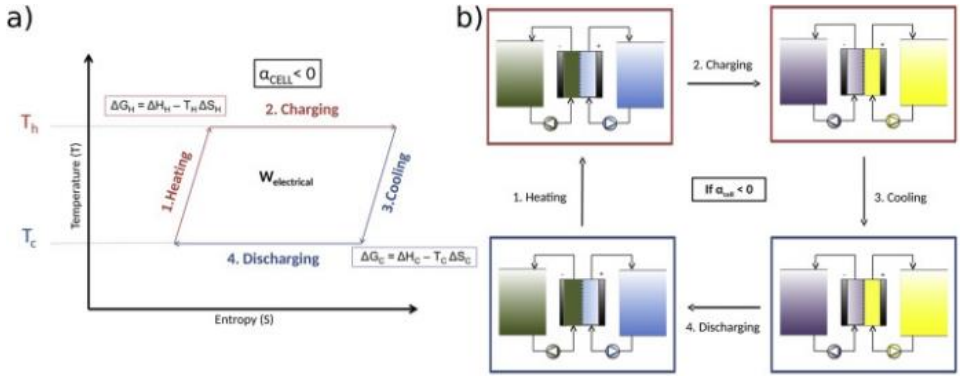

Figure 2.6. The principle for harvesting heat of VRFB, **a)** The temperature-entropy plot for a TREC when thermopower is negative **b)** The thermodynamic cycle of TREC-VRFB system. Reprinted with permission from ref. 73. Copyright 2018 Elsevier.

$$V^{3+} + e^- \rightleftharpoons V^{2+} \quad (24)$$

$$VO^{2+} + H_2O \rightleftharpoons VO_2^+ + e^- + 2H^+ \quad (25)$$

Reynard's group reported the thermopower of the whole cell (TREC-VRFB) in the commercial electrolyte is around -1.16 mV K^{-1} while it is -0.80 mV K^{-1} in the mixed-acid electrolyte which is dominated by the negative electrolyte. The energy density is increased by 1.3 Wh L^{-1} and 0.8 Wh K^{-1} respectively.[78] This is appealing for heat harvesting and electricity generation in the photovoltaic farm.[79] However, the available temperature range is limited by the unstable voltage (V).[80] The operating temperature is strictly limited between 10-40 ºC to avoid precipitation.[81] Also, the complete VRFB system is integrated by electrolyte container, electrode, pipe, pump, and heat exchanger, leading to the large weight and volume and further low energy density.

As most of the articles do not give the exact efficiency value of TRBs, however, due to the auxiliary power input, the efficiency calculation is affected by more factors, the equation is given as below:

$$\eta = \frac{I\left(\Delta V - I(R_H + R_L)\right) - I^2 R_{Lead} - P_{aux}}{I T_H \Delta\alpha + Q_{loss} + (1-\varepsilon_{HX})\dot{m} C_p \Delta T} \quad (26)$$

where R_{Lead} is the resistance of the electrical leads, $\Delta\alpha$ is the difference of thermopowers, P_{aux} is auxiliary power input (it is mainly pumping power in this system), $(1-\varepsilon_{HX})\dot{m}C_p\Delta T$ is the heat leaks from the mass transport of reactants, ε_{HX} is the effectiveness of the recuperative heat exchanger and $\dot{m}$ is the mass flow rates of the fluids respectively.[8]

Similarly, a continuous electrochemical heat engine[8] also exploits the flowing electrolyte with aqueous $V^{2+/3+}$ (1.7 mV K^{-1}) and $Fe(CN)_6^{3-/4-}$ (-1.4 mV K^{-1}) to create an overall 3 mV K^{-1} of the cell. With a Zn anode and catholyte of $Fe(CN)_6^{3-/4-}$ guanidinium, this system presents an overall thermopower of -3.28 mV, a maximum power density of 1.24 W m^{-2} and an actual thermoelectric power density of 0.245 W m^{-2}.[82] For $V^{2+/3+}$/$Fe(CN)_6^{3-/4-}$ system, at

the maximum power density of 110 μW cm^{-2} equivalent to 1.1 W m^{-2}, the corresponding η_r and η_c are 0.15 and 12.4%, respectively. The authors believe that by using a variety of redox couples, the maximum power increases with the electrode reaction rate constant k_0 till k_0 is 0.05 cm s^{-1}. The power output is only a function of thermopower α at a high k_0, suggesting the change in polarization and rate controlling steps. Under this circumstance, the ohmic resistance and mass transport loss are larger than activation polarization. In other words, the ohmic and mass transport loss limit the achievable maximum power density. Changing the fluid flow patterns (improving mass transport) and increasing redox couple concentrations (improving reaction rate) both contribute to higher power density. A higher power density of 200 W m^{-2} with 15 M concentrated slurries is theoretically predicted. This high power density could be achievable for redox couples with high solubility. However, the solubility of most redox couples is insufficient.

It should be noted that in the current literature, both Wh L^{-1} and W m^{-2} are used to measure the performance of the thermoelectric cell. Wh L^{-1} is energy density. It is obtained by running a system for a certain time under a certain power condition, then dividing the electrolyte volume. It evaluates the efficiency of the system. For comparison, W m^{-2} is power density, which is based on the membrane area. Comparing power densities of different systems not only gives the power generation ability but also, is helpful to analyze the utilization and performance of the membrane.

2.2.3 Thermal Regenerative Ammonia-based Batteries (TRABs)

Since thermally regenerative acetonitrile-based all-copper redox flow battery reported before,[83] new thermal regenerative ammonia-based batteries (TRABs) is reported to utilize low-grade heat for electricity generation. Cu^{2+}/Cu cathode and Cu-NH_3/$Cu(NH_3)_4^{2+}$ are applied

to this system. The electricity is generated by the formation of metal ammine complexes. While the solid copper electrodes alternative serves as anodes or cathodes in TRABs, NH_3 is separated and transferred by traditional heat-based separation technology. The theoretical voltage is up to 0.344 V. The cycle is shown in **Figure 2.7**.[61]

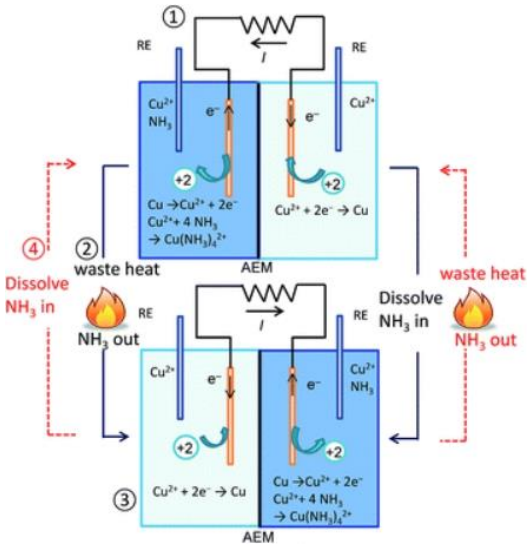

Figure 2.7. The closed-cycle system for TRAB. Reprinted with permission from ref. 61. Copyright 2015 Royal Society of Chemistry.

As referred above, the solvation limitation which restricts the power density is solved by introducing high solvation NH_3. The power output of TRABs is much larger than the highest power output of TECs (12 W m^{-2}) and RFBs (1.1 W m^{-2}), which shows great advantages for practical application. The reported power output of Cu-TRAB is 60 W m^{-2},[50] however, the value varies from 47 to 136 W m^{-2}. With the low resistance BTMA PPO anion exchange membrane, the power output is increased to 106 W m^{-2} while the efficiency is increased to 0.97%.[62] Furthermore, ethylenediamine shows a better performance than ammonia as a ligand. The power output of an ethylenediamine-based battery (TRENB) is 85 W m^{-2} with 2 M ethylenediamine and 119 W m^{-2} with 3 M ethylenediamine. However, the energy requirement of the separation process of ethylenediamine is 2.5 times more than that of ammonia, which

causes lower thermal-electric efficiency (0.52%). Higher thermal-electric efficiency can be obtained by examining alternative separation methods.[84] The comparison of parameters in various systems is listed in **Table 2.2**.

Table 2.2. The comparison of parameters in various system.

System	Power output ($W\ m^{-2}$)	η (%)	η_r(%)	Temperature (condenser-reboiler/ ^oC)	Ref.
Cu-TRAB	60	0.86	6.2	-	[61]
BTMA-TRAB	106	0.97	7.0	43.3-70.4	[62]
TRENB	119	0.52	3.1	-	[84]
Ag-TRAB	23	0.41	3.8	43-60	[85]
Cu-TRAFB	45	0.70	5.0	43.3-71	[86]
Cu/Zn-TRAB	118	0.95	10.7	43-70.9	[87]
Cu/Zn-TRAFB	280	0.34	2.7	43-70.9	[11]

With the development of TRABs, the researchers focus on improving the performance. The main aspects are given below.

1) The poor long cycle lifetime stability. The poor reversibility is derived from the unbalanced electron exchange of the anode and cathode, which means the metal is consumed in continuous cycles (less than 10 cycles). The anode coulombic efficiency (ACE) is approximately 37% while the cathode coulombic efficiency (CEE) is around 100%, resulting in a relatively low discharge energy efficiency (44%). This indicates a large portion of copper dissolved in the anode electrolyte but does not take part in the

electrode reaction. This is based on the side reaction of dissolved oxygen and the formation of $Cu(OH)_2$, and further proved by adding acid and removing dissolved oxygen to improve the battery performance.[61] Replacing the ammonia ligand with ethylenediamine raises the ACE to 77%.[84] Moreover, a high ACE of almost 100% is obtained by using silver salt.[85] The promising value represents excellent reversibility, proved by over a hundred charge/discharge cycles of producing a stable power. Due to the high cost of silver, the metal electrode is substituted with carbon-silver electrodes.

2) The resistance problem. The whole resistance consists of the Ohmic resistance and the activation resistance. Both Ohmic resistance and activation resistance can be determined by the electrochemical impedance spectroscopy (EIS) test. Ohmic resistance is battery internal resistance caused by the electrolyte conductivity and diffusion rate. Additionally, the reaction resistance is related to the electrode dynamics. For example, the charge-transfer resistance can judge the difficulty of the reaction kinetics: the smaller charge-transfer resistance means better reversibility of the electrode. The better reversibility of Ag compared with Cu is because of the low reaction resistance (0.08 Ω).[85] In order to solve the resistance problem, a compact design is required to stack the electrodes and membrane together. Adding NH_4NO_3 as a supporting electrolyte also enhances the electrolyte conductivity and reduces the resistance without bringing other ions and pollution. But dense NH_4NO_3 might increase the viscosity, which increases the transport resistance of copper ions, leading to high reaction resistance and energy loss. The peak power density is obtained at 3 M NH_4NO_3 concentration in the range of 1-5 M, suggesting the existence of an optimal concentration.[88]

3) The concentration optimization of Cu^{2+} and NH_3. The cycle stability is ensured by the consistency of the cathodic Cu^{2+} concentration and the anodic $Cu(NH_3)_4^{2+}$

concentration in every cycle. Owning to the copper corrosion during discharging, the cathodic Cu^{2+} concentration is greater than the anodic $Cu(NH_3)_4^{2+}$ concentration. Therefore decreasing the initial anodic $Cu(NH_3)_4^{2+}$ concentration is necessary to avoid cyclical concentration change. Also, appropriately increasing Cu^{2+} and NH_3 concentration could improve the battery performance because Cu^{2+} concentration determines the limiting current density which shows mass transport ability, while NH_3 concentration has a vital effect on the power output and overpotential.[88] The power output increases from 53 W m^{-2} with 1 M NH_3 to 136 W m^{-2} with 3 M NH_3.[61]

4) The temperature effects. Compared with 95 W m^{-2} at 23 ºC, the maximum power density linearly increases to 236 W m^{-2} at 72 ºC. The high relative efficiency η_r (13%) is obtained with a total efficiency η of 0.5%. An improved reaction kinetics at higher temperatures attested by the reduced overpotential result in the enhancement in power production. However, the high temperature causes the loss of membrane selectivity and further brings about the ammonia crossover problem, which leads to a decrease in power density and coulombic efficiency.[89]
5) Effect of flow rate. The use of flowing electrolytes is a practical method to strengthen mass transport. The power density of Cu/Zn-TRAFB (280 W m^{-2}) is twice more than the power density of Cu/Zn-TRAB (118 W m^{-2}).[11,87] The power output increases with the flow rate when the flow rate is below 8 mL min^{-1}, otherwise, the reaction is controlled by the kinetic rate under sufficient mass transfer.[11]
6) Scalability of system. The flexibility of compiling battery systems in series or parallel can meet the actual demands for voltage and current.[11,61]

2.2.4 Electrical Double-layer-based Cycle

The thermally induced entropy change is utilized to harvest energy by constructing electrical double-layer capacitors. One method is to make use of the thermal membrane potential of the ion exchange membrane to extract energy from a small thermal difference,[90] or harvesting the mixing free energy of solutions of different concentrations. In particular, the electrostatic potential increases with the temperature, which enhances the ion-capturing ability.[91] As shown in **Figure 2.8**, the voltage changes from 2.50 to 2.536 V at 65 ºC temperature, the calculated thermopower of the capacitor is 0.6 mV K^{-1} and the theoretically predicted efficiency is 5%.[91] However, both two methods are confronted with the decay problem. Thus, the power generation is not continuous, the operation process is within a certain time scale.

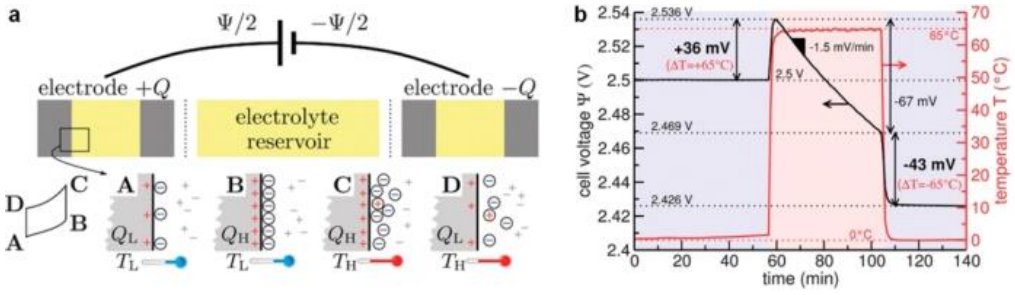

Figure 2.8. a) A supercapacitor model with two parallel plates. **b)** The open-circuit potential change when cycling the fully charged cell between 0 and 65 °C. Reprinted with permission from ref. 91. Copyright 2015 Royal Society of Chemistry.

2.2.5 Direct Thermal Charging Cell (DTCC)

Direct thermal charging cell[92] for converting low-grade heat to electricity was invented recently. In particular, this kind of isothermal heating operation does not require external charging and building thermal gradient. DTCC can be self-regenerated after discharging. While the thermopower is quite high up to 5 mV K^{-1}, the thermoelectric conversion efficiency reaches 3.52% at 90 ºC with 19.7% of Carnot efficiency. Compared with the other thermal cycles and thermal conversion devices, the thermopower and efficiency are still high. However, the degradation problem of cathode limits the application which requires long-term cycling.

DTCC consists of asymmetric electrodes (a capacitor-type cathode of GO/PtNPs and a battery-type anode of PANI) and an aqueous electrolyte containing Fe^{2+}/Fe^{3+}. DTCC generates the voltage by the temperature-induced pseudocapacitive GO and temperature-dependent electron carriers (redox couple). The relevant electrical double layer-based cycle has been reported to thermal induced ionic entropy change which results in a thermopower of 0.6 mV K^{-1} of the double layer capacitance. The voltage change is 0.036 V of the temperature change from 0 to 65 ºC. This illustrates the existence of the temperature-dependent capacitive effect.

At first, DTCC is heated at an open circuit. Due to the pseudocapacitive effect, oxygen functional groups absorb protons and react at the electrode-electrolyte interface. Due to the positive thermopower of the Fe^{2+}/Fe^{3+} redox couple, the reduction reaction happens with the increase in temperature. The open circuit voltage is enhanced by the two effects. Then connect the two electrodes, PANI self-oxides while electrons transfer to cathode to attribute to the reduction of Fe^{3+}. At the last regeneration stage, oxidized PANI reacts with Fe^{2+} and revert to the initial stage. The reaction is given below:

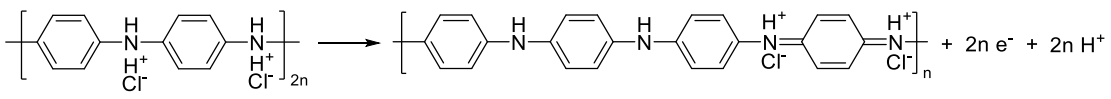

(27)

DTCC exhibits excellent efficiency and power density. What's more, potential applications including a wide operation window and low-cost cell stacks are under exploration. But it still remains an ongoing challenge of cyclability which requires further research like changing the cathode materials or redox couple to tackle the degradation problem. Furthermore, the mechanisms of reactions of temperature-induced pseudocapacitive effect together with the PANI polymer catalytic activation have yet to be identified.

2.3 Thermo-osmotic Energy Conversion (TOEC)

Thermo-osmotic energy conversion (TOEC) is a new technology based on the hydrophobic membrane. When the temperature gradient tends to drive the vapor flux against a hydraulic pressure difference, a pressurized flow is produced to drive a turbine or other types of machines.

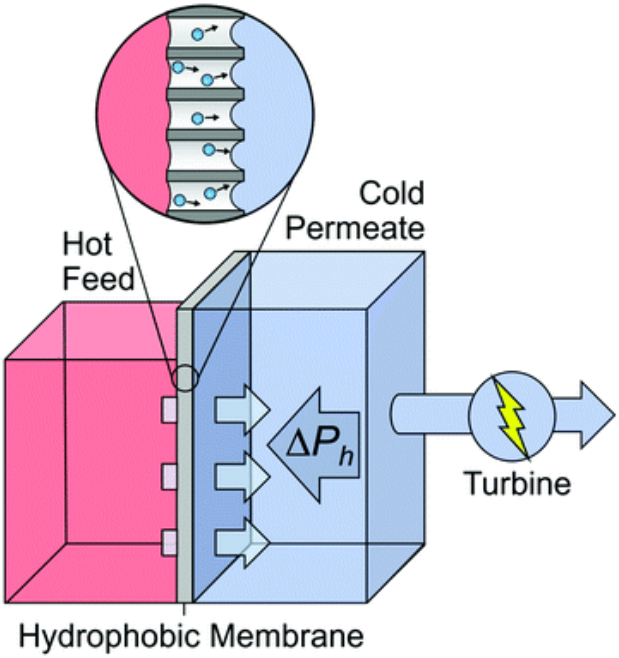

Figure 2.9. Working principle of TOEC system, a, Schematic diagram of water vapour transport across a membrane, b, Hydraulic pressure that can be theoretically generated with a certain temperature difference across a membrane. Reprinted with permission from ref. 63. Copyright 2018 Royal Society of Chemistry.

As demonstrated in **Figure 2.9**, applying a hydrophobic, nanoporous membrane between hot and cold liquid creates a gas phase, temperature-driven flux against the pressure-driven flux from the hot side to the cold side. Consequently, the volume of the cold liquid hinders the expansion and leads to pressure on the turbine for power generation. Water is used in this system due to its high surface tension, which prevents the membrane pore from infiltration. Vapor-gap membrane is used in this system because of their relatively high thermo-osmotic fluxes and relatively low thermal conductivity of polymer membrane. Polytetrafluoroethylene (PTFE) has been first used in this system, producing a 3.53 ± 0.29 W m^{-2} power density with a 40ºC temperature difference (20ºC-60ºC). The efficiency of an optimized system with a continuous closed-loop system is more than 50% of Carnot efficiency.[63]

The thermal efficiency of the membrane is the amount of heat transferred by vaporization through the membrane divided by the total heat transferred. The heat loss mainly is due to the thermal conductivity of the membrane. Thermal efficiency is relevant to the thermal conductivity and thickness of the membrane. In order to increase efficiency, reducing thermal conductivity is a practical way.[64] The working fluid investigated by now is water because of high surface tension and high heat of vaporization, however, mixing of fluids, such as working fluid with different absorption of CO_2 also shows the potential of improving the performance.[93] More importantly, higher efficiency can be obtained by increasing the pressure and a higher power can be obtained by increasing the area of the membrane theoretically. But the

amelioration strategies for increasing pressure resistance and high-performance structure are still under investigation.[64]

2.4 Summary and Perspectives

Compared with TE, liquid-based systems show great advantages in power density, efficiency, and cost. With more and more researchers' interests and efforts in the use of liquid-based systems for recovering low-grade waste heat, power density and efficiency have been improved significantly. However, in order to make the systems practical, the fundamental understanding and the cell design are both vital to overcome the key performance limitations.

For TECs, the key point is the redox couple and cell configuration. As most researchers focus on efficiency improvement, the practical application of TECs is limited by the low power density (maximum 12 W m^{-2}), which can be improved by changing alternative redox couple with higher thermopower and optimizing the cell configuration.

First and foremost, a redox couple with higher thermopower requires development in exploring the new redox couple or maximizing the entropy change by improving electrolytes. The detailed analyses have been discussed above. In particular, the computational modeling is under-utilized to investigate a new redox couple and additive. The simulation is supposed to theoretically explain the relationship between the thermopower and entropy change and solvent structure. Furthermore, the simulation based on the design of systems and current experimental data provides a reasonable suggestion on structure optimization, moreover predicts the performance of the whole system. The computational and simulation methods show huge potential in terms of analytical ability. Secondly, cell configuration approaches can improve power density in certain perspectives. For example, a significant power density change is the

application of electrolyte-filled thermal separators (sponge thermal separators).[36] The increased thermal resistance attributes to a larger temperature gradient inside the cell. While the proper thickness and porosity lead to decreased thermocell resistance. According to the currently achievable power density, future work on utilizing TECs possibly focus on the integrated TEC arrays for wearable devices because of the low power density requirement.

The TRECs are confronted with the same power density difficulty (below 1 W m^{-2}) which can be improved by increasing the whole thermopower of the cell, widening the temperature range, and lowering the resistance. These requirements need the fundamental understanding of entropy change of material during the reaction, the advanced electrode material design with fast kinetics and higher temperature tolerance, good design of a system or cell configuration and also, a membrane with good selectivity and low resistance.

Firstly, the fundamental understanding of the thermopower should be further studied. Since the general understanding of thermopower of redox couple is based on the solvation structure in the liquid phase, the thermopower of the solid phase is more complex. The influence factors include phonon entropy, configuration entropy, and electron entropy. These are widely studied in the heat control system of industrial battery packs. However, we still need to trace the origin of entropy change in the solid phase. As referred by Gao et al.,[46] the problems are the relation of entropy change and properties of electrode material, the optimization in electrode material, and composition. Secondly, the exploration of electrode material is needed. As other problems such as cell configuration can be settled by technical methods, the electrode material is an urgent problem for TRECs. The material is required to make entropy contribution to the thermopower of the whole cell during the reaction, has fast kinetics, and long-term stability to ensure the reaction conduction. Although utilizing metal ion battery materials give us a good idea, the thermopower of the whole cell is relatively low. The redox couples are possibly introduced into the TRECs. DTCC is a good example to fulfill the cycles with

Fe^{2+}/Fe^{3+} redox couple, but its long-term operation still needs to be further improved. What's more, the guidance on enlarging the thermopower will become clearer if more evaluation and analysis are conducted to determine the entropy contribution of the solid phase and liquid phase. Thirdly, the investigation membrane is also required. As an important component of TRECs, the membrane separates the anode and cathode. More importantly, it prevents the possible side reaction in the system. And in a specific TREC system, good selectivity, and low resistance, more importantly, high-temperature tolerance is critical. Finally, optimization in cell configuration is vital for real applications. As for the performance of TRECs, actually, even though the low power output can be solved by connection in series or parallel, the exact problem is the small effective current density in spite of the high thermopower. In this perspective, TRECs show a certain potential in application in sensors due to the low power requirement, the smallest sensor only needs 10 mW in a 10-30 cm^2 area.

Among the various types of TRECs, TRABs are the most promising practical application because it performs the surprisingly highest reported power density (280 W m^{-2}) so far. The poor cycle performance can be ameliorated by replacing the metal ion. Optimizing the concentration of supporting electrolyte, ligand and metal ions, and adjusting the temperature and flow rate propose a reasonable plan to maximize the power output and efficiency. Future work will probably aim to lower the cost to achieve the perfect coulumbic efficiency, leading to practical large-scale power generator application.

While the major problem of TOEC is lacking robust membranes under pressure. Some works focus on the design of the membrane to create a theoretically 88.8 W m^{-2} excitingly high power density [94], which shows great potential in eco-friendly and continuous heat harvesting. However, the work in this field is limited therefore it still needs further exploration.

To sum up, the TRABs present the highest power density followed by TECs and TOECs, which are competitive with semiconductor thermoelectric material (~mW cm^{-2}), while TOECs,

TRECs, and DTCC display relatively higher efficiency. They overlap in their functionality but have unique features and working conditions. The TRAB systems can be potentially up-scaled for large-scale applications for recovering industrial waste heat. Other systems such as TOECs and TECs can be applied to recover waste heat below 100 ºC, such as waste heat from air conditioners. In addition to these technologies mentioned above, there are other technologies for waste heat recovery such as organic Rankine cycle, heat recovery steam generator, and heat pipe system. What's more, a combination of different technologies such as triboelectric, pyroelectric, piezoelectric, thermoelectric, and thermal-electrochemical systems [95] establishes a new field to boost efficiency and power density. The related materials such as ZnO nanowire arrays, polarized poly(vinylidene flfluoride) (PVDF) film-based generators, both have pyroelectric and piezoelectric properties. The assembled hybrid cell can harvest thermal, mechanical, and solar energy simultaneously.[96-97]

CHAPTER 3 Methodology

3.1 Evaluation of The Efficiency and Power Density

The efficiencies referred to in this thesis can be categorized as a) Carnot efficiency, b) conversion efficiency and c) relative power conversion efficiency. In the traditional system, Carnot efficiency is traditionally regarded as the maximum theoretical efficiency for heat-to-electricity conversion, based on thermodynamic analysis using a Carnot cycle. As a Carnot cycle runs between a heat source at a higher temperature (T_H) and a heat sink at a lower temperature (T_L), the Carnot efficiency (η_c) is calculated as follows:

$$\eta_c = \frac{T_H - T_L}{T_H} \tag{28}$$

However, the realistic efficiency falls short of Carnot efficiency since a complete conversion from heat to electricity hardly succeed. The calculation of conversion efficiency, which is also referred to as thermal-electrical efficiency, can be namely defined as the net work (W) divided by the input heat (Q). The efficiency is expressed as:

$$\eta = \eta_c * \eta_r = \frac{W}{Q} \tag{29}$$

where η is thermal-electrical efficiency, η_r is relative power conversion efficiency which indicate proportion of the heat from the Carnot cycle that is successfully converted into electricity by the system. In other words, η_r reflects the actual performance of the system in

converting heat into electricity, taking into account both the efficiency of the conversion process and the temperature difference between the heat source and the heat sink.

3.2 Material Characterization

The scanning electron microscope (SEM) images were collected in TESCAN VEGA3 to observe the micromorphology of samples. The powder X-ray diffractometer (Rigaku SmartLab 9kW-Advance) with Cu K irradiation source was used for providing X-ray diffraction (XRD) patterns at a rate of 10° min^{-1}. The X-ray photoelectron spectroscopy (XPS) was tested by the Nexsa XPS system. Comprehensive surface and elemental analyses by XPS including oxidation states and valences of surface elements were determined from the peak positions and peak area of XPS results.

3.3 Performance Test of TREC, TRCPC and pH-TRC system

The systems studied in this thesis are electrochemical systems that consist of an anode, a cathode, a membrane, and an electrolyte. To assemble the battery in each system, the electrodes, membrane, and electrolyte were fabricated according to specific designs, which will be discussed in detail in the following chapters.

The heat-to-electricity systems were carried out under ambient air to evaluate the performance. Ideal temperature control was achieved by either water bath or thermoelectric

modules. By circulating the water or regulating the output of thermoelectric modules in advance of achieving the setpoint, the temperature of the system was well controlled at the desired temperature with an over or undershoot limit. For the thermoelectric modules, the temperature was measured through a thermocouple (TT-K-40, Omega), which was clamped between the thermoelectric module and the cell with thermal conductive silicone grease to minimize measurement error. Regarding to water bath, the thermocouple was attached closely to the surface of the cell. After calibration, the thermocouple has an error of ±0.2℃ at temperatures ranging from 0 to 100℃. The effectiveness of this system has been confirmed in previous work of Wang[92] and Yang[48].

The open-circuit potential (OCV), linear sweep voltammetry (LSV), and discharging test were performed on a CHI 760E electrochemical workstation (CH Instrument, Shanghai, ±0.1 mV). The OCV data was collected after a 30-min standing. LSV measurements were conducted via the potentiodynamic procedure at varied scan rates. The discharging performances were evaluated by measuring the peak power density from LSV results and estimating the discharging time under a galvanostatic discharging mode. According to the measured LSV curve, the voltage decreases as the current increases. Therefore, within the range from zero to open-circuit voltage, the working current decreases from high to low, resulting in a maximum power value, which is the peak power density. The data presented in this paper has been averaged prior to its demonstration.

CHAPTER 4 Investigations in TREC of High Thermopower

4.1 Introduction

In response to the existing problems in current heat-to-electricity technologies including low power densities and short lifespans, the prevalent TREC systems were selected to be studied first due to their high efficiency and good stability. Since a complete TREC exploits the temperature-induced voltage from two electrodes, in a cooling - discharging - heating – charging cycle or heating - discharging - cooling – charging cycle, voltage differences generated by different temperatures are critical. Therefore, the parameter α is introduced to evaluate the ability to generate temperature-induced voltage.

The α is calculated by $\alpha = \frac{\Delta E}{\Delta T} = \frac{\Delta S}{nF}$, where n is the number of transferred electrons in the electrochemical reaction, F is Faraday's constant, and ΔS is entropy change of the electrochemical reaction. As the α determines the theoretical voltage at the specific operating temperatures, it is critical to the achievable power output and energy efficiency. Efforts have been made to enlarge the α by increasing the reaction entropy change (ΔS). As the fundamental understanding of the origin of α is critical for further improving the TREC systems, a series of Prussian blue analogs (PBA) such as copper hexacyanoferrate (CuHCF), nickel hexacyanoferrate (NiHCF), cobalt hexacyanoferrate (CoHCF) as referred in the introduction section have been studied to explore the entropy change of their intercalation reaction to enlarge the thermopower. It is found the thermopower of PBA is corresponding to the lattice

status, and the entropy change ΔS could be divided into ion entropy, phonon vibration entropy, configuration entropy, electron entropy, and other entropy. In addition to PBA, metal complex redox systems including TRABs have also been widely explored. They mainly rely on ligand adsorption such as ammonia to create a voltage gap between two reactions. In other words, the thermal-induced phase change produces an energy gap to harvest waste heat. Introducing metal-based electrodes thereby adjusting entropy change might be a promising strategy. Therefore, in this work, we combined PBA-based cathode in traditional TRECs and metal-based anode in reported TRABs to enhance thermal-induced voltage change.

4.2 Experimental Section

4.2.1 Experimental Overview

The objective of this experiment was to investigate the feasibility of a designed thermally regenerative electrochemical cycle (TREC) system. To synthesize the necessary materials, a coprecipitation reaction was employed to produce NiHCF powder, which was then used to prepare the electrodes along with zinc plates. After the TREC cell was assembled, experimental data was collected using an electrochemical workstation. **Table 4.1** provides a summary of the experimental results.

Table 4.1. The experimental information.

Name	Brand	Usage
$NiCl_2$	Showa Kako Corporation	Raw materials for synthesis of NiHCF powder
$K_3Fe(CN)_6$	Sigma-Aldrich	Raw materials for synthesis of NiHCF powder
Carbon black	TIMCAL	Raw materials for preparing electrode slurry
Polyvinylidene fluoride (PVDF)	SOLEF	Raw materials for preparing electrode slurry
1-Methyl-2-pyrrolidone (NMP)	Sigma-Aldrich	Raw materials for preparing electrode slurry
K_2SO_4	Sigma-Aldrich	Raw materials of electrolyte
Membrane	Nippon Kodoshi Corporation, MPF30AC100	Raw materials of cell fabrication
Cation/Anion exchange membrane	Huamo Technology, Hangzhou	Raw materials of cell fabrication
Hot plate	Thermo Fisher	Equipment for preparing electrode
Refrigerated centrifuge	Sigma	Equipment for purifying powder
Electrochemical workstation	CH Instrument, Shanghai	Equipment for evaluating discharging performance

4.2.2 Electrode preparation

The NiHCF powder was prepared by the co-precipitation method. NiHCF was synthesized by mixing $NiCl_2$ and $K_3Fe(CN)_6$ solution. 250 mL of 10 mM $NiCl_2$ and 250 mL of 5 mM $K_3Fe(CN)_6$ were dropped in deionized water (one drop per second) under a strong string at 50°C

to avoid possible side reactions. The suspension was fully settled down overnight. After washing the precipitate with deionized water three times to remove the Cl^- and K^+, the suspension was then centrifuged at 10,000 rpm for three minutes and dried at 60℃ overnight. The obtained powder is lemon yellow. To prepare the NiHCF electrodes, the NiHCF slurry was made by mixing 70 wt% NiHCF nanoparticles, 20 wt% carbon black, and 10% polyvinylidene fluoride (PVDF) in 1-Methyl-2-pyrrolidone (NMP). The liquid percentage is about 0.5 g mixing power with 3 mL NMP. The slurry was cast onto the 1×2 cm stainless metal mesh at 70℃. The metal mesh was placed on a hot plate lined with weighing paper for easy peeling.

4.2.3 Cell Fabrication

The electrodes were separated by the membrane. After soaking with 0.5 M K_2SO_4 electrolyte, the pouch cell was sealed by hot press using a hot press to prevent any leakage. The improved system was fabricated by two types of cells as shown in **Figure 4.1**. The cation exchange membrane was bought from Huamo Technology, Hangzhou.

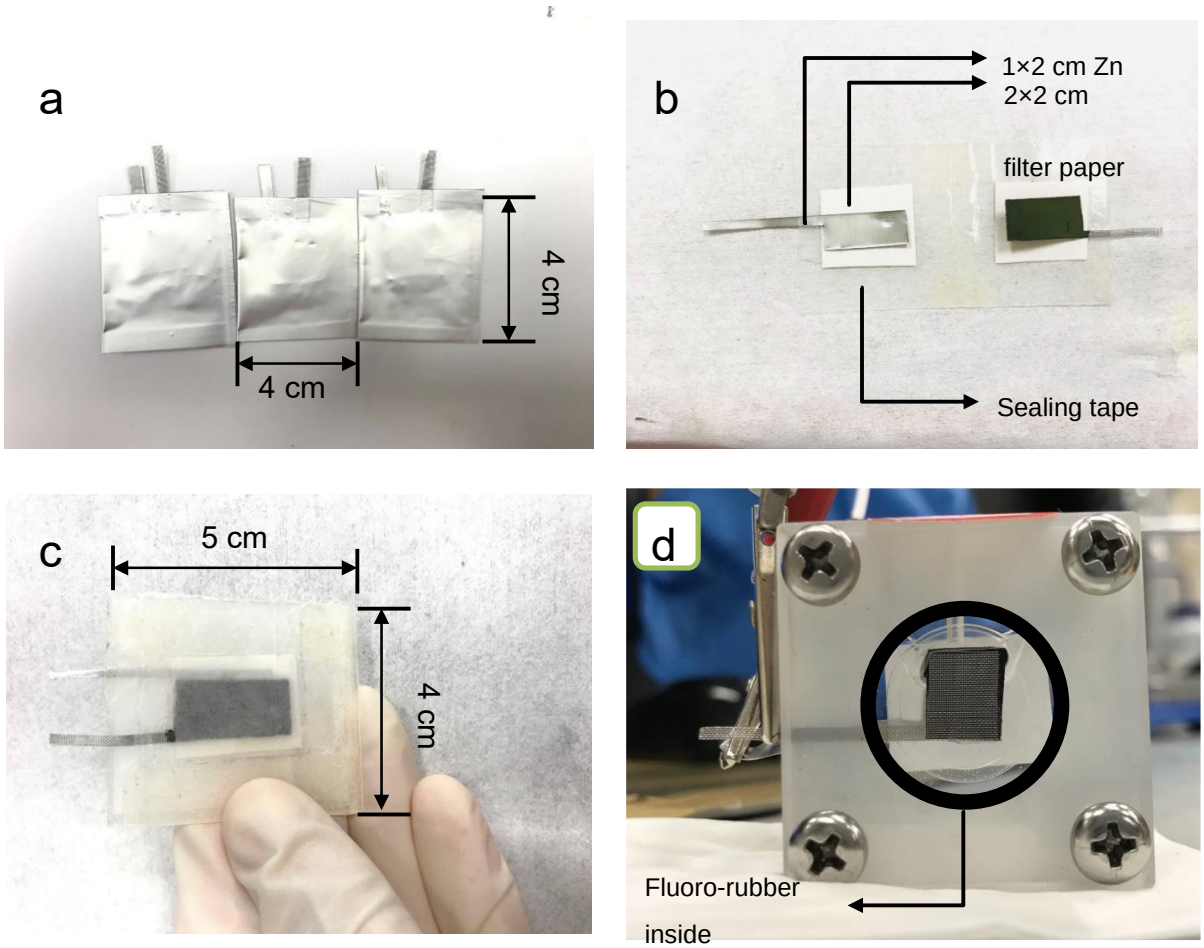

Figure 4.1. The cell fabrication**. a)** The assembled pouch cell to test thermopower with K_2SO_4 electrolyte. **b)** The cell fabrication: the battery shell is made of 4×5 cm polypropylene (PP) membrane and sealant is applied along the edges. Filter paper is set under the electrode in order to absorb the electrolyte. Catholyte and anolyte are injected by needle tube after sealing membrane. **c)** The totally sealed device with CEM and AEM inside. **d)** The cell with sealed method by silicone pad, fluoro-rubber and Vaseline.

4.2.4 Temperature Control

The temperature control system was mainly composed of two thermoelectric plates to

contact the upper and bottom surfaces, a power source to control the heating and cooling current of thermoelectric plates, and thermocouples to measure real-time temperature. The thermopower was determined by measuring the different OCVs at various temperatures (10℃ to 40℃) and then calculating the average slope of the fitting potential of different potential change stages.

4.3 Optimizations in Thermopower

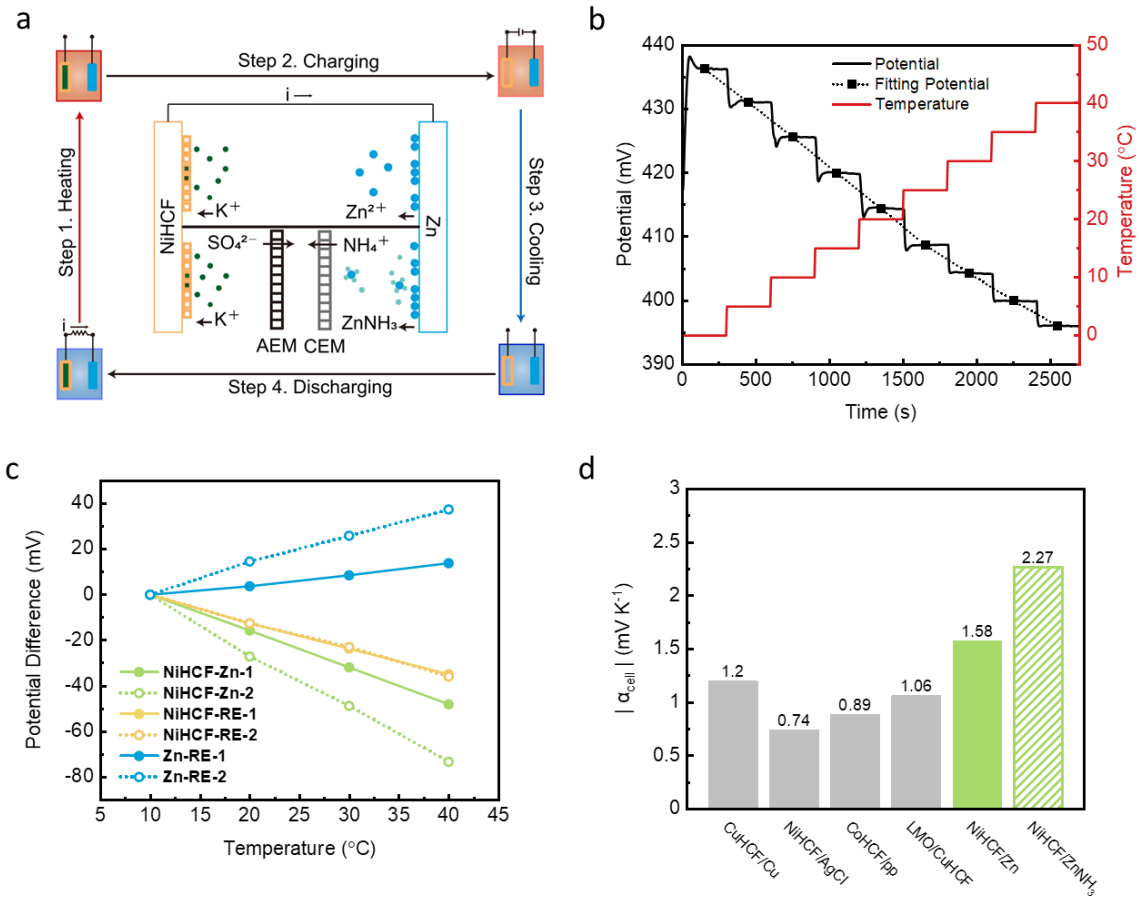

Figure 4.2. Working diagram of TREC and α performance of cathode, anode and the cell. **a)** The four steps working principle of TREC and the discharging reaction of NiHCF/Zn and

$NiHCF/ZnNH_3$ system. **b)** The cathode voltage response to the temperature from 0℃ to 40℃. **c)** The NiHCF, Zn vs. RE (AgCl/Ag) and full cell voltage difference change with temperature difference of 30℃. 1 represents $NiHCF/K_2SO_4/Zn$ system, 2 represents $NiHCF/K_2SO_4//NH_3+(NH_4)_2SO_4+ZnSO_4/Zn$ system. **d)** The comparison on absolute α value of different systems including CuHCF/Cu, [47] NiHCF/AgCl, [48] CoHCF/pp[98] and LMO/CuHCF,[72] green marked bars are our work.

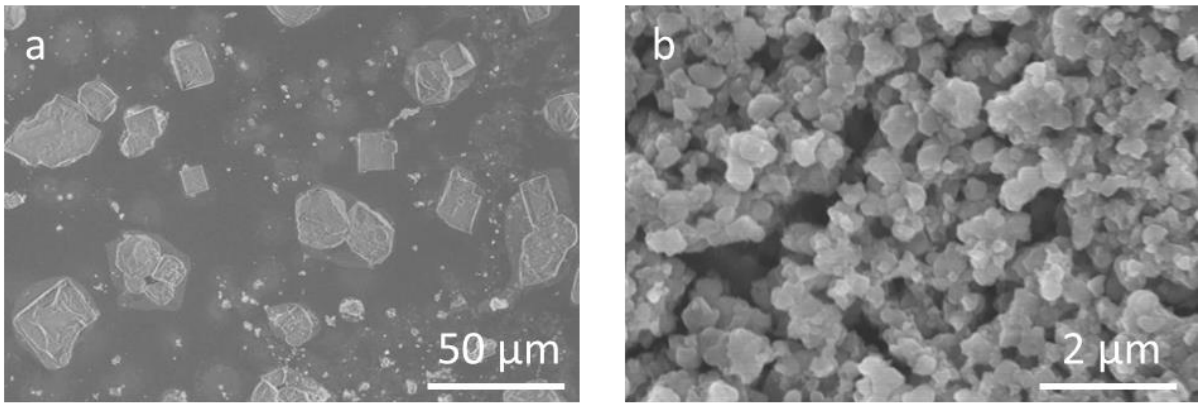

Figure 4.3. Morphology of NiHCF powder. **a)** The SEM image of NiHCF power after settling down overnight. **b)** The SEM image of grinding NiHCF particle with carbon black and binder (PVDF).

As is shown in **Figure 4.2a**, the energy conversion process includes four steps: heating up, charging, cooling down, and finally discharging. When the system is heated to a high temperature (T_H), the OCV decreases ($V(T_H)$) in the first step. Then system is charged in the second step. When the system is cooled down to a low temperature (T_L), the OCV increases ($V(T_L)$) to a voltage higher than $V(T_H)$. Finally, the discharging process is conducted at a low temperature. In such a cycle, the low-grade heat energy is utilized to create a potential

difference so that the system can be charged at a lower voltage ($V(T_H)$) and discharged at a higher voltage ($V(T_L)$), producing net electrical energy. The change in electric potential per unit temperature difference is defined as α (thermopower), which has been explained in the introduction chapter, and is also called the temperature coefficient for the liquid-based systems, or Seebeck coefficient for thermoelectric materials.

Both the efficiency and power output of the system are highly dependent on α. In order to obtain higher efficiency and power output, a larger α is required to provide a larger potential difference. Here, we applied NiHCF as a cathode and Zn as an anode. The two half-reactions are given as formulas 30 and 31:

$$KNi^{II}Fe^{III}(CN)_6 + K^+ + e^- \rightarrow K_2Ni^{II}Fe^{II}(CN)_6 \quad (30)$$

$$Zn \rightarrow Zn^{2+} + 2e^- \quad (31)$$

In this system, potassium ions intercalate into the electrode materials while Zn dissolves into the electrolyte during the discharging process. NiHCF nanoparticles were synthesized by dropping both 10 mM $NiCl_2$ aqueous solution and 5 mM KNiFe $(CN)_6$ aqueous solution into 50℃ deionized water with stirring. The average particle size is about 200 nm (**Figure 4.3a** and **b**). The anode was prepared by ultrasonic cleaning the pure zinc plate. The electrolyte was 0.5 M K_2SO_4 aqueous solution. Because of the active properties of zinc, the neutral pH (~6.5) solution helped to minimize zinc corrosion. Zinc was stabilized by K_2SO_4 electrolyte. The cathode, anode, and separator were assembled in a pouch cell.

As is shown in **Figure 4.2b**, the OCV changes quickly with the temperature while the α is the slope of the fitting potential. From the fitting slope of Figure 1b, the optimized NiHCF achieves an average α of -0.875 mV K^{-1} (-0.720 mV K^{-1} ~ -1.176 mV K^{-1}), while Zn presents an average α of +0.700 mV K^{-1} (+0.608 mV K^{-1} ~ +0.79 mV K^{-1}). Thus, the overall α of the

full cell reaches -1.575 mV K^{-1} (-1.403 mV K^{-1} ~ -1.752 mV K^{-1}).

Previous researches focused on the cathode development to increase the α due to the difficulty in adjusting the entropy change of anode reaction in a single neutral electrolyte. Because of the low α of metal, adjusting the reaction entropy of the zinc electrode instead of improving the material properties could be an effective way to enhance the α. Thus, a coordination reaction can be used because it brings extra reactant to change the reaction entropy change. To enlarge the α, a coordination reaction given below was introduced as shown in formula 32-33.

$$Zn \rightarrow Zn^{2+} + 2e^- \quad (32)$$

$$Zn^{2+} + 4NH_3(aq) \rightarrow [Zn(NH_3)_4]^{2+} \quad (33)$$

As ZnO^{2-} tends to be produced in strongly alkaline solution, and at the same time this reaction requires a concentrated NH_3(aq) environment, the pH value should be carefully controlled. Consequently, the anolyte was designed as a mixture of 2 M NH_3 and 1 M $(NH_4)_2SO_4$ and 0.1 M $ZnSO_4$, where the supporting electrolyte $(NH_4)_2SO_4$ was used to adjust the dissociation equilibrium of NH_3, so as to maintain the appropriate pH value. Due to the cathode degradation caused by NH_3 adsorption reaction and the side reaction with hydroxide,[99] NiHCF would be dissolved gradually. Therefore, the single cation exchange membrane (CEM) or anion exchange membrane (AEM) was not enough to prevent the adsorption of NH_3 and the side reaction. Here, a new design[100] as shown in **Figure 4.2a** was used to decouple the electrolyte. In order not to introduce additional evaporation entropy, the measurement was conducted with a strictly sealed cell. Consequently, the measured α of the anode originating from reaction entropy change rapidly rises from +0.70 mV K^{-1} to +1.395 mV K^{-1} (+1.248 mV K^{-1} ~ +1.728 mV K^{-1}) as depicted in **Figure 4.2 c**. The overall α boosted up to -2.270 mV K^{-1} (-2.068 mV K^{-1} ~ -3.004 mV K^{-1}), which is the record-high value in TREC systems (**Figure 4.2d**). The fundamental analysis is based on the thermodynamics of

electrochemistry. **Figure 4.4a** depicts the entropy and energy change of the anode, cathode, and the full cell reaction. In short, the increasing temperature lowers the energy gap of full reaction, where the related analysis is given below in detail.

In our TREC system, the reactions are given below.

$$\begin{cases} \mathrm{NiHCF} + \mathrm{K^+} + \mathrm{e^-} \rightarrow \mathrm{NiHCF@K} & \Delta G_1 = -n_1 E_1 F \\ \frac{1}{2}\mathrm{Zn^{2+}} + \mathrm{e^-} \rightarrow \frac{1}{2}\mathrm{Zn} & \Delta G_2 = -n_2 E_2 F \end{cases} \tag{34}$$

$$n_1 = n_2 = 1 \tag{35}$$

The overall reaction:

$$\frac{1}{2}\mathrm{Zn} + \mathrm{NiHCF} + \mathrm{K^+} \rightarrow \mathrm{NiHCF@K} + \frac{1}{2}\mathrm{Zn^{2+}} \tag{36}$$

Thus, the overall voltage and the overall energy change of the full cell are shown below.

$$E_{overall} = E_1 + (-E_2) = \frac{\Delta G_2}{n_2 F} - \frac{\Delta G_1}{n_1 F} \tag{37}$$

$$\Delta G_{overall} = \Delta G_1 + (-\Delta G_2) = \Delta G_1 - \Delta G_2 \tag{38}$$

The overall energy change with temperature change can be expressed by thermopower $\boldsymbol{\alpha_1}$ and $\boldsymbol{\alpha_2}$.

$$\begin{aligned} \frac{\partial G_{overall}}{\partial T} &= \frac{\partial \Delta G_1}{\partial T} - \frac{\partial \Delta G_2}{\partial T} \\ &= -n_1 F \frac{\partial E_1}{\partial T} + n_2 F \frac{\partial E_2}{\partial T} \\ &= n_2 F \alpha_2 - n_1 F \alpha_1 \end{aligned} \tag{39}$$

In our systems, $\boldsymbol{\alpha_2}$ is positive while $\boldsymbol{\alpha_1}$ is negative, and the $\frac{\boldsymbol{\partial G_{overall}}}{\boldsymbol{\partial T}}$ is both positive in our NiHCF/Zn and NiHCF/$ZnNH_3$ systems implying that the overall Gibbs energy change increases with temperature. The $\boldsymbol{|\Delta G_{overall}|}$ decreases with increasing temperature. This is why the charging process is a thermodynamically favorable process at high temperatures.

For cathode, $\alpha_1 = \frac{\partial E_1}{\partial T}$ shows a negative value, as $\Delta S_1 = n_1 F \frac{\partial E_1}{\partial T}$, $\partial \Delta G_1 = -\Delta S_1 \partial T$, the cathode discharging reaction is a process of entropy and energy reduction (ΔS_1 and ΔG_1 are negative). As $\frac{\partial G_1}{\partial T}$ is positive, it indicates that the $|\Delta G_1|$ decreases with temperature. For anode, the $|\Delta G_2|$ decreases with temperature (α_2, ΔS_2 and ΔG_2 are positive, $\frac{\partial G_2}{\partial T}$ is negative). Therefore, for reaction $Zn^{2+} + 2e^- \rightarrow Zn$, the energy gap is shortened with temperature. Because $\Delta G_{overall} = \Delta G_1 - \Delta G_2$, ΔG_1 becomes more positive and ΔG_2 becomes more negative, and $\Delta G_{overall}$ tends to be more positive when the value is below zero, which means $|\Delta G_{overall}|$ decreases with increasing temperature.

Here should be noted that the thermopower is directional, that is, the thermopower of cathode corresponds to entropy change of the cathode discharge reaction, and the thermopower of anode corresponds to the opposite direction of the anode discharge reaction entropy change, so as to ensure that the energy change direction is consistent with the electrode potential. For example, the reaction $[Zn(NH_3)_4]^{2+} + 2e^- \rightarrow Zn + 4NH_3(aq)$, $\Delta S>0$, $\Delta G>0$, $E<0$, $\alpha>0$.

To sum up, the $|\boldsymbol{\Delta G_{overall}}|$ is higher at low temperature than that at high temperature. Regardless of the discharge or charge process, the energy gap presents the absolute value of energy change thus avoiding the direction problem of reaction voltage and energy. That is, the discharging process harvests exceeding energy through a voltage change by reducing the temperature. And the voltage change could be further amplified by promoting the thermopower in NiHCF/$ZnNH_3$ system. The calculation process is also applicable to other TREC system.

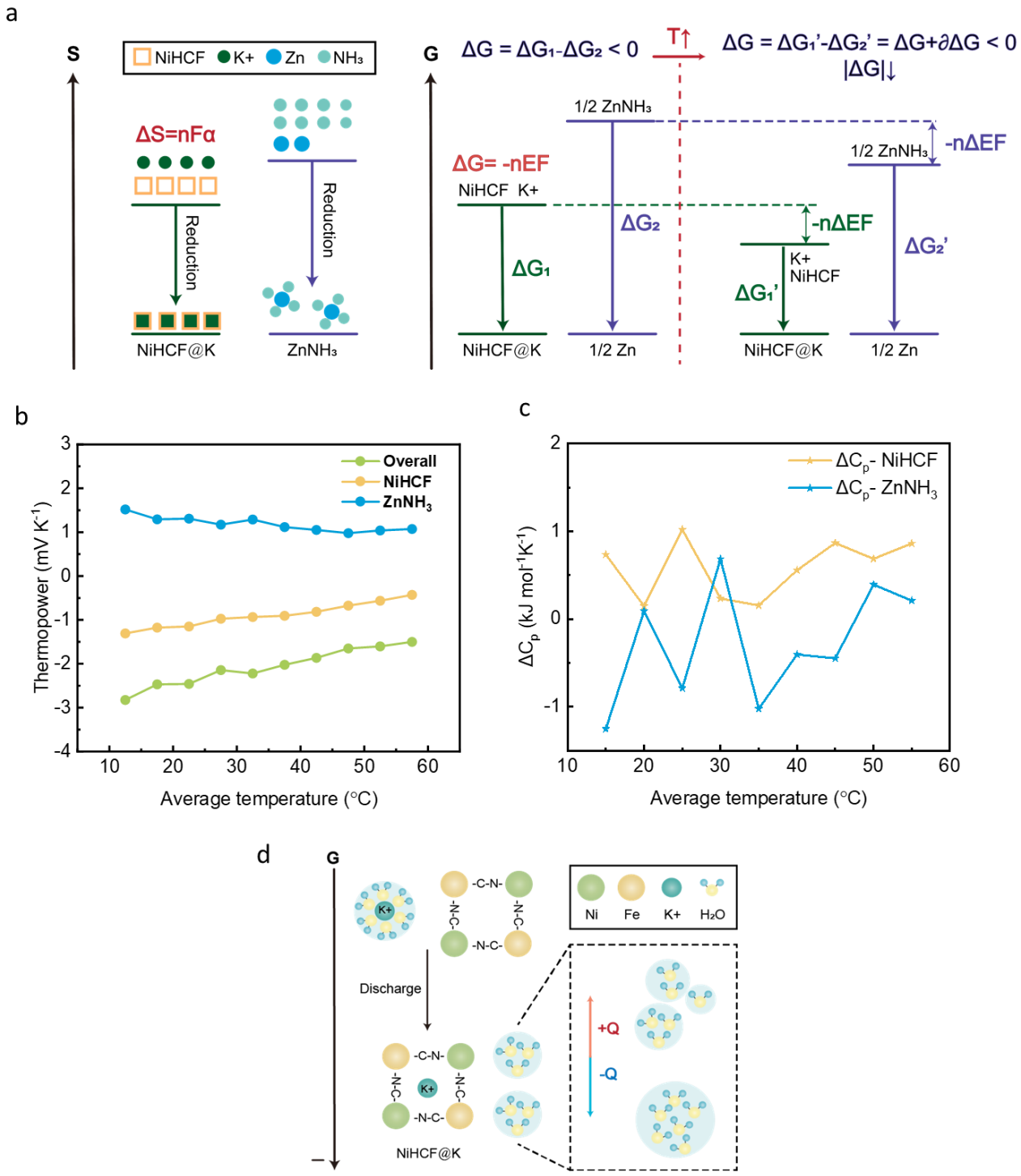

Figure 4.4. The entropy change and energy change of discharging electrochemical reaction. **a)** Schematic diagram of entropy and energy change of the reaction. **b)** α change of NiHCF and Zn electrode among the 10°C to 60°C temperature range. **c)** Overall heat capacity change $\Delta C_{p_{reaction}}$ of cathode and anode reaction. **d)** Schematic diagram of temperature influence in

reaction energy change.

Theoretically, when the activity of the solid phase is assumed to be 1, the potential can be calculated from the Nernst equation, and the temperature coefficient is calculated as -0.08617 mV K^{-1} if the activity is approximated to be constant regardless of temperature. In this work, we found that the α will change with temperature as shown in **Figure 4.4b**.

As it is assumed from previous work that the entropy change ΔS is constant, the α is also regarded as a constant. However, it should be noted that the entropy change of the system cannot be simply attributed to the entropy change of the electrochemical reaction. While the entropy term in equation 1 is a constant, actually it cannot be decoupled with system energy in non-ideal working fluids.[49] It implies that the entropy change of the reaction ΔS might change since reactants are an indispensable part of the system, yet the entropy of the system usually increases with increasing temperature. Therefore, a modified equation is given below:

$$nF\Delta E = \Delta(ST) + R\Delta(T\ln([C^+])) \quad (40)$$

where ΔE is OCV change, R, T, are the gas constant and temperature, and C^+ is the activity of monovalent cation. The equation is conducted and discussed blow.

The Gibbs free energy (G) is a function of temperature, pressure and chemical energy according to Maxwell's equations, $dG = -SdT + VdP + \sum_i \mu_i dn_i$, where S, T, V, P represent the entropy, temperature, volume, and pressure of the system respectively, $\sum_i \mu_i dn_i$ is the overall chemical energy change of each component. The electrochemical system proceeds under isobaric conditions, which means the value of dP is 0. The equation can be simplified to:

$$dG = -SdT + \sum_i \mu_i dn_i \quad (41)$$

For a certain electrochemical reaction, the reaction entropy change ΔS is relative to the energy change of this reaction ΔG. Then the change in reaction energy is reflected in the change of the equilibrium potential, equal to the measured OCV. So, the relations among thermopower (α), entropy (S), energy and potential are given as equation 42 to 44:

$$\Delta S = -\frac{\partial \Delta G}{\partial T} \quad (42)$$

$$\Delta G = -nEF \quad (43)$$

$$\Delta S = nF\frac{\partial E}{\partial T} = nF\alpha \quad (44)$$

NiHCF exhibits negative thermopower in this system, which means the equilibrium potential decreases with increasing temperature. It suggests that the cathode discharging reaction is an entropy decreasing reaction according to equation 44 (ΔS is negative) and Gibbs energy deceasing reaction from equation 43.

Theoretically, when the activity of the solid phase is assumed to be 1, the potential can be calculated from the Nernst equation:

$$E^{\theta'} = E^0 - \frac{RT}{nF}\ln([C^+]) \quad (45)$$

$$E^{\theta'} = E^0 - 0.08617\ mV\ K^{-1} \times \mathrm{Tln}([C^+]) \quad (46)$$

where $E^{\theta'}$ is the formal potential, E^0 is the standard electrode potential with the unit activity of ions, R, T, are the gas constant and temperature, and C^+ is the activity of monovalent cation. Equation 45 can be simplified to equation 46, where the temperature coefficient is counted as -0.08617 mV K^{-1} if the activity is approximated to be constant regardless of

temperature. The theoretical formal potential does not change much with temperature with the temperature coefficient of -0.08617 mV K^{-1}. As the Nernst equation is derived under isobaric and isothermal conditions, it is assumed in this equation that the energy is fully converted to chemical energy ($-SdT + VdP = 0$). However, when temperature changes, the $-SdT$ term is not zero which means only part of the energy is converted into chemical energy. Consequently, the Nernst equation should be modified by adding a supplementary item showing the entropy and temperature change effect on potential. That is the main contribution to the gap between equilibrium potential and formal potential (equation 47):

$$nF\Delta E = \Delta(ST) + R\Delta(T\ln([C^+])) \quad (47)$$

From **Figure 4.4c** and equation 42, the slope $\frac{\partial \Delta S}{nF\partial T} = \frac{\partial \alpha}{\partial T}$ indicates the reaction entropy change with temperatures. Since the increase of temperature results in smaller water molecular groups,[101] which could be also proved by Raman, it illustrates the influence of dehydrated water on the reaction entropy change as depicted in **Figure 4.4d** and **Figure 4.5**.

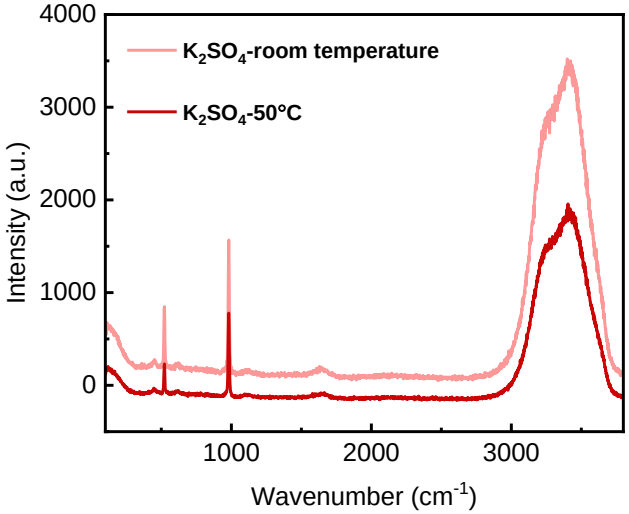

Figure 4.5. Raman spectra of 0.5 M K_2SO_4 at 25°C room temperature and 50°C.

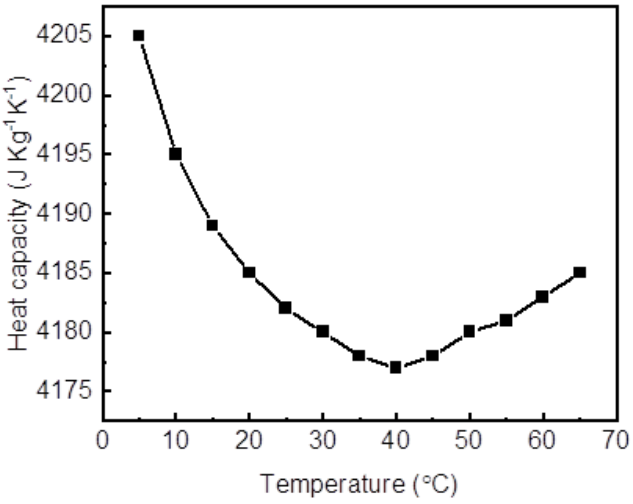

Figure 4.6. Pure water heat capacity change with temperature.[102]

Since increasing temperature results in smaller water molecular groups,[101] the proportions of monomer, dimer, and trimer water increase with increasing temperature, but decrease in tetramer, pentamer, hexamer. That is caused by the destroyed OH bonding at high temperature as shown in **Figure 4.5** that the OH vibration mode peak integrated intensity decreases with increasing temperature. The characteristic peak at 1633 cm^{-1} and the stretching mode from 2800 to 3800 cm^{-1} exhibits OH vibrations. The OH peak has almost the same position at both high and low temperatures regardless of the cation and anion, but the integrated intensity decreases with increasing temperature. It indicates the OH bonding is weakened at high temperature, which can be inferred that the OH bond network is destroyed. As is seen in this figure, the SO_4^{2-} vibration mode at 983 cm^{-1} demonstrates a linewidth increasing from room temperature to high temperature, which can be attributed to structure disordering.[103] This structure disorder is related to the weakened hydrogen bonding at high temperatures so that interatomic distances increase, resulting in the polarizing power of cation

decreasing and consequently sulfate wavenumbers decreasing.

Therefore, so far, we have theoretically and experimentally proved the reaction entropy change is not constant but temperature dependent, thereby causing a non-linear change in voltage with temperature.

In order to further predict the thermopower change, a series of physical quantities were introduced into this isobaric system to explore the physical meaning of thermopower change with temperature $\frac{\partial \alpha}{\partial T}$. The calculation process is shown as follows from equations 48 to 51:

$$\Delta H = \Delta(G + TS) = -nEF + nFT\alpha \tag{48}$$

$$\Delta H = \Delta H_{T_1} + \int_{T_1}^{T} (\sum_I \nu_i \, \Delta C_p) dT \tag{49}$$

$$\Delta C_{p_{reaction}} = \sum_I \nu_i \, \Delta C_p = \sum_{products} \nu_i C_p - \sum_{reactants} \nu_i C_p \tag{50}$$

$$\Delta C_{p_{reaction}} = \frac{\partial \Delta H}{\partial T} = nFT \left(\frac{\partial \alpha}{\partial T}\right) \tag{51}$$

where ΔH represents reaction enthalpy change, constant ΔH_{T_1} is heat of reaction at a single temperature T_1, $\Delta C_{p_{reaction}}$ is the overall heat capacity change of a reaction which can be expressed as the difference of products' heat capacity and reactants' heat capacity, where ν_i is stoichiometric number and C_p is the corresponding heat capacity, ΔC_p is the heat capacity change. It can be seen that the changing thermopower is actually related to the reaction heat capacity change. Heat capacity C_p can be determined as a function of temperature below (equation 52):

$$C_p = a + bT + cT^2 \tag{52}$$

where a, b, c are the constants whose values are different for different materials. For example, the heat capacity of water is not a constant within 10℃~60℃ range and it is the

lowest at around 40°C (**Figure 4.6**). From equation 51 to 52, it could be seen that $\frac{\partial \alpha}{\partial T}$ is not zero if $\Delta C_{p_{reaction}}$ is not zero.

For instance, the actual cathode reaction including water molecules is $KNi^{II}Fe^{III}(CN)_6 + [K(H_2O)_6]^+ + e^- \rightarrow K_2Ni^{II}Fe^{II}(CN)_6 + 6H_2O$. The estimated cathode overall reaction heat capacity change is $\Delta C_{p_{reaction}} = 6C_{p_{H_2O}} - C_{p_{[K(H_2O)_6]^+}}$ as the heat capacities of most metals and simple crystalline solids are similar and stable at room temperature. Since the water heat capacity reaches minimum value of 4.1796 J g^{-1} K^{-1} at 40°C while the hydration heat capacity $C_{p_{[K(H_2O)_6]^+}}$ decreases only very slightly with temperature,[104] the theoretical minimum value of overall reaction heat capacity should be obtained at around 40°C due to the lowest heat capacity of water at ~40°C (**Figure 4.6**) which is in line with our results (~35°C) from **Figure 4.4c**. The estimated anode reaction heat capacity change is $\Delta C_{p_{reaction}} = 4C_{p_{NH_3H_2O}} + C_{pZn} - 4C_{p_{H_2O}} - C_{p_{[Zn(NH_3)_4]^{2+}}} \approx 4C_{p_{NH_3 \cdot H_2O}} - 4C_{p_{H_2O}} + C$, where C is regarded as a constant. The heat capacity change is found to increase with increasing temperature when temperature is higher than 30°C (**Figure 4.4c**) due to the significant increase of $C_{p_{NH_3 \cdot H_2O}}$ with temperature (about 4.2468 J $g^{-1}K^{-1}$ at 10°C, 4.3095 J $g^{-1}K^{-1}$ at 60°C (10 wt% NH_3)[105]) to $C_{p_{H_2O}}$ (4.1955 J $g^{-1}K^{-1}$ at 10°C, 4.1851 J $g^{-1}K^{-1}$ at 60°C).[106]

It is still difficult to quantitatively predict the thermopower change in spite of using heat capacity change of reaction $\Delta C_{p_{reaction}}$. The complexity introduced by such a thermo-electrochemical system makes the integration of thermodynamic rules more difficult. In addition to the heat capacity change, the K_2SO_4 electrolyte used in the system is almost

saturated at room temperature and crystallization is easier at low temperature. Similar to the K_2SO_4, the solubility of $(NH_4)_2SO_4$+$ZnSO_4$ decreases with addition of ammonia.[107] Moreover, the simultaneous evaporation of both water and ammonia requiring additional heat might occur inside the system apart from the electrolyte recrystallization-dissolution process. By introducing the additional dissolution ($\Delta H_{diss_{K_2SO_4}} = 37.39\ kJ\ mol^{-1}$)[108] and vaporization heat ($\Delta H_{vap_{H_2O}} = 40.65\ kJ\ mol^{-1}$, $\Delta H_{vap_{NH_3}} = 23.37\ kJ\ mol^{-1}$)[109], the unexpectable heat capacity change could be brought in system then affects ΔC_p a lot. That might be the reason of fluctuation of ΔC_p.

In order to clearly understand the relations among the physical quantities in this chapter, the aforementioned equations have been organized into **Table 4.2.**

Table 4.2. The meaning and unit of referred physical quantities.

Parameter	Name	Unit	Equation
α	Thermopower/temperature coefficient	mV K^{-1}	$\alpha = \frac{\sigma E}{\sigma T} = \frac{\Delta S}{nF}$
ΔS	Entropy change	kJ mol^{-1}K^{-1}	$\Delta S = -\frac{\partial \Delta G}{\partial T}$ $\Delta S = nF\frac{\partial E}{\partial T} = nF\alpha$ $nF\Delta E = \Delta(ST) + R\Delta(T\ln([C^+]))$
$E^{\theta'}$	Formal potential	V	$E^{\theta'} = E^0 - \frac{RT}{nF}\ln([C^+])$
ΔG	Gibbs energy change	kJ mol^{-1}	$\Delta G = -nEF$ $dG = -SdT + VdP + \sum_i \mu_i dn_i$

			$dG = -SdT + \sum_i \mu_i dn_i$ (isobaric)
ΔH	Enthalpy change	kJ mol^{-1}	$\Delta H = \Delta G + T\Delta S = -nEF + nFT\alpha$ $\Delta H = \Delta H_{T_1} + \int_{T_1}^{T} (\sum_I \nu_i \Delta C_p) dT$
$\Delta C_{p_{reaction}}$	Heat capacity change	kJ mol^{-1} K^{-1}/ J g^{-1} K^{-1}	$\Delta C_{p_{reaction}} = \sum_{products} \nu_i C_p - \sum_{reactants} \nu_i C_p$ $\Delta C_{p_{reaction}} = \frac{\partial \Delta H}{\partial T} = nFT\left(\frac{\partial \alpha}{\partial T}\right)$ $C_p = a + bT + cT^2$
η	Efficiency	-	$\eta = \frac{W}{T_H \Delta S + (1 - \eta_{HR}) C_{p_{cell}} \Delta T}$
η_c	Carnot efficiency	-	$\eta_c = \frac{T_H - T_L}{T_H}$
η_r	Relative efficiency	-	$\eta_r = \frac{\eta}{\eta_c}$
W	Energy density	mWh g^{-1}/J g^{-1}	$W = Q_{dis}(\overline{V}_{dis} - \overline{V}_{ch}/CE)$
P	Power density	mW g^{-1}/ mW m^{-2}	$P = \frac{(\overline{V}_{dis} - \overline{V}_{ch})I}{2}$

4.4 Effects of Temperature

To investigate the effects of temperature on the kinetics process and cyclic voltammetry at different temperatures was conducted. A series of parameters were analyzed and shown in **Figure 4.7 a-b**.

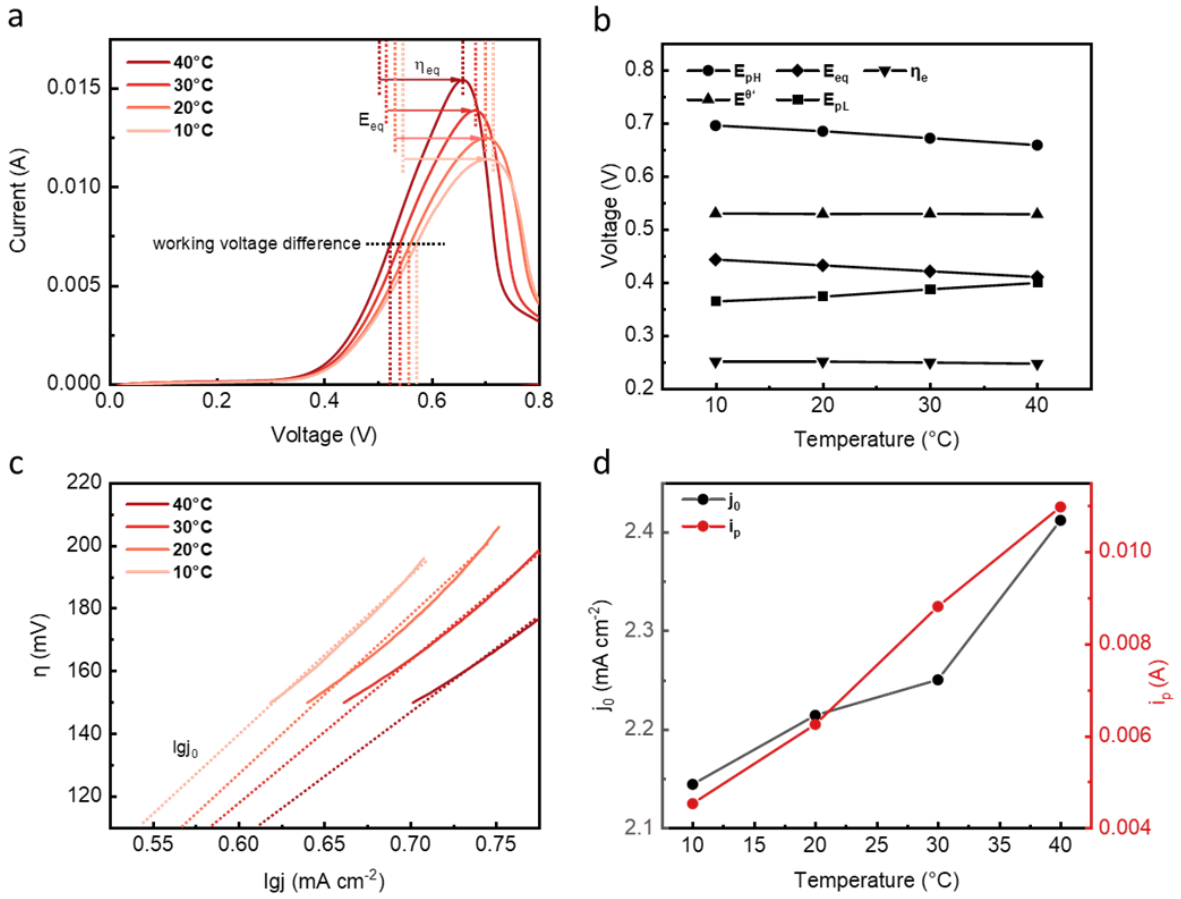

Figure 4.7. The cyclic voltammetry (CV) curves of NiHCF in 0.5 M K_2SO_4 and kinetics parameters analysis in electrode reaction. **a)** The half CV curve of NiHCF from 10°C to 40°C with the sweeping speed of 1 mV s^{-1}. E_{eq} is the equilibrium potential, η_e is the overpotential controlled by charge transfer step. **b)** The various potentials of NiHCF from 10°C to 40°C. $E^{\theta'}$, E_{pH} and E_{pL} represent formal potential, high and low peak voltage respectively, the sweeping speed is 1 mV s^{-1}. **c)** The linear fitting to extrapolate exchange current density from 10°C to 40°C. The overpotential can be expressed linearly to lg j where j is current density. The intercept on the x axis represents lg j_0, j_0 is exchange current density. **d)** The obtained exchange current density from **Figure 4.7c** and peak current from **Figure 4.7a**.

Firstly, the equilibrium potential was measured based on the OCV. The OCV represented the equilibrium state of the electrode when the net current was zero. As the equilibrium potential (E_{eq}) decreased from 0.444 V at 40 ℃ to 0.411 V at 10 ℃ (corresponding to an α of -1.100 mV K^{-1}), the formal potential ($E^{\theta'}$) from CV curve was experimentally measured as the midpoint of two peak voltages (E_{pH} and E_{pL}) and stabilized at approximately 0.530 V vs. Ag/AgCl reference electrode with a small slope of -0.0483 mV K^{-1} from 0.530 V at 10 ℃ to 0.529 V at 40 ℃, as depicted in **Figure 4.7b**. The result is consistent with the tendency of the calculated temperature coefficient from the coefficient of Nernst equation (-0.08617 mV K^{-1}).

Secondly, with increasing temperature, the two gradually approaching peaks (E_{pH} and E_{pL}) indicated better reversibility, presenting higher exchange current density and reaction rate. Exchange current density was obtained by linear fitting in the overpotential region of 150-200 mV (**Figure 4.7c**). The exchange current density increased gradually from 2.145 mA cm^{-2} at 10°C to 2.412 mA cm^{-2} at 40°C, as shown in **Figure 4.7d**.

Thirdly, the increasing peak current (**Figure 4.7d**) demonstrated higher diffusion rates at higher temperatures. For an ion intercalation process, the rate-determining step is usually the diffusion movement of ions in the lattice.[110] The peak current i_p can be determined as equation 53 (Randles-Sevcik equation):

$$i_p = 0.4463\, nFAC\left(\frac{nFvD}{RT}\right)^{\frac{1}{2}} \quad (53)$$

where A is electrode area, C is electrolyte concentration, v is scan rate, D is diffusion coefficient and R is the ideal gas constant. The peak current is positively related to $(D/T)^{-1/2}$ at a certain sweeping rate and concentration. As is shown in **Figure 4.7d**, the increasing peak

current from 0.0119 A to 0.0154 A demonstrated a faster diffusion process and less diffusion overpotential loss at high temperatures. The possible lattice expansion of NiHCF was proved by the peak shift of X-ray Diffraction pattern (**Figure 4.8**). That attributes to the lattice expansion of NiHCF at a high temperature, leading to faster movement during intercalation.

These results further supported the positive effect of temperature on the kinetic process. A better kinetic performance including better reversibility and lower mass transfer resistance was illustrated by the higher exchange current density and diffusion rate, further confirming that a high temperature facilitates the kinetic process.

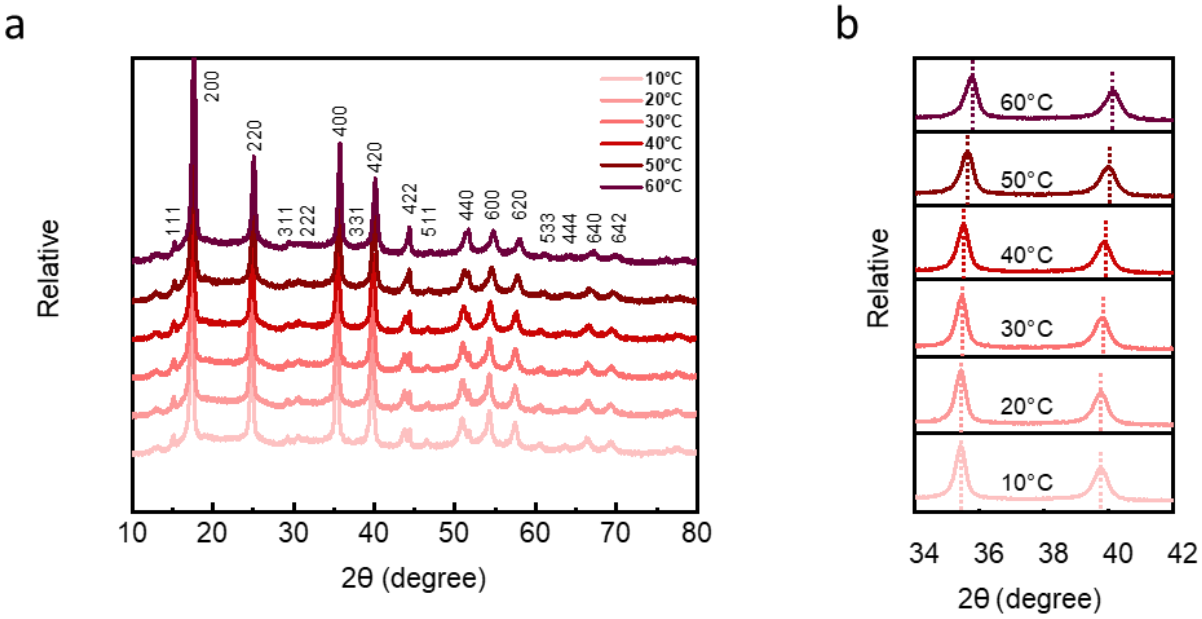

Figure 4.8. The XRD pattern of NiHCF particles. **a)** The XRD pattern of NiHCF, indicating its face-centered cubic Fm-3m space group. **b)** The (400) and (420) peak shift with temperature from 10℃ to 60℃.

4.5 Performances

For the sake of comprehensive comparison on performance from different aspects, parameters including η (efficiency), η_r (efficiency related to Carnot efficiency), P (power density) will be discussed. These parameters have been also sorted out in the fowling **Table 4.3.**

Table 4.3. The information of parameters related to performances.

Parameter	Name	Unit	Equation
η	Efficiency	-	$\eta = \frac{W}{T_H \Delta S + (1-\eta_{HR}) C_{p_{cell}} \Delta T}$
η_c	Carnot efficiency	-	$\eta_c = \frac{T_H - T_L}{T_H}$
η_r	Relative efficiency	-	$\eta_r = \frac{\eta}{\eta_c}$
W	Energy density	mWh g^{-1}/J g^{-1}	$W = Q_{dis}(\overline{V}_{dis} - \overline{V}_{ch}/CE)$
P	Power density	mW g^{-1}/ mW m^{-2}	$P = \frac{(\overline{V}_{dis} - \overline{V}_{ch})I}{2}$

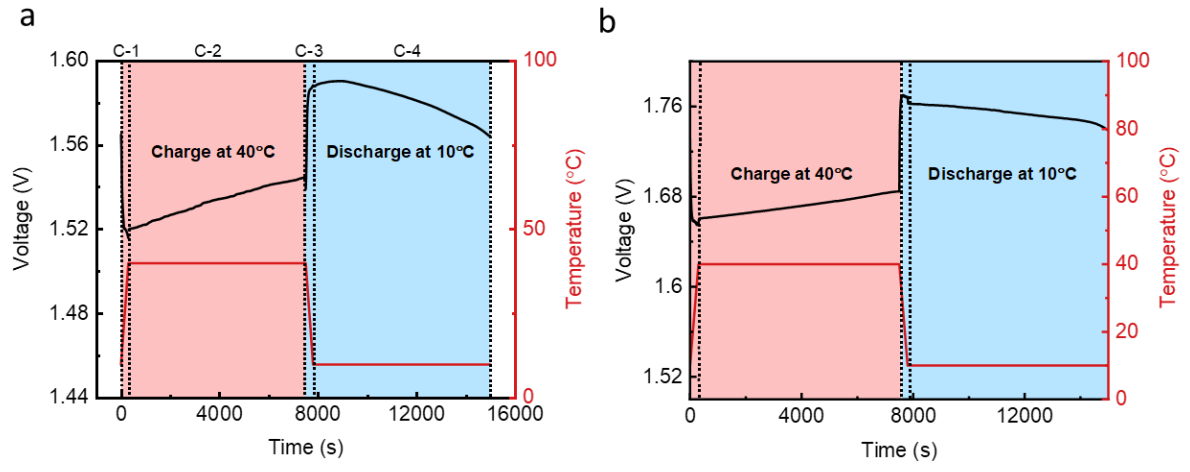

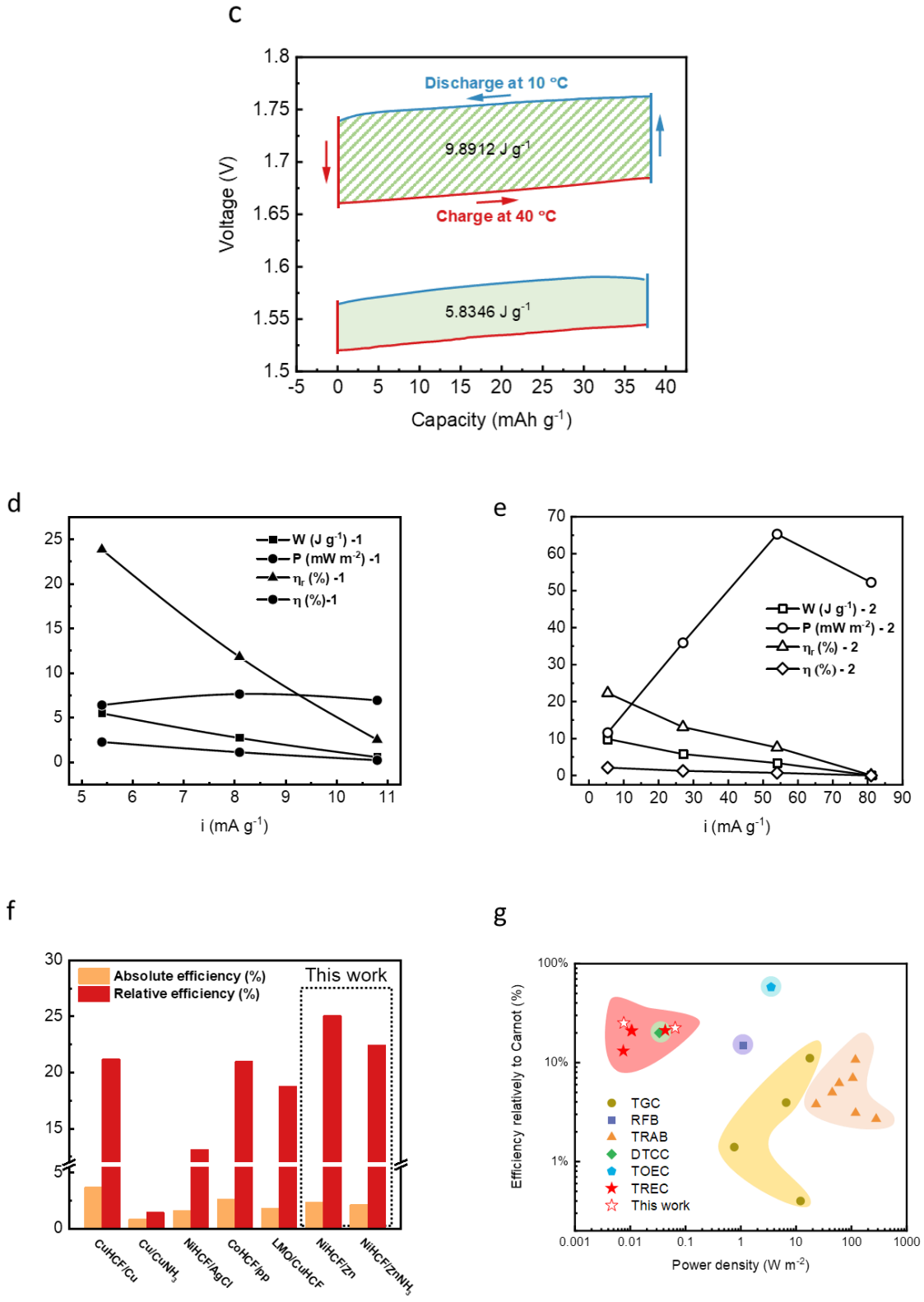

Figure 4.9. The full cell performance with NiHCF cathode and Zn anode. **a)** The voltage change for the whole cell during a full TREC cycle. The NiHCF-Zn cell was operated between

10°C to 40°C at a current density of 5.4 mA g^{-1}, including C-1 heating up, C-2 charging, C-3 cooling down, and C-4 discharging. **b)** The voltage change for the whole cell during a full TREC cycle. The NiHCF-$ZnNH_3$ cell was operated between 10°C to 40°C at a current density of 5.4 mA g^{-1}. **c)** The full NiHCF/Zn cell capacity plot versus voltage of the whole cycle consistent to Figure 2.6a and b. The corresponding energy density is 5.8346 J g^{-1} (per electrode mass). The full NiHCF/$ZnNH_3$ cell capacity plot versus charging-discharging voltage with 0.1 C current density (5.4 mA g^{-1}) which is as same as the charging-discharging condition as NiHCF-Zn. The corresponding energy density is 9.8912 J g^{-1} (per electrode mass). **d)** The relative efficiency, efficiency, energy density and harvested output power of 0.1 C, 0.15 C, 0.2 C current density with 5.4 mA g^{-1}, 8.1 mA g^{-1}, 10.8 mA g^{-1} within 10°C to 40°C temperature range (η_{HR}=0). 1 represents NiHCF/Zn system. **e)** The relative efficiency, efficiency, energy density and harvested output power at current of 0.1 C (5.4 mA g^{-1}), 0.5 C (27.0 mA g^{-1}), 1 C (54.0 mA g^{-1}), 1.5 C (81 mA g^{-1}) and at temperature gap of 30ºC (10°C to 40°C) (η_{Hr}= 0). 2 represents NiHCF/$ZnNH_3$ system. **f)** The performance comparison including efficiency, relative efficiency and α. The systems include CuHCF/Cu, [47] NiHCF/AgCl, [48] CoHCF/pp[98] and LMO/CuHCF.[72] **g)** The relative efficiency and power density of different systems.

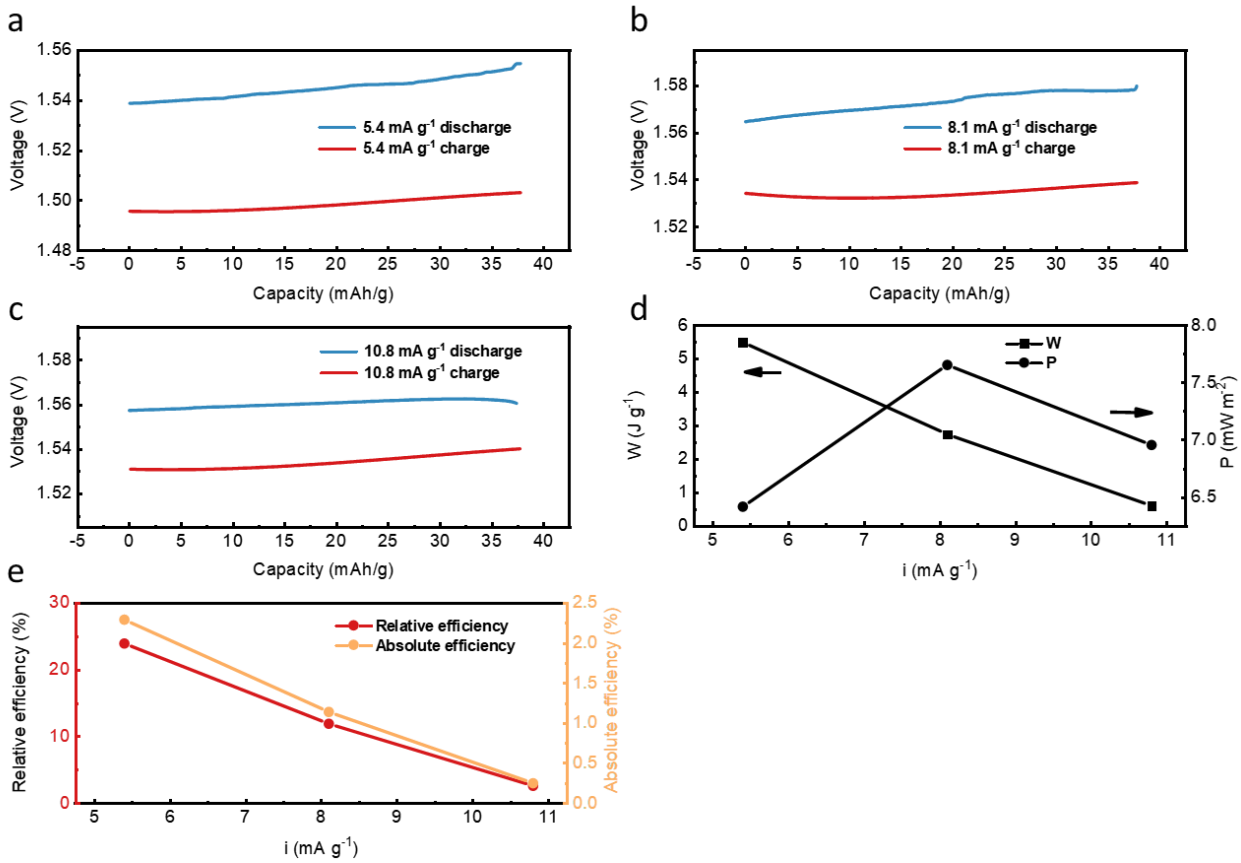

Figure 4.10. The performance of NiHCF/Zn system (from 80% SOC to 100% SOC). **a)** The TREC cycle with 30°C temperature difference at 5.4 mA g^{-1} (0.1 C). **b)** The TREC cycle with 30°C temperature difference at 8.1 mA g^{-1} (0.15 C). **c)** The TREC cycle with 30°C temperature difference at 10.8 mA g^{-1} (0.2 C). **d)** The power density at different current density. **e)** The relative efficiency and absolute efficiency ($\boldsymbol{\eta_{HR} = 0}$) at different current density.

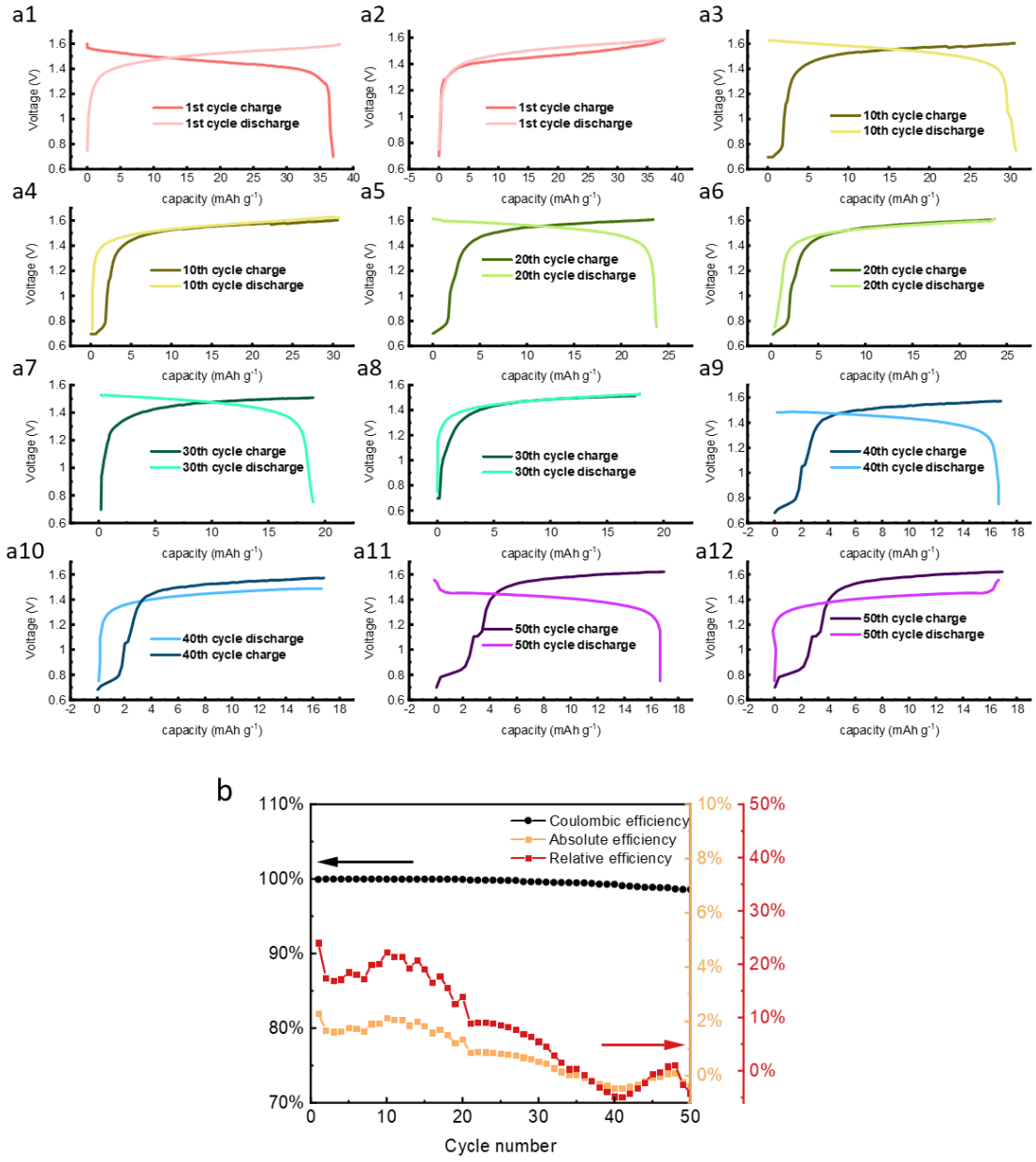

Figure 4.11. The cycle life of NiHCF/K_2SO_4/Zn system. **a)** The TREC cycle life with 30℃ temperature difference at 5.4 mA g^{-1} (0.1 C). The 50 cycles with 30℃ temperature difference at 5.4 mA g^{-1} current density, the cell is fully charged and discharged. The cycling end discharging voltage is 0.65 V and the end charging voltage is 1.6 V. **b)** The relative efficiency, absolute efficiency ($\boldsymbol{\eta_{HR} = 0}$) and coulomb efficiency of 50 cycles.

Table 4.4. The performance comparison. Parameters include α, temperature difference ΔT, energy density W, efficiency η, relative efficiency η_r and recuperation efficiency η_{HR}. The systems include CuHCF/Cu, [47] NiHCF/AgCl, [48] CoHCF/pp[98] and LMO/CuHCF.[72]

System	α_{cell} (mV K^{-1})	ΔT	W J/g	η (%)	η_r (η/η_c , %)	η_{HR}
CuHCF/Cu	-1.2	50.000	5.200	3.7	21.2	0
NiHCF/AgCl	-0.74	40.000	1.000	1.6	13.12	0
CoHCF/pp	-0.89	40.000	2.052	2.65	21	0
LMO/CuHCF	+1.061	30.000	0.970	1.8	21	0
NiHCF/Zn	-1.575	30.000	5.8346	2.40	25.16	0
NiHCF/$ZnNH_3$	-2.270	30.000	9.8912	2.17	22.66	0

The α of the full cell reached -1.575 mV K^{-1}. Assembled TREC full pouch cell was composed of NiHCF cathode, Zn metal anode, and the two electrodes were separated by a normal pp separator which was soaked with 0.5 M K_2SO_4 electrolyte. The electrodes were prepared with an area of 1×2 cm^2 and a material loading of 7 mg cm^{-2} (70% active material of NiHCF). The full cell achieved a high specific capacity of 54 mAh g^{-1} (active material mass) / 37.8 mAh g^{-1} (electrode mass). To enable a complete TREC cycle, the cell was sandwiched between two thermoelectric plates (controlled temperature ± 0.01°C) and two thermocouples were inserted. As is shown in Figure 2.6a, the cell was heated up to 40°C within 5 minutes, which dramatically decreased the voltage by about 50 mV. The charging process was then

implemented at 40°C under 0.1C current density (equivalent to 5.40 mA g^{-1}) from 80% state of charge to 100% state of charge for 2h. The overpotential was approximately 3.5 mV at the beginning of charging process and the average charging voltage was 1.5334 V. The working temperature range was designed by considering the electrode stability. As shown in **Figure 4.9a-c**, after cooling down to 10°C, the discharging process was conducted at the same current density with an average discharging voltage of 1.5814 V and an overpotential of 5 mV. The energy density of 5.8346 J g^{-1} was obtained with the high coulombic efficiency of 99.66%, corresponding to an efficiency of 2.410% and a relative efficiency to Carnot efficiency of 25.155%. The efficiency and relative efficiency were increased to 4.868% and 50.81%, respectively, with a recuperation efficiency of 70%. To examine the current effect, a full cell was tested at 5.40 mA g^{-1}, 8.10 mA g^{-1}, 10.80 mA g^{-1} current density respectively with 30°C temperature difference (**Figure 4.10**). The larger current density caused higher overpotential.

As shown in **Figure 4.9d**, the energy density, efficiency and relative efficiency all decreased almost linearly with current density. At a discharge current of 8.1 mA g^{-1}, the cell achieved the highest power output with good efficiency. The cell can be operated for more than 30 fully charge-discharge cycles (whose time scale equals to 150 cycles of 80% SOC to 100% SOC cycle as shown in **Figure 4.9b**) at a current density of 5.4 mA g^{-1}. The fully charged and discharged cell achieved an energy efficiency of 2.30%, which was 24.01% that of the Carnot efficiency. Thanks to excellent coulombic efficiency of NiHCF like Prussian blue analog material,[111] it exhibits good reversibility. However, the side reaction of hydrogen evolution due to the large potential window contributes to additional $Zn(OH)_2$ product, resulting in higher

resistance and Ohmic loss, which further decreases the efficiency.

To avoid the side reaction of NH_3 (aq) and NiHCF, the mixed membrane (AEM/CEM) was used to separate the catholyte and anolyte. The same temperature range used for the NiHCF/K_2SO_4/Zn system was adopted to prevent ammonia vaporization. With a higher α of -2.270 mV K^{-1}, a large voltage gap of more than 70 mV was established with a temperature difference of only 30°C. Thus, a harvested energy density of 9.8912 J g^{-1} is obtained at a discharging voltage of 1.7596 V and a charging voltage of 1.6719 V. As a result, the cell achieved an energy efficiency of 2.171% and a relative efficiency of 22.663% of the Carnot efficiency. With a recuperation efficiency of 70%, a higher energy efficiency of 4.835% was achieved, which corresponded to a relative efficiency of 50.468% of Carnot efficiency (**Figure 4.11**). Interestingly, the overpotential in this system is similar to the overpotential in NiHCF/K_2SO_4/Zn system (around 5 mV at 0.1 C) when the same current density is applied. It indicates that the cell resistance not only relies on membrane resistance, but also depends on the concentration of electrolyte. As shown in **Figures 4.9d-e**, the maximum power density is almost seven times that of NiHCF/K_2SO_4/Zn system. However, due to the intrinsic diffusion of ammonia, the α and the equilibrium voltage of this system can only be maintained for around 7 cycles. Though different types of strictly sealed cells were tried to prevent the side reaction of NH_3 and NiHCF, the cell capacity degradation happened and the α decreased to around -1.7 mV K^{-1} after a few cycles which similar to the NiHCF/K_2SO_4/Zn system. As depicted in **Figure 4.9f-g**, the two systems show great performance in terms of relative efficiency and absolute α.

The energy efficiency highly depends on the temperature gap so that this high efficiency

obtained at a 30°C difference is very satisfactory compared with previous literature (40-50°C). As the Carnot efficiency represents the maximum efficiency for heat-to-power conversion by a thermodynamic cycle, the relative efficiency to Carnot efficiency was a better indicator to evaluate the performance of the energy system. With the same recuperation efficiency as demonstrated in **Figure 4.9f** and **Table 4.3**, the reported performance data were summarized and compared. Our two systems perform excellent relative efficiency owning to their high α. Although the power density is relatively low compared with other systems according to **Figure 4.9g**, the design of this work provides a new possibility to further improve the performance. The related information in **Figure 4.9g** is given in the following **Table 4.5**.

Table 4.5. Performance comparison among different systems.

Systems	Structure	|αcell| (mV K^{-1})	η (%)	η_r (%)	Power density (W m^{-2})	Ref.
TGC	Electrode: Multi-walled carbon nanotubes (MWCNT) based electrode Electrolyte: $[Fe(CN)_6]^{3-}/[Fe(CN)_6]^{4-}$	1.4	0.24	1.4	0.76	[34]
	Electrode: Carbon-based material Electrolyte: $K_3[Fe(CN)_6]/(NH_4)_4[Fe(CN)_6]$ or $Fe_2(SO_4)_3/FeSO_4$	1.85	0.11	0.4	12	[36]
	Electrode: CNT aerogel sheets Electrolyte: $K_3Fe(CN)_6/K_4Fe(CN)_6$	1.43	0.55	3.95	6.6	[44]
	Electrode: graphite plate Electrolyte: $K_3Fe(CN)_6/K_4Fe(CN)_6$+ GdmCl	3.73	1.62	11.1	17.7	[19]

RFB	Electrode: carbon cloth Electrolyte: $[Fe(CN)_6]^{3-}$ /$[Fe(CN)_6]^{4-}$ and V^{3+}/V^{2+}	3.0	1.8	15	1.1	[8]
TRAB	Electrode: Cu Electrolyte: $Cu(NO_3)_2/NH_4NO_3$	-	0.86	6.2	60	[61]
	BTMA-TRAB Electrode: Cu Electrolyte: $Cu(NO_3)_2/NH_4NO_3$	-	0.97	7.0	106	[62]
	TRENB Electrode: Cu Electrolyte: $Cu(NO_3)_2/NH_4NO_3$/ethylenediamine	-	0.52	3.1	119	[84]
	Ag-TRAB Electrode: Ag Electrolyte: $AgNO_3/NH_4NO_3$	-	0.41	3.8	23	[85]
	Cu-TRAFB Electrode: Cu Electrolyte: $Cu(NO_3)_2/NH_4NO_3$	-	0.70	5.0	45	[86]
	Cu/Zn-TRAB Electrode: Cu/Zn Electrolyte: $Zn(NO_3)_2$/ $Cu(NO_3)_2/NH_4NO_3$	-	0.95	10.7	118	[87]
	Cu/Zn-TRAFB Electrode: Cu/Zn Electrolyte: $Zn(NO_3)_2$/ $Cu(NO_3)_2/NH_4NO_3$	-	0.34	2.7	280	[11]
DTCC	Electrode: GO/PtNPs and PANI Electrolyte: $FeCl_2/FeCl_3$	5	3.52	20	0.0336	[113]
TOEC	Electrode: - Electrolyte: water	-	7	58	3.53	[63]
TREC	Electrode: CuHCF/Cu	1.2	3.7	21.2	0.043	[47]

Electrolyte: $NaNO_3$					
Electrode: NiHCF/AgCl Electrolyte: KCl	0.74	1.6	13.12	0.0075	[48]
Electrode: CoHCF/pp Electrolyte: NaCl	0.89	2.65	21	0.0105	[98]
Electrode: LMO/CuHCF Electrolyte: KNO_3+$LiNO_3$	1.06	1.8	21	0.01078	[72]
Electrode: NiHCF/Zn Electrolyte: K_2SO_4	1.58	2.4	25.16	0.00765	This work
Electrode: NiHCF/Zn Electrolyte: K_2SO_4/ $(NH_4)_2SO_4$+$NH_3 \cdot H_2O$	2.44	2.15	22.44	0.065	This work

4.6 Conclusions

This study explored the effects of temperature on entropy change and energy change of both systems and electrochemical reactions due to the lack of comprehensive research on the mechanism of heat-to-electricity energy conversion. A theoretical framework was built and equations among a series of thermodynamic parameters were derived in order to illuminate the origins of the α and to identify ways of enhancing the α. We found that the increased temperature changes the reaction heat capacity, which further affects the α. We also investigated the intrinsic energy conversion mechanism including the thermodynamics and kinetics processes. It is found that high temperature has a positive impact on both the thermodynamics and kinetics processes. For the thermodynamics process, the high temperature

lowers the energy gap for heat energy utilization. For the kinetics process, the high temperature lowers the energy gap, accelerates mass transfer process, and lowers overpotential.

CHAPTER 5 Thermally Regenerative CO_2-induced PH-Gradient Cell for Waste to Energy Conversion

5.1 Introduction

Based on the above research, we have obtained an optimized system of TREC. However, increasing the thermopower does not significantly increase the power density, which is determined by the intrinsic characteristics of TREC itself. Further optimization of the TREC system had limited impact on its performance. To explore alternative approaches for improving the power density, we were inspired by the thermally regenerative ammonia battery (TRAB) system, which is known for its high power density. Specifically, we investigated the possibility of modifying the ammonia in the TRAB system to design a novel system that could reduce the risks of corrosion of metal electrodes and pollution from ammonia leaks, while preserving the high power densities of the TRAB system.

The massive increase in waste CO_2 has aroused widespread social concerns due to its intense impacts on the global environment and climate.[114] Incessant combustion of carbon-based fuels, as the primary energy sources, produce relentless CO_2 and ubiquitous waste heat; a majority of this waste heat is regarded as low-grade heat and is usually dumped into the environment without use. Under this circumstance, CO_2 is a good option to achieve our goals.

Here, a new low-grade thermally regenerative CO_2-induced pH-gradient cell (TRCPC) is proposed to recycle waste CO_2 and thereby produce durable electricity. It was designed by using pH-sensitive electrodes in a carbonate-based absorbent, which has unique advantages including low cost, non-toxicity, and can be regenerated by using low-grade heat[115,116] to allow system cyclability. The TRCPC achieved a satisfying peak power density of 0.578 W m^{-2} with a long discharge time, which is comparatively over 10 times longer than the previous works.[117]

The structure and working mechanism of TRCPC are presented in **Figure 5.1a** and **5.1b**, respectively. A symmetric cell with two MnO_2/MnOOH electrodes is initially filled with 0.5 M sodium carbonate (Na_2CO_3) for both anolyte and catholyte. When CO_2 flows into the catholyte, part of Na_2CO_3 absorbs CO_2 and becomes sodium bicarbonate ($NaHCO_3$) so that a pH difference between the anolyte and catholyte side is established to build a potential difference through two pH-sensitive MnO_2/MnOOH electrodes. When discharging, the protons in the catholyte intercalates into the manganese dioxide while the anode experiences a reverse reaction. The pH gradient gradually decreases during the process until a CO_2 saturation state is reached. Afterward, $NaHCO_3$ can be thermally regenerated to Na_2CO_3 then the CO_2 can be further stored. Finally, the two electrodes can be swapped to fully exploit their ratio of oxidation and reduction states.

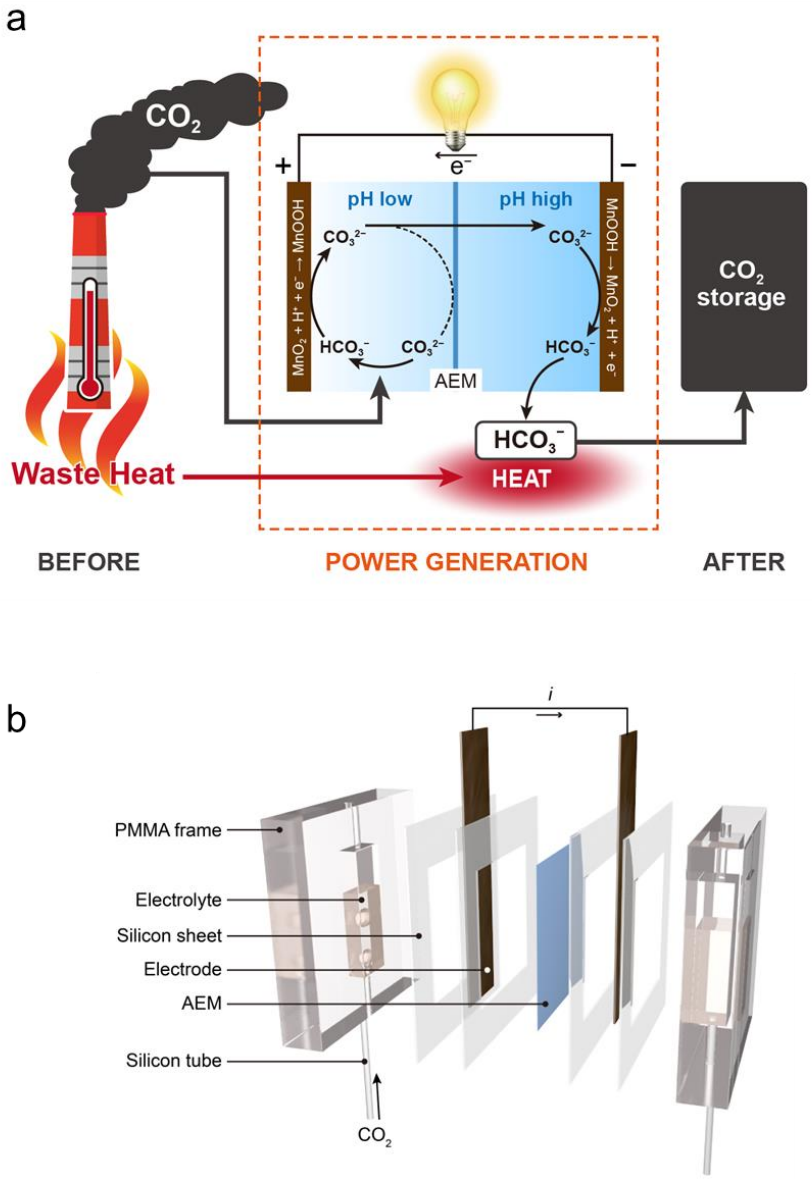

Figure 5.1. Schematic of the cell components and operation of the proposed heat-induced CO_2-based electrochemical cycle. **a)** Mechanism of the TRCPC. **b)** Structure of a TRCPC cell. Two 10 cm silicone tubes (ϕ 1.5×0.25 mm) were sealed in PMMA frame with two corresponding 2 mm air vents. The electrodes and anion exchange membrane are separated by two silicone sheets. One-third of the cell is left empty to prevent overflow of the 0.5 M Na_2CO_3 electrolyte.

5.2 Experimental Section

5.2.1 Experimental Overview

The experimental section follows the order of synthesis of active material, preparation of the electrodes and fabrication of the cell. The following **Table 5.1** provides a summary of the required material for experiments.

Table 5.1. The experimental information.

Name	Brand	Usage
Potassium permanganate ($KMnO_4$)	AR, 99%, Aladdin	Raw materials for synthesis of active material
Manganese sulfate monohydrate ($MnSO_4$)	AR, 99%, Aladdin	Raw materials for synthesis of active material
Ammonium chloride ((NH_4Cl)	ACS, 99.5%, Aladdin	Raw materials to reduce electrode
Sodium carbonate (Na_2CO_3)	ACS, 99.5%, Aladdin	Raw materials of electrolyte
Sodium bicarbonate ($NaHCO_3$)	HPLC, ≥ 99.8%, Aladdin	Raw materials of electrolyte
Carbon dioxide	≥ 99.8%, Linde HKO Ltd.	Raw materials to generate pH change
Activated carbon	(Nippon Kodoshi Corporation, MPF30AC100)	Raw materials of electrode
Poly-1,1-difluoroethene (PVDF)	Solef 5130, Solvay	Raw materials of electrode
N-Methyl-2-pyrrolidone (NMP)	ACS reagent, ≥ 99.0%, Sigma Aldrich	Raw materials of electrode

Carbon cloth	CeTech W0S1011	Raw materials of electrode
Zn flake	≥ 99.95%, 0.1 mm, KeJing	Raw materials to reduce electrode

Potassium permanganate ($KMnO_4$), manganese sulfate monohydrate ($MnSO_4$, AR, 99%, Aladdin), ammonium chloride (NH_4Cl, ACS, 99.5%, Aladdin), sodium carbonate (Na_2CO_3, ACS, 99.5%, Aladdin), sodium bicarbonate ($NaHCO_3$, HPLC, ≥ 99.8%, Aladdin), carbon dioxide (CO_2, ≥ 99.8%, Linde HKO Ltd.), activated carbon, poly-1,1-difluoroethene (PVDF, Solef 5130, Solvay), N-Methyl-2-pyrrolidone (NMP, ACS reagent, ≥ 99.0%, Sigma Aldrich) were used without further purification. Carbon cloth was washed with 1 M H_2SO_4 and DI water, followed by a 4-hour 500 ℃ treatment to strengthen hydrophilicity. Zn flake was washed with 70% alcohol and DI water and dried under N_2 stream. Deionized water (18.2 MΩ) was used throughout the experiments.

5.2.2 Synthesis of the MnO_2 Powder

The brown MnO_2 powder is synthesized by coprecipitation reaction: $2KMnO_4 + 3MnSO_4 \rightarrow 5MnO_2 \downarrow + 3K_2SO_4 + H_2SO_4$. Equal volumes of 0.1 M $KMnO_4$ and 0.15 M $MnSO_4$ were simultaneously added dropwise into 50 mL DI water. The resulting dark brown powder was rinsed with DI water several times and dried at room temperature.

5.2.3 Preparation of the Electrodes

For pure MnO_2 electrodes, 3.5 g as-synthesized MnO_2 powder is mixed with 1 g active carbon and 0.5 g PVDF and dissolved in NMP. The obtained slurry was coated on carbon cloth and dried at 65℃ for 24 h. MnOOH/MnO_2 electrodes were prepared by cathodic reduction of MnO_2 electrodes, with Zn flake as an anode in 1 M NH_4Cl electrolyte. The reduction current was set at 0.47 mA cm^{-2}. Electrodes are prepared by drying the mixture of homemade manganese dioxide powder, binder, and conductive agent on carbon cloth. The electrochemical reduction method was then used to ensure the electrodes have the same redox state ratio on both sides. The essence of this is to make sure that there are enough reactants on both sides of the electrodes from the outset of the electrochemical reaction.

5.2.4 Fabrication of the Cell

Two 10 cm silicone tubes (ϕ 1.5×0.25 mm) were sealed in PMMA frame with two corresponding 2 mm air vents. The electrodes and anion exchange membrane are separated by two silicone sheets. One-third of the cell is left empty to prevent overflow of the 0.5 M Na_2CO_3 electrolyte. **Figure 5.2** shows the structure and photo of the cell used in the experiments.

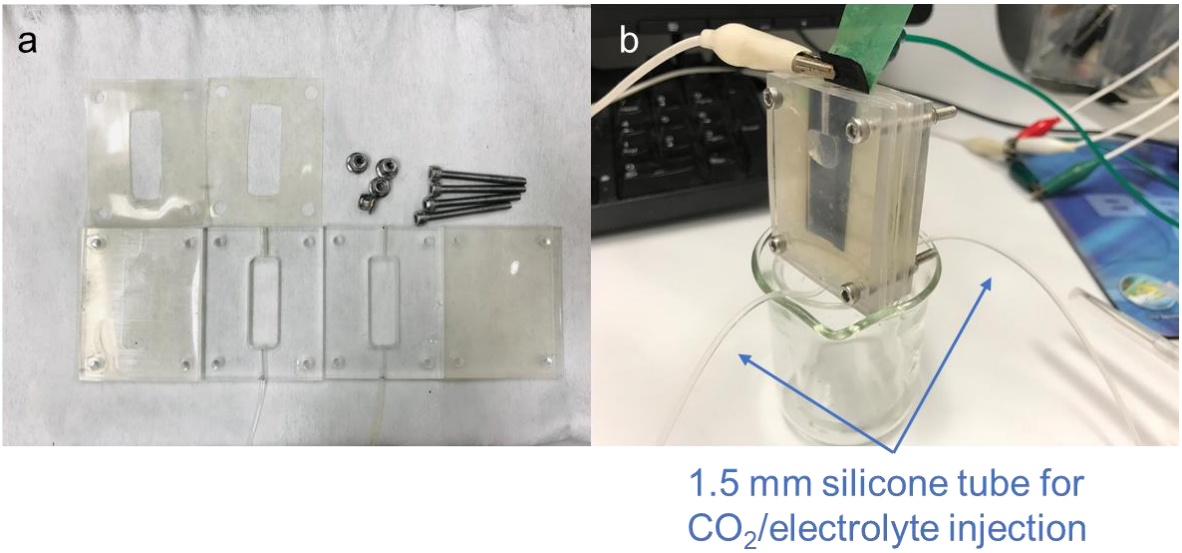

Figure 5.2. Fabrication of the cell. **a)** The components of the cell. **b)** The complete cell after fabrication. Two 10 cm silicone tubes were sealed in PMMA frame with two corresponding 1.5 mm air vents. The electrodes and anion exchange membrane are separated by two silicone sheets. One-third of the cell is left empty to prevent overflow of the 0.5 M Na_2CO_3 electrolyte.

5.2.5 Flow Rate

Typically, 60 mL CO_2 was released from compressed gas cylinders and stored in a sealed syringe. The flow rate is then controlled by adjusting the feed rate and diameter of the syringe using a precise syringe pumping system (LSP01-2A, Baoding Longer Precision Pump Co., Ltd).

5.2.6 XPS

X-ray photoelectron spectra (XPS) were recorded on Nexsa thermo scientific XPS system. The over-lapped XPS were deconvoluted by automatic peak fitting of local extreme value.

5.3 Requirements of TRCPC

To generate electricity from TRCPC, the electrode potential is established by the pH change of the electrolyte with an increasing amount of CO_2 absorbed and then the system is reversible when heat is utilized. Hence, there are three basic requirements for the proposed system to be technically feasible: (1) the cell potential difference can be built by CO_2 absorption; (2) the electrode redox reactions can be driven by the cell potential; and (3) the electrolyte can be thermally regenerated. **Figure 5.3a** illustrates the design concept of TRCPC. The red curve is the change of $NaHCO_3$ percentage with respect to the cell constitutive CO_2 injection level, where the pH decreases after CO_2 is absorbed until the electrolyte in catholyte reaches its saturated condition. The black curve represents the trend of cell open circuit voltage (OCV) versus pH change between two sides. By heating, $NaHCO_3$ is decomposed to Na_2CO_3 and a decrease in $NaHCO_3$ percentage results in the decrease of OCV.

Figure 5.3b shows that the cell OCV raised rapidly until it reached a peak value of approximately 0.18 V. The OCV can be sustained with a constant CO_2 supply; once the supply was interrupted, the voltage gradually decayed (i.e., about 2 hours) due to the ion diffusion (e.g., HCO_3^-) through the membrane from catholyte to anolyte. The slope and peak value of OCV are mainly determined by the CO_2 flow rate, inlet CO_2 concentration, and absorbent concentration. According to $\Delta pH = pH_{initial} - pH_{equilibrium}$ and $\frac{dpH}{dt}$, both the pH change and the rate of pH change increase with increasing the concentration of Na_2CO_3, benefiting a higher peak OCV, a shorter equilibrium time, and a larger amount of CO_2 absorption. Taking

all these factors into account, the 0.5 M Na_2CO_3 electrolyte and the total amount of 20 mL CO_2 for each cycle with flow rate of 2 mL min^{-1} were chosen as the standard in all experiments if not otherwise stated. As shown in **Figure 5.3c** and **d**, the three-electrode system, using MnO_2/MnOOH electrode, platinum wire, and Ag/AgCl electrode as the working, counter, and reference electrode respectively, was used to measure the relationship between the potential change of MnO_2/MnOOH electrode and the pH value of electrolyte in the various $NaHCO_3$/Na_2CO_3 mixtures. As noted, the electrolytes were prepared by mixing 1 M $NaHCO_3$ and 0.5 M Na_2CO_3 to maintain the overall c(Na^+) in 1 M. As noted, the maximum potential between pure $NaHCO_3$ and Na_2CO_3 is approximately 0.18 V. In the operation, only part of Na_2CO_3 was converted to $NaHCO_3$, but the measured voltage also reached close to 0.18V. Here, the membrane may contribute to the increase in the cell potential. **Figure 5.3d** expresses a good linearity between the potential and pH with a slope of 78.8 mV pH^{-1} in a pH range from 8.4 to 10.5.

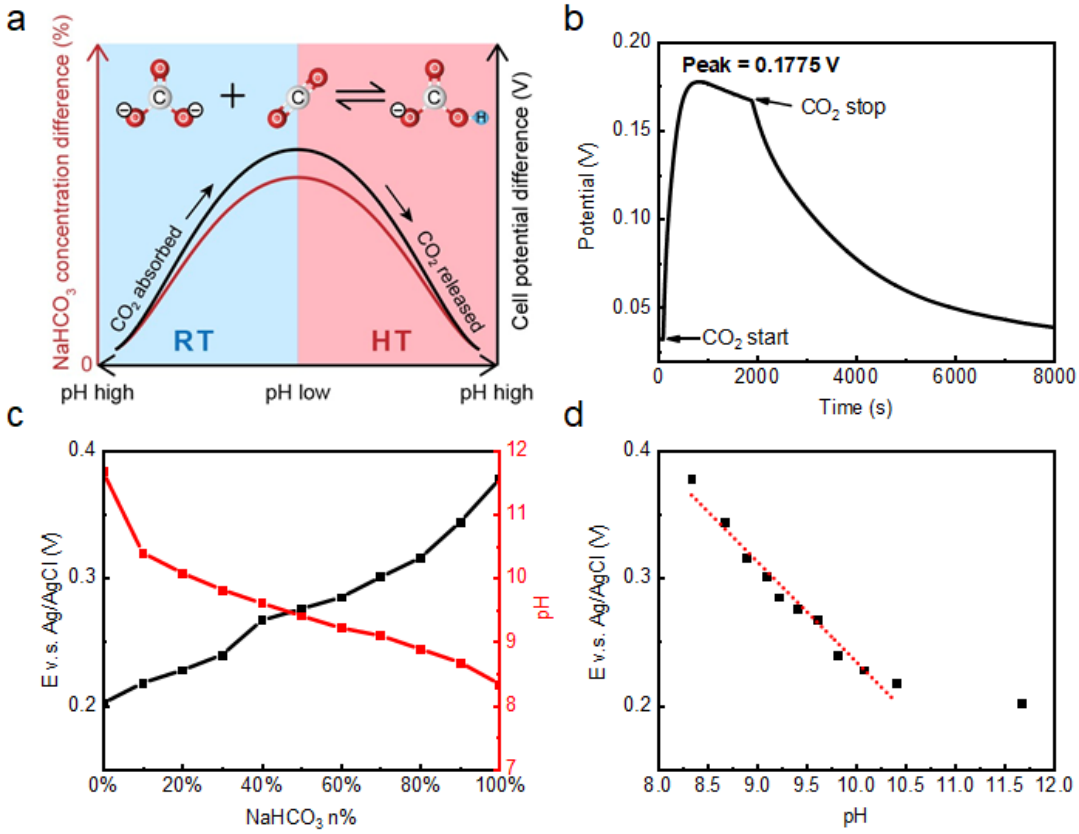

Figure 5.3. The schematic of CO_2-induced voltage. **a)** Systematic diagram of the CO_2 cycle in the cell at hot temperature (HT) and room temperature (RT). **b)** Open circuit potential before, during, and after CO_2 pumping. The flow rate of CO_2 is 2 mL min^{-1}, the overall volume of CO_2 is 60 mL. **c)** MnOOH/MnO_2 electrode potential and pH versus $NaHCO_3$ molar percentage in $NaHCO_3$/Na_2CO_3 solution. The remaining total c(Na^+) is 1 M. **d)** MnOOH/MnO_2 electrode potential versus pH value.

The discharging ability of TRCPC relies on the pseudocapacitance behavior of the MnOOH/MnO_2 electrodes. In **Figure 5.4a**, the cyclic voltammetry curve of MnOOH/MnO_2 electrode (50%/50%, molar fraction) in 0.5 M Na_2CO_3 electrolyte indicates a capacitance of 26.24 F g^{-1}. The synthesized MnO_2 particles were approximately 500 nm as illustrated in

Figure 5.4b. As shown in **Figure 5.4c-e**, the X-ray photoelectron spectroscopy (XPS) spectrum provided evidence that MnO_2 and MnOOH were co-existed. **Figure 5.4e** demonstrates the transformation from MnO_2 to MnOOH during the controlled discharging process.

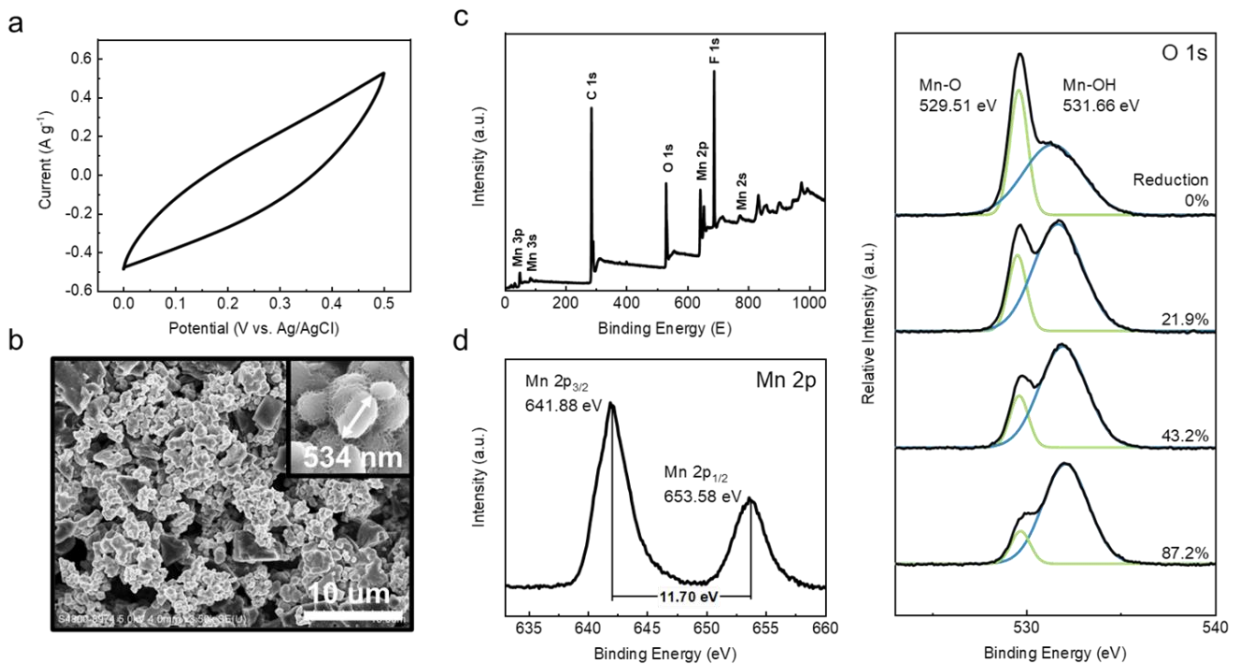

Figure 5.4. a) CV curves of $MnOOH/MnO_2$ electrode in 0.5 M Na_2CO_3 electrolyte at a scanning rate of 50 mV s^{-1}. The $c(Na^+)$ is maintained at 1 M. **b)** SEM image of MnO_2 particles on the electrode. **c)** XPS survey spectrum of $MnOOH/MnO_2$ electrode and the narrow XPS spectrum of **d)** Mn 2p, **e)** O 1s corresponding to different reduction states.

5.4 Performances of TRCPC

After investigating the CO_2-induced voltage generation and electrode discharging capability, the charge-discharge cycles were conducted to study the system performances. In **Figure 5.5a**, the peak power density of TRCPC was calculated to be 0.578 W m^{-2}. **Figure 5.5b** shows the constant current discharging performance of our standard 20 mL CO_2 system as compared with the 60 mL CO_2 system, where the discharging times were 360 s and 720.4 s under 1 mA discharging current, respectively. Although the initial potential of the 60 mL CO_2 system (0.1601 V) was slightly higher than that of the 20 mL CO_2 system (0.1404 V), there was a quick potential drop at the beginning and both systems had a similar level of average discharging potential (0.0425 V and 0.0428 V). The overall energy densities were calculated to be 153.05 J m^{-2} and 70.614 J m^{-2} for 60 mL and 20 mL, respectively. Unifying to 1 mole CO_2, energy density values of 15.871 Wh m^{-2} mol^{-1} (60 mL) and 21.972 Wh m^{-2} mol^{-1} (20 mL) were obtained. In principle, under the same discharging conditions, the discharging time of a 60 mL CO_2 system should be 3 times of 20 mL CO_2 system; however, a 60 mL CO_2 system only showed 2.17 times. This difference was mainly caused by two reasons. First, in a limited electrolyte volume (1.6 mL), the CO_2 absorption rate decreased with increasing the proportion of $NaHCO_3$, leading to a non-linear relationship between CO_2 absorption capability and CO_2 supply. In the late absorption period of the 60 mL system, the same amount of CO_2 supply provided a relatively short discharging time. Second, more ions (e.g., HCO_3^-) would diffuse across the membrane from catholyte to anolyte during the longer operation time of the 60 mL

CO_2 system, resulting in a larger potential drop. Therefore, the energy density of the 60 mL CO_2 system was less than that of the 20 mL CO_2 system.

Before conducting cycling experiments, the cut-off point was determined to be the full conversion from Na_2CO_3 to $NaHCO_3$ in the electrolyte. Here, a control system with pure 1M $NaHCO_3$ in both anolyte and catholyte was used, where CO_2 was supplied to the catholyte. This control system represented the saturated condition[12] so that its potential plateau (50 mV) indicated the cut-off point as Na_2CO_3 was fully converted to $NaHCO_3$ in the TRCPC, as seen in the dash lines in **Figure 5.5c**. Once the voltage is lower than the cut-off point, it is time to regenerate the electrolyte by heat. Under this circumstance, the overall 30 cycles were performed from the initial state to the cut-off point with the final built-in potential of approximately 55 mV. The total energy of these 30 cycles was counted by integrating the discharging energy of every cycle when discharge time decreases from 322.2 s of the first cycle to 48.78 s of the last cycle; the total energy produced is computed to be 0.06252 J, corresponding to the consumption of 0.02679 mole CO_2 and the generation of 0.0016 mole $NaHCO_3$. The build-in voltages decreased because the CO_2 absorption capability gradually declined as the solution became a mixture of Na_2CO_3 and $NaHCO_3$. It is important to note that the potential does not start from 0 V except the first charge-discharge cycle due to the membrane potential being built by the concentration difference between anolyte and catholyte. It takes a long time for ions to completely diffuse across the membrane to remove these residual charges. After several charging-discharging cycles, the cathode was in the reduced state with

more MnOOH while the anode was in the oxidized state with more MnO_2. It is worthy to note that the two electrodes and membrane can be swapped and flipped over to discharge current in an opposite direction and adjust the proportion of MnOOH/MnO_2 as shown in **Figure 5.5d**. This process can be reproduced, making the TRCPC a sustainable system.

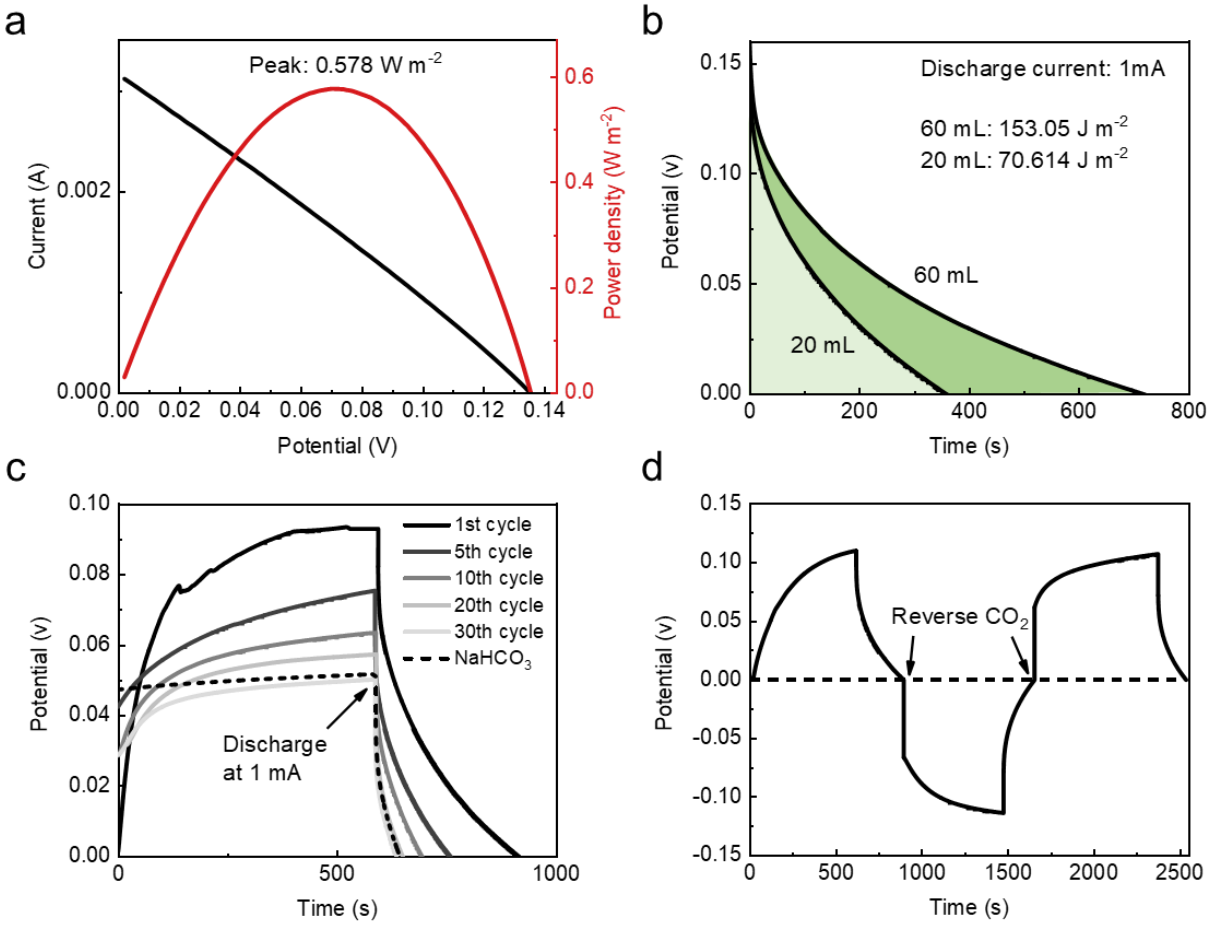

Figure 5.5. a) Current-potential curve and corresponding power density output with 2 mL min^{-1} and 20 mL CO_2 pumping. **b)** Potential-time curve during discharging with a constant current of 1 mA after establishing the potential of 20 mL and 60 mL CO_2 respectively. **c)** 30 cycles of CO_2 charging and 1 mA discharging (2 mL min^{-1}, 20 mL) whose potential changes are compared with the control group of pure $NaHCO_3$. **d)** the discharging performance of the

reversed electrode. The electrode was reversed after the previous charge-discharge cycle.

After the system reaches saturated state, the electrolyte can be thermally regenerated by using low-grade waste heat. The absorbed CO_2 will be released and then stored, allowing TRCPC for the next operation. To efficiently utilize the waste heat, a lower regenerating temperature and a larger built-in potential are expected at the same time. The pH changes of the electrolytes were monitored under different temperatures to estimate the proportion of $NaHCO_3$ and Na_2CO_3. The percentage of $NaHCO_3/Na_2CO_3$ conversion shown in **Figure 5.6a** was more than 80% at 90℃ and less than 10% at 70℃. Basically, a higher temperature accelerated the conversion of $NaHCO_3/Na_2CO_3$ and a lower temperature would take a longer time for the conversion. **Figure 5.6b** further demonstrates the release of CO_2 from the electrolyte at the temperature of 90℃. It can be estimated that the system needs at least 0.4872 kJ of heat for 1.6 mL electrolyte regeneration.

The proof-of-concept implementation of one cell worked under 10 Ω load was shown in **Figure 5.6c**. After building up the OCV of 0.11 V, the switch was turned on and then the current was recorded by the ammeter under continuous supply of gas. As seen, the discharging potential was stabilized at 0.047 V with a stable current output of 0.32 mA. Once the CO_2 supply was interrupted, the potential and current quickly decreased within 1000 s. It is suggested that a continuous CO_2 supply can maintain the potential difference and will extend the discharge time. The TRCPC shows a great potential to scale up in the industry, particularly in a thermal power plant. According to our current design, 14.7 W h electricity

can be produced based on 1 ton CO_2 in a single TRCPC cycle. However, this result was obtained from the single-cell while a single cell was not available to absorb all the CO_2. A single cell of TRCPC utilized a small part of CO_2 for power generation. In the practical application, it is feasible to construct a cascade system with integrated cells, making full use of CO_2. If all the CO_2 can be fully used, 493 W h electricity will be generated from 1 ton CO_2 per cycle. Assuming CO_2 emission of 20 million tons per year from one power plant,[118] 9.8 GW h electricity is able to be produced by one TRCPC cycle. Although this result sounds very exciting, there are still some unresolved issues that need to be addressed before it can be practically implemented. Two significant issues include the stability of the electrode and the inevitable ion cross-over through the membrane during discharge. The first issue pertains to the stability of the electrode. Specifically, the manganese-based electrode used in the TREC system is not stable in an alkaline environment, leading to a shorter lifespan. To address this issue, further research is needed to identify alternative electrode materials that are more stable and can support high power densities without degrading over time. The second issue relates to the inevitable ion cross-over through the membrane during discharge. This phenomenon can lead to the loss of pH differences, directly resulting in the inability to maintain the thermodynamic driving force required for efficient heat-to-electricity conversion. To overcome this issue, various approaches could be explored, such as improving the selectivity of the membrane, developing alternative electrolytes that minimize ion cross-over, or implementing advanced control strategies to mitigate the effects of ion

cross-over.

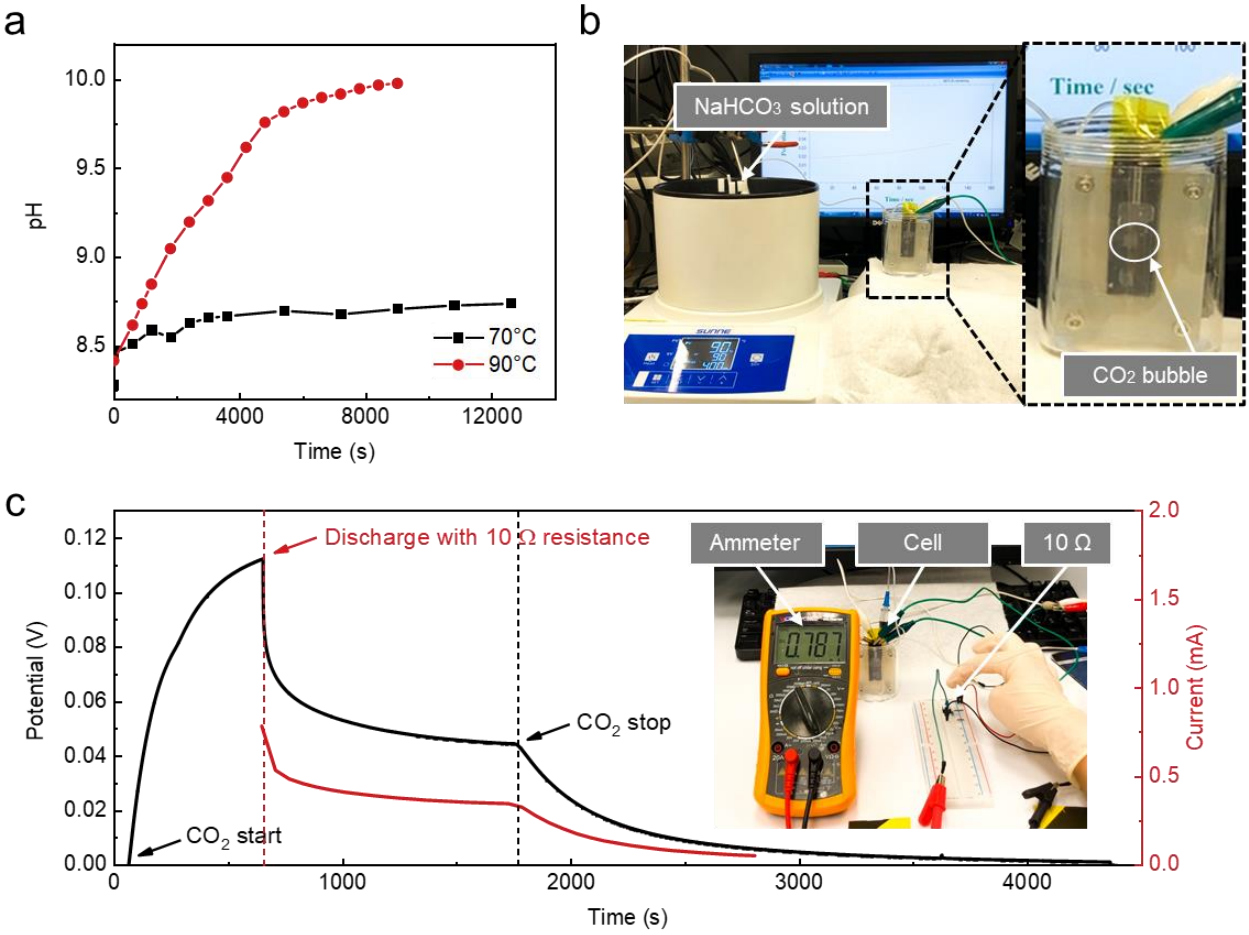

Figure 5.6. Heat regenerative electrolyte. **a)** The pH changes of the 1 M $NaHCO_3$ towards time under the 70℃ and 90℃ environmental temperature. **b)** The demonstration of decomposition of 1 M $NaHCO_3$ solution which is sealed in a glass container under the 90℃ environmental temperature. The continuous bubbles in the cell are decomposed CO_2 gas. **c)** The discharging performance with 10 Ω resistance.

5.5 Theoretical Analysis

5.5.1 Effect of Na^+

MnO_2 is a material with possible electrochemical insertion/extraction of H^+ and alkali metal ions. Due to the effect of ion size, hydrogen ions are generally more reactive than alkali metal ions in the low potential range. In this work, the concentration of Na^+ is higher than H^+ in $NaHCO_3$ and Na_2CO_3 solutions; thus, the possibility of Na^+ intercalation should be verified.

First, two groups of controlled experiments were studied by using electrochemical potential change. The first group has undergone changes [H^+] while [Na^+] remained unchanged. The second group experienced changes in [Na^+] while [H^+] remained unchanged. Either H^+ or Na^+, the reaction on the electrode can be denoted as below:

$$MnO_2 + A^+ + e^- \leftrightarrow MnOOA \tag{54}$$

where A^+ represents H^+ or Na^+. Thus, the theoretical relation of electrode potential φ and active ion concentration $[A^+]$ in solution can be explained as:

$$\varphi = \varphi_0 + \frac{RT}{nF} ln \frac{[MnO_2][A^+]}{[MnOOA]} = \varphi_0 + \frac{2.303RT}{nF} lg[A^+] = \varphi_0 + 0.0591\, lg[A^+]. \tag{55}$$

Therefore, the theoretical slop is determined to be:

$$\frac{d\varphi}{d(-lg[A^+])_{theory}} = -0.0591. \tag{56}$$

Figure 5.6a and **b** shows the experimental results of MnOOH/MnO_2 electrode potential in Na_2CO_3-$NaHCO_3$ solution with consistent [Na^+], and in NaCl and Na_2SO_4 solution with consistent [H^+].

For Na_2CO_3-$NaHCO_3$ solution,

$$\frac{d\varphi}{d(-lg[A^+])_{theory}} = -0.05437 \quad (57)$$

For NaCl solution,

$$\frac{d\varphi}{d(-lg[A^+])_{theory}} = 6.0010 \times 10^{-4} \quad (58)$$

From the slopes from **Figure 5.7a** and **b**, it can be seen that $\frac{d\varphi}{d(-lg[H^+])} \approx \frac{d\varphi}{d(-lg[A^+])_{theory}} \gg \frac{d\varphi}{d\,(-lg[Na^+])}$. Accordingly, we can see that the dominate active ion in the electrolyte should be H^+ rather than Na^+.

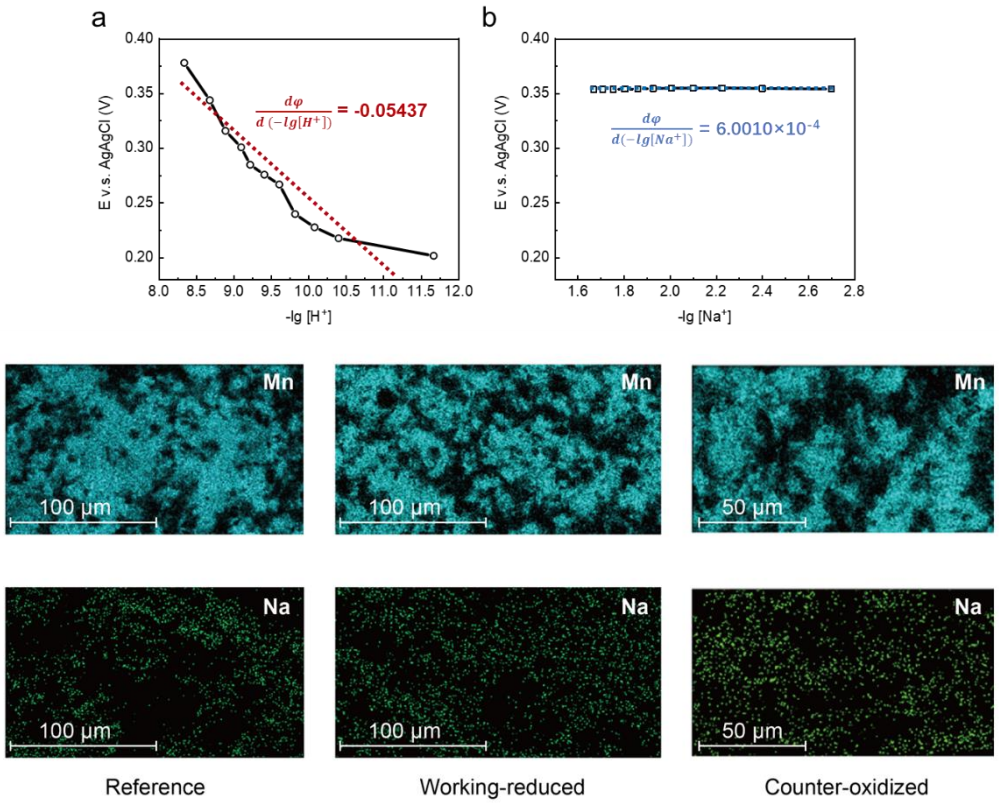

Figure 5.7. Potential change of $MnOOH/MnO_2$ electrode in **a)** Na_2CO_3-$NaHCO_3$ solution with consistent c(Na^+) = 1 M, **b)** in NaCl solution with consistent c(H^+) ≈ $10^{-6.06}$. Energy dispersive spectroscopy (EDS) elemental mapping images showing the distribution of Mn and Na on, **c)** and **d)**, reference electrode immersed in 1 M $NaHCO_3$ solution. **e)** and **f)**, working electrode in TRCPC. **g)** and **h)**, counter electrode in TRCPC.

Moreover, an EDS analysis was conducted on the working electrode (reduced) and counter electrode (oxidized) in TRCPC. Another MnOOH/MnO_2 electrode was immersed in 1 M $NaHCO_3$ solution for the same time as a reference. **Figure 5.7c** to **h** shows that the distribution of Mn and Na has little difference among the reference electrode, working electrode, and counter electrode. The quantitative EDS analysis shows a very small Na percentage on both the working electrode (0%→1.74%) and counter electrode (0%→0.98%), which are in the same range of Na^+ absorption on the reference electrode (0%→0.48%). The sightly difference between the working electrode and counter electrode may come from the ion exchange between H^+ and Na^+.[119] The EDS results further evidenced that Na^+ is not the dominant reactive ion in TRCPC.

5.5.2 Effect of Ion Concentration

In the following section, we will calculate the change in OCV resulting from the pH changes in the electrolytes during discharging. Our calculations will be based on the ionization and hydrolysis of carbonate and bicarbonate ions, as well as water. We will determine the proportion of carbonate and bicarbonate ions in the electrolyte at different pH values and correspond these values to the number of transferred electrons. Considering the balance of ionization and hydrolysis in electrolyte of 1 M Na^+, the charge balance, ionization and hydrolysis equations are given as follows.

$$H_2CO_3 \leftrightharpoons H^+ + HCO_3^- \quad (59)$$

$$HCO_3^- \leftrightharpoons H^+ + CO_3^{2-} \quad (60)$$

$$H_2O \leftrightharpoons H^+ + OH^- \tag{61}$$

$$K_{A1} = \frac{[H^+][HCO_3^-]}{[H_2CO_3]} = 4.3 \times 10^{-7} \tag{62}$$

$$K_{A2} = \frac{[H^+][CO_3^{2-}]}{[HCO_3^-]} = 5.61 \times 10^{-11} \tag{63}$$

$$K_w = [H^+][OH^-] = 10^{-14} \tag{64}$$

$$[H^+]+[Na^+]=[HCO_3^-]+[OH^-]+2[CO_3^{2-}] \tag{65}$$

So that the $[H^+]$ can be expressed in terms of $[HCO_3^-]$ and $[CO_3^{2-}]$, the equations are shown below.

$$[H^+]^2+([Na^+]-[HCO_3^-])[H^+] - (K_w + 2K_{A2}[HCO_3^-]) = 0 \tag{66}$$

$$\begin{cases} [H^+]+[Na^+] = \frac{[H^+][CO_3^{2-}]}{K_{A2}} + 2[CO_3^{2-}] + \frac{K_w}{[H^+]} \\ pH = -\lg[H^+] \end{cases} \tag{67}$$

For 0.5 M Na_2CO_3 solution, it can be easily seen from the ratio of $\frac{K_{a1}}{K_{a2}} \approx 10000$, so the existing of H_2CO_3 can be neglected.

For 1 M $NaHCO_3$ solution, the calculated pH value (8.3098) is very close to the experimental pH value of simulated CO_2 absorbed solution (8.30). At this point, the concentration ratio of H_2CO_3 to HCO_3^- is 1.14%.

5.5.3 Calculation of Efficiency in TRCPC

To further explain the mechanism behind, a theoretical analysis of TRCPC was conducted. From **Figure 5.8**, the relation of the output energy and input energy can be described below.

$$\eta = \frac{W_{output}}{E_{input}} = \frac{W_e}{W_p+Q_{in}} \tag{68}$$

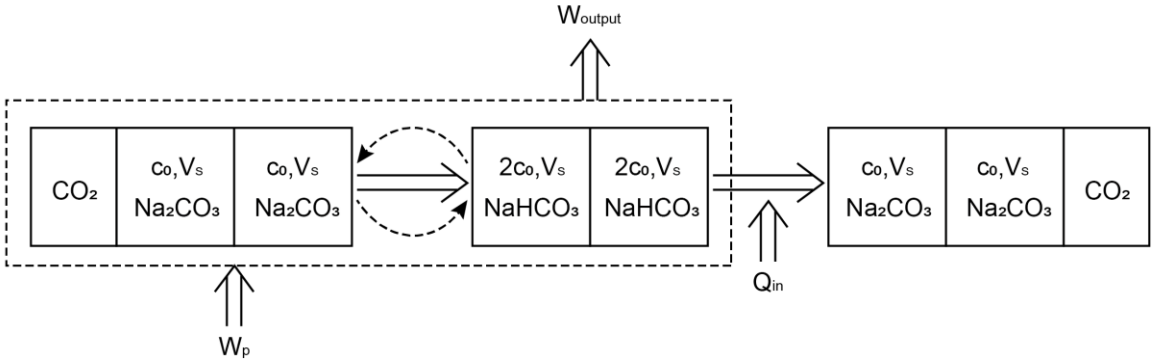

Figure 5.8. The energy balance diagram of TRCPC.

Output energy

a) Experimental output energy

$$W_{output,exp} = W_{e,exp} = \sum_i \overline{U}_i I_i t_i \tag{69}$$

$\overline{U}_i$ is the average discharging voltage, I_i is the discharging current, t_i is the total discharging time for cycle *i*. From **Figure 5.9 and Table 5.2**, a single cell containing 1.6 mL electrolyte has a total energy output of 0.05646 J.

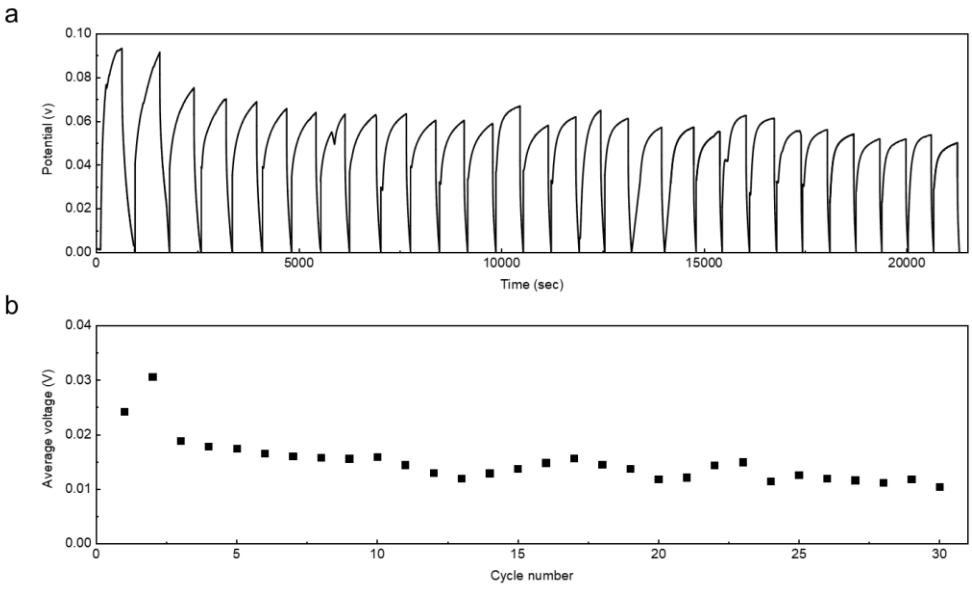

Figure 5.9. Cycle performance of one complete electrolyte conversion. **a)** Charge-discharge

curve of 30 cycles. **b)** The average discharge voltage for each cycle.

Table 5.2. The average discharging voltage $\overline{U}$ and time t in the cycling experiments. The inlet of CO_2 is 20 mL per cycle. The discharging current I is 1 mA.

Average cell voltage $\overline{U}$ (V)	Discharge time t (s)	$W = \overline{U}It$ (J)
0.02423	322.2	0.007808
0.03065	239.6	0.007343
0.02184	265.9	0.005807
0.01882	173.2	0.003259
0.01785	151.4	0.002702
0.01746	138.8	0.002423
0.01659	121.9	0.002022
0.01606	112.9	0.001813
0.01577	111.4	0.001756
0.01559	109.3	0.001704
0.01588	106.1	0.001685
0.01445	92.35	0.001334
0.01296	86.14	0.001116
0.01198	78.03	0.000935
0.01292	78.43	0.001013
0.01371	73.6	0.001009
0.01483	84.91	0.001259
0.01564	99.11	0.00155
0.01449	82.86	0.0012
0.01376	75.07	0.001033
0.01186	61.33	0.000727
0.01214	58.96	0.000716
0.0144	85.1	0.001225
0.01495	52.16	0.00078
0.01142	34.29	0.000392
0.01254	63.92	0.000802
0.01194	56.65	0.000676
0.01161	48.74	0.000566
0.01119	52.91	0.000592
0.0118	59.86	0.000707
0.01039	48.78	0.000507

b) Theoretical output energy

For n mol electron transferred in the cell, from Nernst equation we have:

$$E_n = (\varphi_{catholyte} - \varphi_{anolyte})_n = 0.0591\Delta pH_n \quad (70)$$

$$W_{e,ideal} = \int dW_e = \int FE_n dn = \int 0.0591F\Delta pH_n dn \quad (71)$$

where E_n and ΔpH_n is the cell voltage and pH difference between anolyte and catholyte, corresponding to condition of n mole electron have been transferred.

Thus, to calculate the voltage change during the discharging process, the relationship between ΔpH_n and n should be firstly calculated. In the ideal case, one transferred electron can correspond with the increase in two HCO_3^- molecules and a decrease in one CO_3^{2-} molecule in the anolyte. Integrated with the relationship between ion concentration and pH, the theoretical ΔpH_n and E_n during electron transfer corresponding to 1 L catholyte/anolyte is shown in **Figure 5.10**. When the cell is fully discharged, both ΔpH_n and E_n drops to 0, the $W_{e,ideal}$ is 4.2888 kJ corresponding to 1 L catholyte/anolyte. In a single cell, $W_{output,ideal} = W_{e,ideal} = 3.431J$.

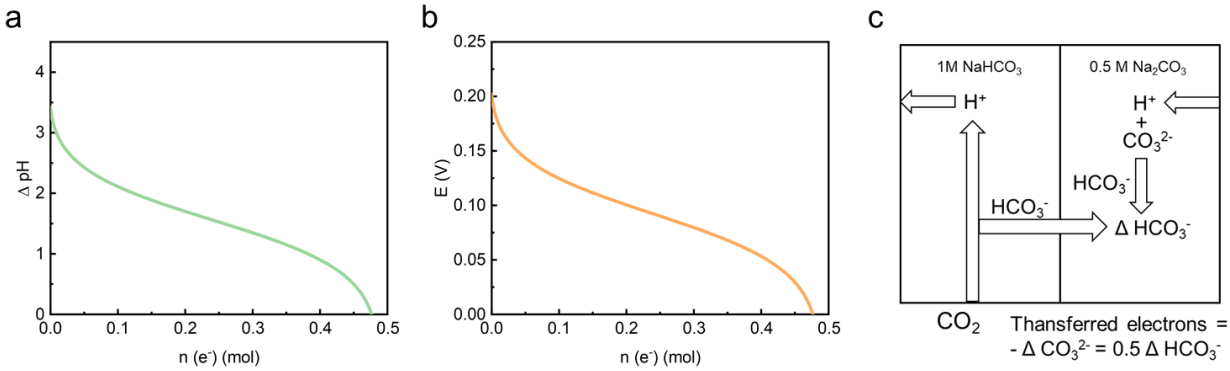

Figure 5.10. The theoretical calculated results of **a)** ΔpH_n and **b)** E_n during electron transfer,

corresponding to 1 L catholyte/anolyte. **c)** Ion movements during discharge.

Input energy

$$E_{input} = W_p + Q_{in} \tag{72}$$

The input energy comes from two parts, pump work for CO_2 inlet (W_p) and thermal energy (Q_{in}) for $NaHCO_3$(aq) decomposition.

a) Pump work

The pump work can be easily calculated with CO_2 mass and flow rate. In a single cell and 2 mL min^{-1} flow rate, the pump work is

$$W_p = \frac{1}{2} m_{CO2} v^2 = 2.5335 \times 10^{-7}\ J. \tag{73}$$

b) Input heat

The input heat can be divided into two parts. The first part Q_1 is the heat required for the decomposition reaction.

$$\begin{cases} NaHCO_3(s) \rightarrow \frac{1}{2} Na_2CO_3(s) + \frac{1}{2}\ CO_2(g) + \frac{1}{2} H_2O(g),\ \Delta H_1^\theta = +63.977\ kJ\ mol^{-1} \\ Na_2CO_3(s) \rightarrow 2Na^+(aq) + CO_3^{2-}(aq),\ \Delta H_2^\theta = -28.1\ kJ\ mol^{-1} \\ NaHCO_3(s) \rightarrow Na^+(aq) + HCO_3^-(aq),\ \Delta H_3^\theta = +18.61\ kJ\ mol^{-1} \\ HCO_3^-(aq) \rightarrow \frac{1}{2} CO_3^{2-} + \frac{1}{2}\ CO_2(g) + \frac{1}{2} H_2O(l),\ \Delta H_4^\theta = ? \\ H_2O(g) \rightarrow H_2O(l),\ \Delta H_5^\theta = -40.8\ kJ\ mol^{-1} \end{cases} \tag{74}$$

Thus, the enthalpy can be calculated as below.

$$\Delta H_4^\theta = \Delta H_1^\theta + \frac{1}{2}\Delta H_2^\theta - \Delta H_3^\theta + \frac{1}{2}\Delta H_5^\theta = 10.917\ kJ\ mol^{-1}. \tag{75}$$

For a single cell, Q_1 is

$$Q_1 = 0.00873\ kJ. \tag{76}$$

The second part Q_2 is the heat required to heat up the electrolyte from the working temperature (T_1=25°C) to the regeneration temperature (T_2=90°C). The specific heat capacity of the solution is taken as 3.979 J K^{-1} g^{-1} which is similar to other sodium-based solutions.[120,121]

For a single cell, Q_2 is

$$Q_2 = m_{electrolyte} C_p (T_1 - T_2) \approx 0.2243\ kJ. \tag{77}$$

Thus, the input heat and input energy can be calculated as:

$$Q_{in} = Q_1 + Q_2 = 0.23303\ kJ \tag{78}$$

$$E_{input} = W_p + Q_{in} = 1.017 \times 10^{-6}\ J + 0.23303\ kJ \approx 0.23303\ kJ. \tag{79}$$

We can see that W_p contributes little to the total energy needed in the ideal system which can be eliminated.

$$E_{input,ideal} = W_p + Q_{in} \approx Q_{in} \tag{80}$$

Comparison of efficiency

$$\eta_{exp} = \frac{W_{output,exp}}{E_{input}} = \frac{W_{e,exp}}{W_p + Q_{in}} = 0.024\% \tag{81}$$

$$\eta_{ideal} = \frac{W_{output,ideal}}{E_{input}} = \frac{W_{e,ideal}}{W_p + Q_{in}} = 1.47\% \tag{82}$$

Comparing the ideal efficiency with Carnot efficiency (17.899%, 25-90°C), the efficiency of our system should be lower than those of current heat engines at a low-temperature regime due to inevitable ion cross-over problem through membrane. However, the current system has plenty of room for optimization. Corresponding to the analysis, here are a number of methods to further improve the efficiency of the proposed new system.

First and foremost, how to efficiently generate energy from $W_{e,ideal}$ is the key problem of TRCPC, which requires further investigation in an electrochemical system with high efficiency

for chemical energy to electricity conversion. At the same time, exploring the reversible absorption process with a wider pH window to enlarge the ΔG_{pH} is also a practical method for cycling operation.

Secondly, increasing the speed of CO_2 absorption. Possible approaches include reducing the flow rate and exploring the absorbents that are easier to absorb the gas to avoid a CO_2 waste.

Thirdly, decreasing the heat required for regeneration. Approaches include developing the water-based electrolyte into an organic electrolyte or utilizing solid materials to store CO_2 because of their lower heat capacity.

5.6 Conclusions

This work demonstrated the design principle and a proof-of-concept device of TRCPC. There is still plenty of room for system optimization based on our theoretical model. For example, tuning the electrode helps to enlarge the capacity and make the discharge time longer, improving the electrolyte benefits the built-in potential and CO_2 consumption, modifying the membrane assists to find the best balance between the diffusion and the concentration difference. In addition, engineering optimizations in the flow rate, pipe diameter and so on are equally important. There could be other underlying improvements such as altering the Na_2CO_3 absorbance into amino.

CHAPTER 6 PH-Sensitive Thermally Regenerative Cell (pH-TRC) with Circulating Hydrogen

6.1 Introduction

Numerous approaches including TREC have been recently proposed for converting low-grade waste heat into electricity. For instance, our previous work on TRCPC demonstrated a new concept by using thermally regenerative pH-gradient and pH-sensitive electrodes for heat-to-electricity conversion. But the power density and discharging time are unsatisfactory among these technologies. That is because previous works including TREC and TRCPC focus on the electrode-involved electrochemical reactions (such as intercalation and deintercalation of alkali metal ions, and metal complexation reaction). The consumption of active materials heavily restricts the lifetime of the electrodes. Therefore, most of the research relative to TREC and TRCPC remains in the stage of experimental verification, and far too little attention has been paid to longer the discharging time with good power for demonstrable use.

Therefore, pH-sensitive thermally regenerative cells (pH-TRCs) are designed. **Figure 6.1a** shows the mechanism of pH-TRCs to convert heat to electricity. OCV (black line) represents Gibbs free energy difference (ΔG, blue line) between the initial state (before discharging) and final state (after discharging) and can be expressed as $OCV=-\Delta G/nF$, where n is the electrons transferred from the electrochemical reaction, F is the Faraday constant. Capable of discharging, the output electric work can be evaluated to be ideally equal to ΔG. During discharging, the

OCV gradually reduces to zero, with a simultaneous decrease in ΔG. Once ΔG is fully exploited during discharging, it will then be regenerated into the initial state in a following thermal regeneration step, corresponding to increases in energy and OCV.

In approaching this aforementioned issue of loss of electrode active material, platinum-H_2/H^+ catalytic electrodes were designed to replace the consumable electrodes and then applied in a proposed pH-TRC with circulating hydrogen. By replacing the early consumable electrode with H_2/H^+ catalytic electrode and rationally improving the cell design, an advanced pH-sensitive thermally regenerative cell (pH-TRC) with circulating hydrogen could potentially achieve both endurable discharging and satisfactory power density.

Figure 6.1b and **Figure 6.1c** show the working mechanism of the design. First, the pH-TRC consists of anolyte (0.5 M Na_2CO_3, pH=11.70) and catholyte (1 M $NaHCO_3$, pH=8.30) with different pH values, allowing an initial pH-induced potential built between the symmetric platinum-H_2/H^+ catalytic anode and cathode. To be noticed, $Na_2CO_3/NaHCO_3$ electrolytes were selected because of their great adaptability in combination with carbon capture and storage (CCS) technologies, giving potential to a cost-effective and scalable system that utilizes wastes (CO_2 and low-grade heat) to produce electricity without external energy supply.[128,129] Next, when the anode and cathode experience reversed proton-related reactions on platinum-H_2/H^+ catalytic electrodes respectively, anolyte and catholyte are neutralized accordingly and this discharging process is ended with an equal pH value of anolyte and catholyte. It should be noted here that Na^+ dominates the ion transport in electrolytes due to the relatively low concentration of H^+. Also, despite there is no Na^+ concentration gradient between anolyte and

catholyte, Na^+ is still able to cross through a CEM by migration under an electric field rather than diffusion. Then, the electrolytes are regenerated by heat to subsequently establish a renewed potential. As a result, a full cycle of pH-TRC is achieved by resetting the pH values of electrolytes as depicted in **Figure 6.1b**. This cycle briefly comprises discharging process and regeneration process, individually terminated at saturated and initial state.

The cell structure of pH-TRC with circulating hydrogen is demonstrated in **Figure 6.1c**. Symmetric platinum-H_2/H^+ catalytic electrodes are initially immersed into anolyte of 0.5 M Na_2CO_3 and catholyte of 1 M $NaHCO_3$ separately (**Figure 6.1a**). The hydrogen gas flows via gas channel meanwhile electrolytes flow through flow channel, where the two channels are sealed by silicone sheets and separated by catalytic electrodes. Reactions occur at the surface of platinum-H_2/H^+ catalytic electrode thereby producing electrons, which are conducted to graphite electrode holder, and ultimately to copper current collector for external circuit power supply.

In this study, power density, discharging time and efficiency of pH-TRC were carefully investigated by both experimental results and theoretical computations. It is shown here that the pH-TRC demonstrates an incredibly long discharging time with a satisfactory power density.

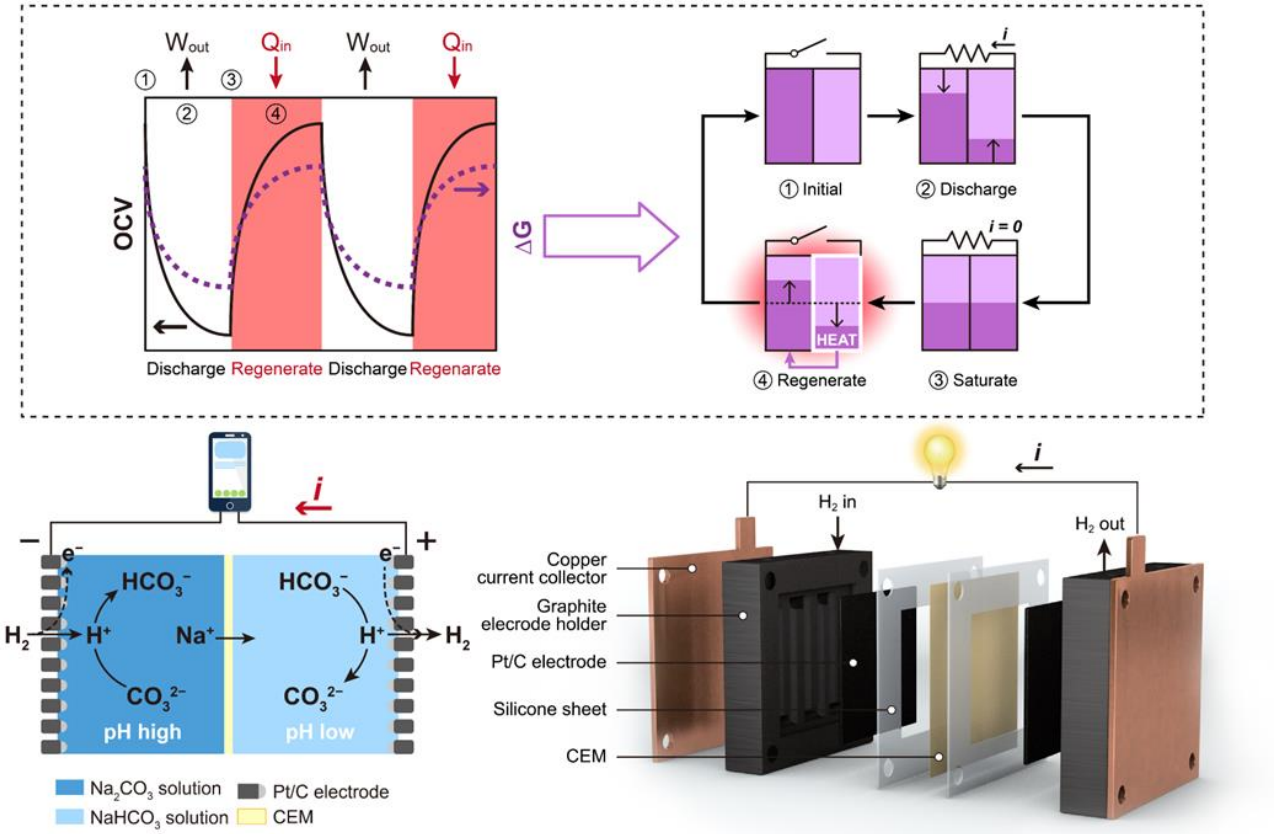

Figure 6.1. Working mechanism of pH-TRC to convert heat into electricity. **a)** Schematic of typical TRC; **b)** Schematic of pH-TRC; **c)** Single cell structure of pH-TRC.

6.2 Experimental Section

6.2.1 Experimental Overview

The quick overview of experimental information is summarized in the following **Table 6.1**.

Table 6.1. The experimental information.

Name	Brand	Usage
Pt/C powder	20%, XC-72r Pt/Vulacan, Premetek	Raw materials of catalytic electrode
Sodium carbonate (Na_2CO_3)	ACS, 99.5%, Aladdin	Raw materials of electrolyte
Sodium bicarbonate ($NaHCO_3$)	HPLC, ≥ 99.8%, Aladdin	Raw materials of electrolyte
Nafion solution	5%, D520, Dupont	Raw materials of catalytic electrode
polytetrafluoroethylene solution	60%, D210C, Daikin	Raw materials of catalytic electrode
carbon paper	28BC, Sigracet	Raw materials of electrode base
carbon cloth	1011, CeTech	Raw materials of electrode base

6.2.2 Preparation of Pt/C Electrodes

For the carbon paper electrodes, 20 mg Pt/C powder (20%), 0.053 g Nafion solution (5%), and 0.0044 g PTFE solution (60%), were mixed and dissolved in 1 mL water-isopropanol mixture (1:4). The Pt/C ink was obtained after 30 min sonication and sprayed on a piece of 2 cm × 2 cm carbon paper at 120℃ for several times. For the carbon cloth electrodes, 20 mg Pt/C powder (20%), and 0.0707 g Nafion solution (5%) was mixed and dissolved in 1 mL water-IPA mixture (1:4). After 30 min sonication and ink spraying, the obtained electrodes were heated at 120 ℃ in an oven for 2 hours.

6.2.3 PH-TRC System Configuration and Operation

The construction of a single pH-TRC was carried out by assembling the Pt/C electrodes (2×2 cm), CEM (4×4 cm), two flow channels (4×4×0.1 cm, fluor rubber

sheets), two electrode holders (4×4×1.5 cm, graphite) with two gas channels (2×2×0.15 cm), two current collectors (4×4×0.1 cm, copper), and two end plates (4×4×1 cm, titanium). The Pt/C electrodes were prepared by spraying Pt/C ink to carbon paper (anode) and carbon cloths (cathode) with an even loading mass of 1 mg Pt per cm^2. The electrodes were tightly glued by liquid rubber to the electrode holders to form the whole electrodes. After drying, the electrodes were connected to the current collectors by adhesive-back fluor rubber sheets and thereby connected to the titanium end plates, fixed by bolts and nuts. The electrolytes were prepared to be 1 M $NaHCO_3$ and 0.5 M Na_2CO_3 by using ultrapure water and then pumped into the cell as catholyte and anolyte. The electrodes, flow channels, and membranes increased but remained the other fixing components for series and parallel configurations of multiple cells. Since each adjacent cell was separated by an insulating gasket, cells could be arranged in rows, meeting various discharging modes by changing connections. It is worth mentioning that although the main substances (Na_2CO_3 and $NaHCO_3$) initiating the pH gradient are very cheap (*ca.* 0.014 USD g^{-1} and 0.018 USD g^{-1}, respectively) the major cost of a single pH-TRC device in the experiment comes from the Pt/C electrodes (*ca.* 0.771 USD cm^{-2}) and the graphite/copper/titanium current collector with gas channels (*ca.* 0.215 USD cm^{-2}). **Table 6.2** include the cost of the materials used in our experiments.

Table 6.2. The experimental information.

Material	Price (USD)	Unit	Material used in a single cell	Cost for a single cell (USD)
Sodium carbonate (Na_2CO_3, ACS, 99.5%, Aladdin)	0.014	g^{-1}	0.5M, 50 ml	0.0377
Sodium bicarbonate ($NaHCO_3$, HPLC, ⩾ 99.8%, Aladdin)	0.018	g^{-1}	1M, 50 ml	0.0754
Pt/C powder (20%, XC-72r Pt/Vulacan, Premetek)	109.901	g^{-1}	40 mg	4.3966
Nafion solution (5%, D520, Dupont)	8.701	ml^{-1}	0.1237 g	1.0764
Polytetrafluoroethylene solution (60%, D210C, Daikin)	0.118	g^{-1}	0.0044 g	0.00052
Carbon paper (28BC, Sigracet)	0.088	cm^{-2}	2*2 cm	0.3536
Carbon cloth (1011, CeTech)	0.086	cm^{-2}	2*2 cm	0.3432
CEM	0.044	cm^{-2}	2*2 cm	0.1768
Graphite (1.5 cm)	0.034	cm^{-2}	4*4 cm, x2	1.0816
Copper (0.1 cm)	0.046	cm^{-2}	4*4 cm, x2	1.456
Titanium	0.031	g^{-1}	4*4*1 cm, x2	4.1028
Fluor rubber sheets (0.1 cm)	0.008	cm^{-2}	4*4 cm, x2	0.2457
Total				**13.35 USD**

6.2.4 Characterization

The electrochemical tests were performed on CHI 760E electrochemical workstation (CH Instrument, Shanghai). The SEM images were captured by VEGA3 (Tescan). The gas chromatography curves were recorded on GC9720 (Fuli Instruments).

6.3 OCV Generation

It is crucial to understand the generation of OCV since it implies reactions occurring

on electrodes. With a hydrogen supply to the anode, electricity is derived from reversible pH-driven electrode reactions as expressed below.

Anode: 0.5 M Na_2CO_3

$$H_2 \rightarrow 2H^+ + 2e^- \quad (83)$$

$$2H^+ + 2{CO_3}^{2-} \rightarrow 2{HCO_3}^- \quad (84)$$

Cathode: 1 M $NaHCO_3$

$$2H_2O + 2e^- \rightarrow 2OH^- + H_2 \quad (85)$$

$$2OH^- + 2{HCO_3}^- \rightarrow 2{CO_3}^{2-} + 2H_2O \quad (86)$$

During discharging, the anode and cathode experience the hydrogen oxidation reaction (HOR) and the hydrogen evolution reaction (HER), respectively, the net H_2 consumption is zero. Theoretically, OCV established by a pH difference between the anolyte and the catholyte would gradually decrease from approximately 0.2 V to 0 V when an equal-pH-state is reached (**Figure. 6.2a, b**). Afterward, thermal regeneration of electrolytes can be conducted to initialize the discharging state. It is worth noticing that the number of theoretical electrons transferred through the aforementioned reaction is not 1 M or 0.5 M but much lower. Considering the product and anion migration effect on the pH difference, the transferred electrons are determined to be 0.32 M. Therefore, 1.426 KJ of electricity can be generated corresponding to 1 L anolyte/catholyte.

Corresponding to the aforementioned reactions of the anode and cathode, a theoretical OCV can be determined as below, assuming the standard states for gas and solutions are 1 atm and 1 M. The subscripts of a and c represent anode and cathode, respectively. p is the partial pressures of hydrogen. From the OCV equation, it suggests that OCV value is contributed by differences in both pH and hydrogen partial pressure,

which is clearly illustrated in **Figure. 6.2c**.

$$E_{anode} = E_a{}^0 + \frac{2.301RT}{2F} lg \frac{C_{H^+}^2}{p_{H_2}} \quad (85)$$

$$E_{anode} = E_a{}^0 - 0.059\left(pH_a + lg\, p_{H_2a}^{0.5}\right) \quad (86)$$

$$E_{cathode} = E_c{}^0 - \frac{2.301RT}{2F} lg(C_{H^+}^2 p_{H_2}) \quad (85)$$

$$E_{cathode} = E_c{}^0 + 0.059\left(14 - pH_c - lg\, p_{H_2c}^{0.5}\right) \quad (86)$$

$$E_c{}^0 - E_a{}^0 = 0.829\, V \quad (87)$$

$$OCV = 0.059\left(pH_a - pH_c + lg\, p_{H_2c}^{0.5} - lg\, p_{H_2a}^{0.5}\right) \quad (88)$$

The OCV of the cell stabilized at 0.17 V at the beginning and increased significantly until it rapidly reached a peak voltage of over 1 V within a few seconds once the cell was supplied with hydrogen. This value gradually decreased to 0.2061 V in the end.

The outset and end of voltages suggests that the OCV value is mainly determined by the pH difference since there is only a slight increase of 0.306 V (**Figure. 6.2c**) in the OCV after gas supply on comparison to the OCV of 0.13 V caused by the pH difference at the start (**Figure. 6.2c**). However, it still couldn't explain the peak and slope of OCV. To explore the causes of the peak and slope of OCV, the electrode potentials of anode and cathode were respectively measured in 0.5 M Na_2CO_3 and 1 M $NaHCO_3$ in a proper order. **Figure. 6.2d** and **Figure. 6.2e** depict the OCV changes of anode and cathode corresponding to switching inlet H_2. The values of the anode and cathode OCV both start at a positive value, but end at a negative value after providing H_2, suggesting an additional oxygen reduction reaction (ORR) from the dissolved oxygen, which dominates the OCV at the start. However, with saturation of H_2 in electrolyte, the voltage changes into normal values at -0.7256 V of anode and -0.5206 V of cathode, providing an overall OCV of 0.2 V at the end, which confirms the final

OCV in **Figure. 6.2c**. Besides, the anode (carbon paper) displays a quicker response in comparison to cathode (carbon cloths) from **Figure. 6.2d** and **Figure. 6.2e**. That helps to illustrate an asymmetric peak OCV in **Figure. 6.2c**, where an extremely sharp OCV slope appears before the peak value and slowly fades afterward. The effect of dissolved H_2 on OCV was further investigated by examining the cathode in different electrolyte states. The cathode was immersed in 1 M $NaHCO_3$, 0.5 M Na_2CO_3 and 1 M $NaHCO_3$ in turn, which contained dissolved H_2. Then the electrolyte underwent an intense shake to expel the hydrogen adsorbed on the electrode surface, followed by a H_2 supply again. As seen from **Figure. 6.2f**, a 0.2 V voltage change from -0.52 V to -0.72 V appears after altering electrolyte, which confirms our speculation. Later, the voltage was initiated by replacing the electrolyte into the original electrolyte of 1 M $NaHCO_3$ with saturated H_2. After which, the voltage increases at an alarming rate and returns to the initial voltage because of the vibration in H_2 concentration. Owing to the low partial pressure of H_2 (< 1 atm) in an exponential form, a minor change in H_2 concentration leads to dramatic changes in OCV, which is consistent with the aforementioned OCV equation. The foregoing results further confirm the need to ensure sufficient hydrogen concentration in the catholyte solution at the beginning. Otherwise, a false OCV would be produced. For this reason, H_2-saturated electrolytes were applied in all experiments if not otherwise stated.

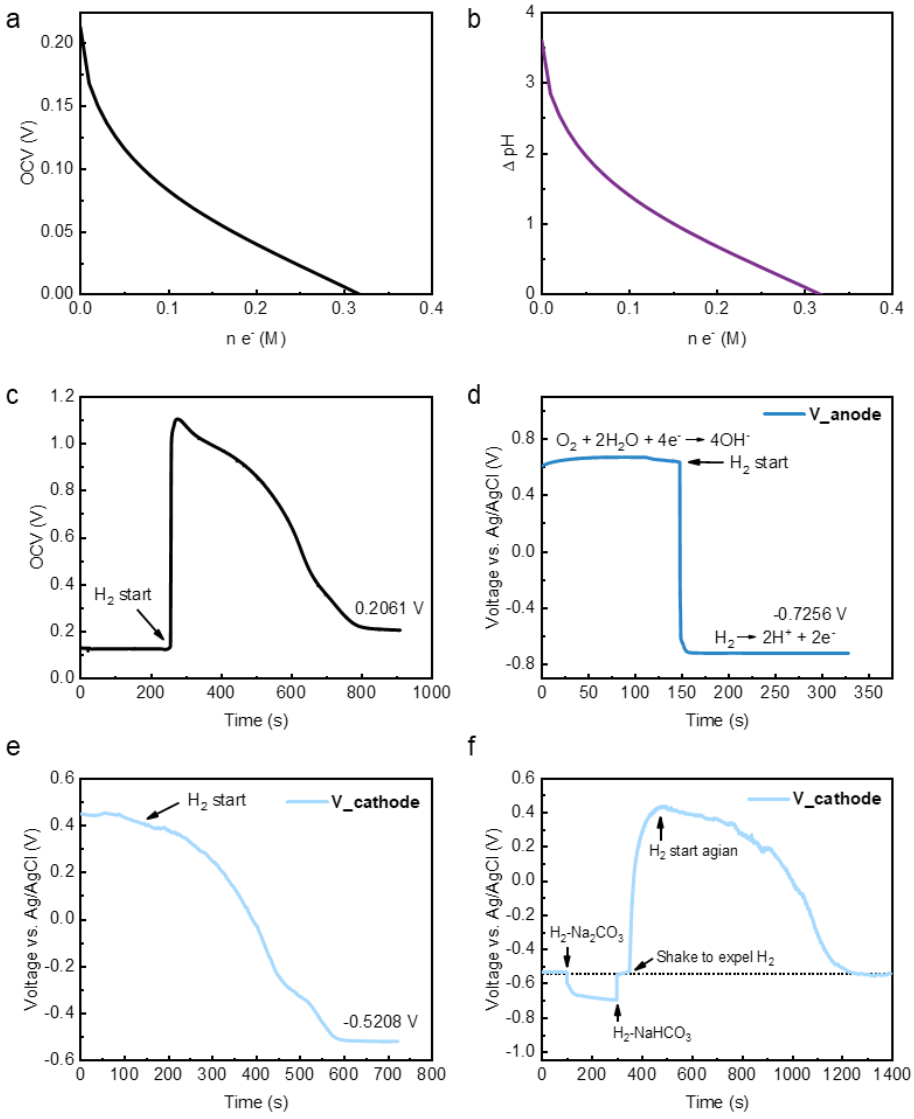

Figure 6.2. Open circuit voltage (OCV) change in pH-TRC. **a)** The OCV and **b)** pH difference change with electron transfer during discharging; **c)** OCV of cell, **d)** anode and **e)** cathode change by hydrogen supply; **f)** Voltage change with electrolyte state.

6.4 Working Characteristics of PH-TRC

After investigating the OCV generation, the discharging ability of pH-TRC was evaluated in this section. To properly understand the working characteristics, the linear sweep voltammetry (LSV) experiments were conducted in a single cell to study the discharging abilities of anode and cathode. LSV results of cathode and anode are shown in **Figure. 6.3a** and **Figure. 6.3b** separately, where dashed line represents initial OCV. In **Figure. 6.3a**, it is noticeable that two plateaus perform H_2 and OH^- diffusion dominated process as the voltage shifts negatively. Due to the low OCV, the cathode potential cannot be shifted to -0.8 V, thus the discharging process in cathode is unlikely to be controlled by OH^- diffusion. Regarding to the anode, the discharging process is much more complicated, as it involves complicated H-adsorption, which is a cause for fluctuations existing in LSV curve of the cathode.[130] Curves relating overpotential to *lg j* (anode and cathode) are given in **Figure. 6.3c**. The power density limit can be drawn by comparing current densities of anode and cathode under a same absolute value of overpotential, respectively. Given an overall OCV of 0.2 V, the current density of cathode is 5 times higher than that of anode within an overpotential range of 0 to 0.2 V. That means it is easier to reach cathode maximum current density than anode maximum current density. Briefly, it can be concluded that the power density is limited by anode. That is not only owing to the relatively complicated H-adsorption in anode, but also related to the substrate material of the electrode, since cathode of hydrophilic carbon cloth

provide larger reaction area than that of anode with a hydrophobic carbon paper substrate. A pH-TRC generates a peak power density of 5.296 W m^{-2} in **Figure. 6.3d**, which satisfies the practical power requirements of devices in general. As a proof-of-concept, four cells (each electrode surface of 10×10 cm) connected in parallel are capable of powering a smart phone and a LED array as demonstrated in **Figure. 6.3e** and **Figure. 6.3f** respectively. The demonstrations were conducted under a gas flow rate of 5 mL min^{-1} and an electrolyte flow rate of 40 mL min^{-1}. Two shared reservoirs to store anolyte and catholyte, respectively, allow the circulation and further regeneration of flowing electrolyte. A booster circuit was applied to adjust the output voltage without changing the absolute power output.

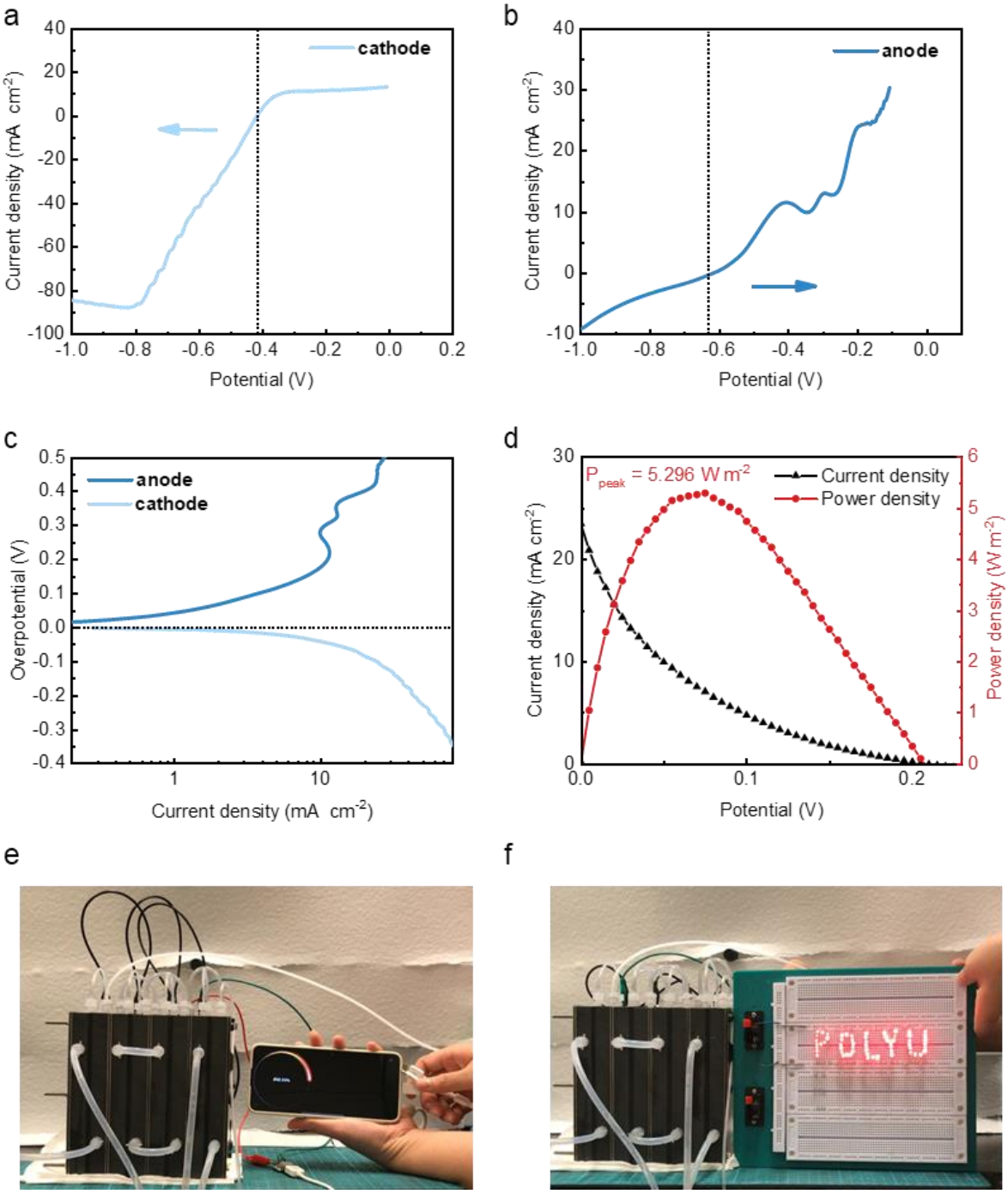

Figure 6.3. Results in power. **a-c)** LSV results of anode and cathode at sweep speed of 5 mV s^{-1}; **d)** Power density of a single cell pH-TRC (electrolyte flow rate: 40 mL min-1, gas flow rate: 5 mL min-1); **e-f)** Demonstrations of pH-TRC powering a smart phone and LED array.

6.5 System Stability and Effect of Operation Temperature

The total energy of pH-TRC is directly related to the electrolyte volume. Firstly, electricity production by a single cell was examined with 1.2 mL of still anolyte and 2 L of flowing catholyte ($V_{anolyte} << V_{catholyte}$). **Figure. 6.4a** shows the discharging process in stages under the current from 10 mA to 1 mA, which provided a long-standing discharging time of over 21000 of seconds with a capacity of 15.53 mA h. In this case, the amount of catholyte is infinite enough to accommodate the transferred sodium ions, the resultant anolyte and catholyte will both be pure $NaHCO_3$. **Figure. 6.4b** gives a proof of equal pH values (~8.5) of anolyte (left hand) and catholyte (right hand) by precise pH strips (5.5 - 9.0) after discharging. That implies 0.5 M electrons transferred in the case of **Figure. 6.4a**. Accordingly, a theoretical capacity of 16 mA h can be determined in this case, closely approaching our experimental result (15.53 mA h). On the other hand, if the same volume of anolyte and catholyte ($V_{anolyte} \approx V_{catholyte}$) are provided, the resultant products will be a mixture of Na_2CO_3 and $NaHCO_3$. **Figure. 6.4c** plots the pH change trends of anolyte and catholyte with a same volume in discharging process. If the cation effect on pH is carefully taken into account, the transferred electrons are estimated to be 0.3 M. To further illustrate this point, a discharging experiment with the same 50 mL of electrolytes was conducted (**Figure. 6.4d**). Consequently, electricity of 0.2046 A h was generated within an extremely appealing long discharging period of over 170 thousand of seconds. The corresponding energy

density of anolyte was 4.092 Ah m^{-3} ($V_{anolyte} \approx V_{catholyte}$) lower than 13.333 Ah m^{-3} ($V_{anolyte} << V_{catholyte}$) in the first case (**Figure. 6.4e**) as a result of incomplete conversion from Na_2CO_3 to $NaHCO_3$, which follows the prediction.

As our previous work suggested that increasing operating temperature during discharging might be beneficial, power densities at different temperatures were evaluated, where the peak power densities and a discharging curve at 50℃ were given in **Figure. 6.4e** and **Figure. 6.4g**, respectively. The power densities at higher temperatures are evidentially higher than those at lower temperatures. However, the energy density decreased under higher temperature. A single cell at 50℃ provides only 60% capacity of that at 25 ℃, suggesting the opposite effects of temperature on power density and capacity. A potential reason could be the electrolyte decomposition at higher temperature during discharging, while the consequently volatilized CO_2 reduces pH differences and thereby causing capacity loss. To confirm this speculation, the produced gas catholyte was collected and compared with standard H_2 and CO_2. The gas chromatography results (**Figure. 6.4h**) evidently showed that the produced gas was a mixture of H_2 and CO_2. Therefore, a higher operation temperature is not favored in the long run.

However, that doesn't mean no electrolyte decomposition occurs at room temperature. Even though considering the aforementioned differences in transferred electrons in cases of **Figure. 6.4a** and **Figure. 6.4d**, the energy density shown in **Figure.**

6.4a is still twice of that in **Figure. 6.4b**. This result can be attributed to the difference in discharging time, where little decomposition occurred in a shorter discharging time.

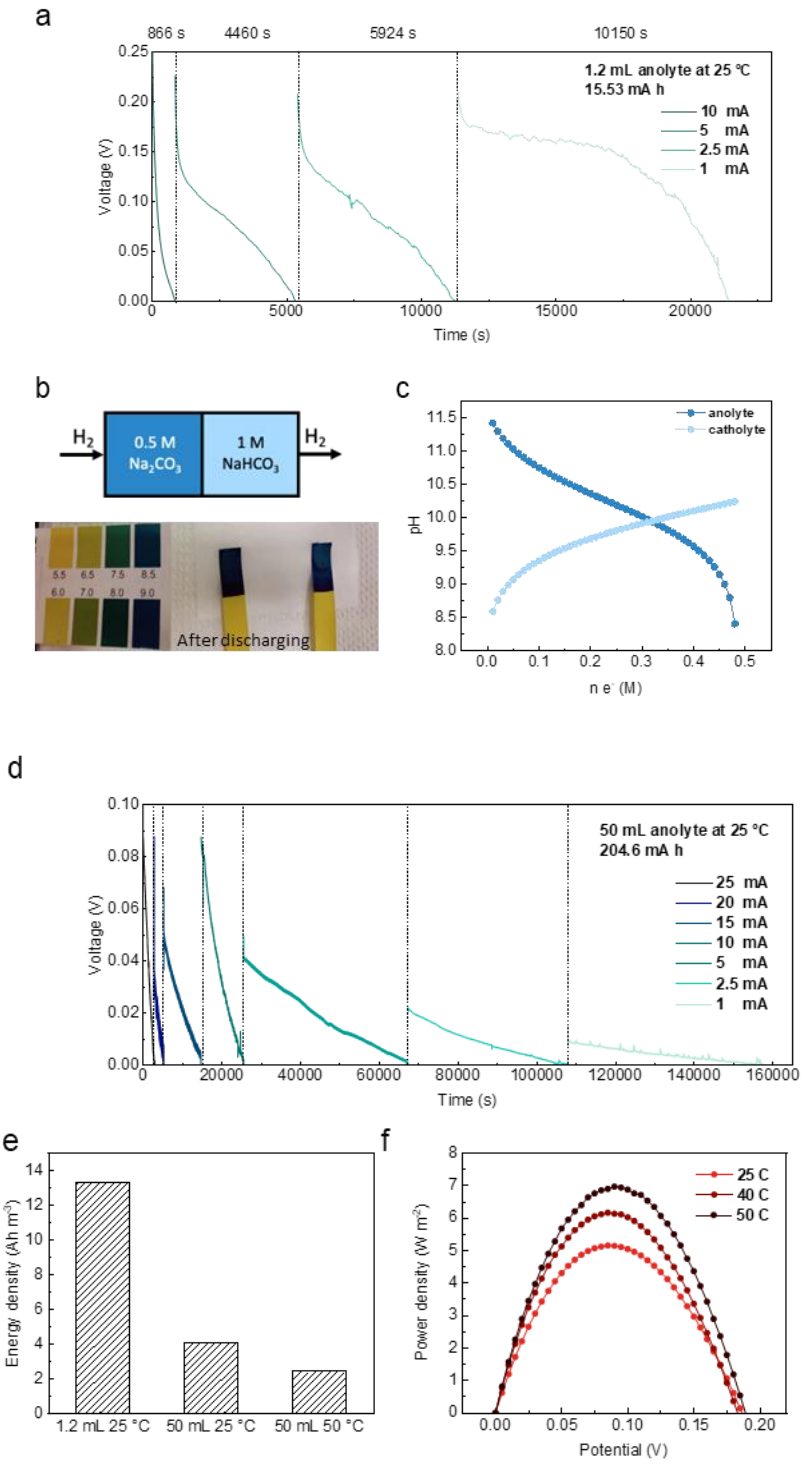

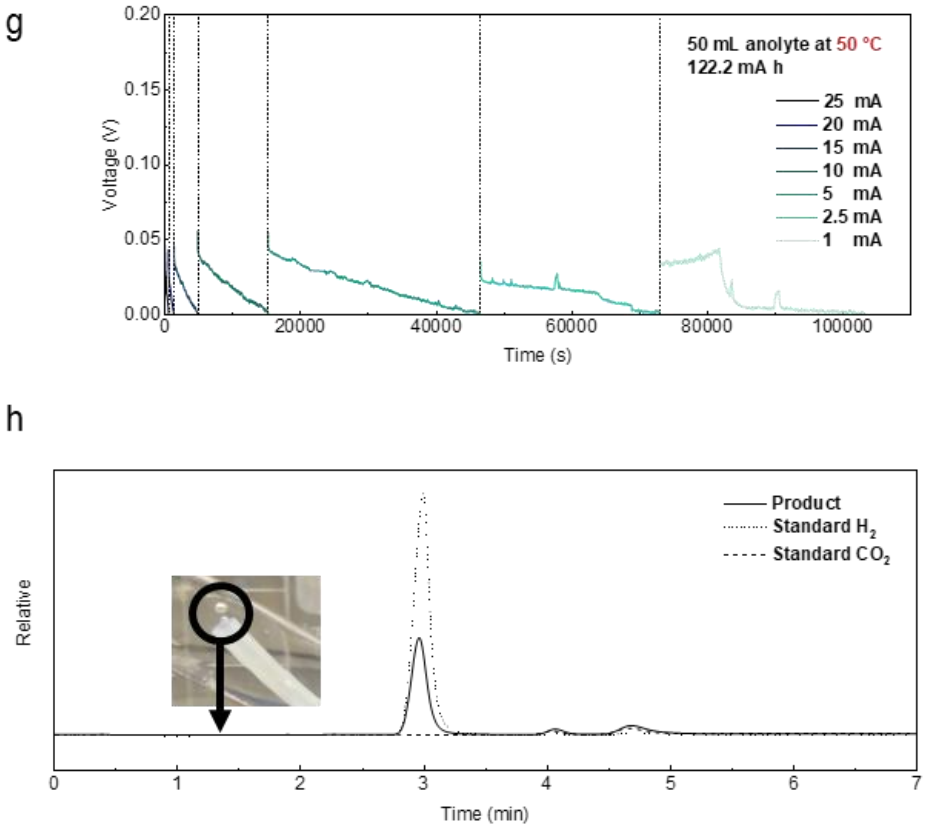

Figure 6.4. Discharging performance at room temperature and higher temperature. **a)** Discharging curve with 1.2 mL anolyte and 2 L catholyte at room temperature; **b)** Mechanism of pH value change of electrolytes during discharging, and comparison of anolyte and catholyte after long-time discharging; **c)** Calculated pH value change of electrolytes during discharging; **d)** Discharging curve with 50 mL anolyte and 50 mL catholyte at room temperature; **e)** Comparison of energy density with different electrolyte volume and temperature; **f)** Power densities with different temperatures; **g)** A discharging curve with equal volume of 50 mL of electrolytes at 50 Celsius; **h)** Gas chromatography curve of discharging product from catholyte.

6.6 Effect of Flow Rate and Supporting Electrolyte

To evaluate the effect of flow rate on power density, a comprehensive mathematical model was developed to simulate the transport and electrochemical process in a pH-TRC.

At first, the electrolytes follow the mass balance and charge balance. Given the concentrations of Na^+ and CO_3^{2-} or HCO_3^-, pH values can be calculated by these governing equations.

$$Mass\ balance: [Na^+] = [HCO_3^-] + [CO_3^{2-}] + [H_2CO_3] \quad (89)$$

$$Charge\ balance: [Na^+] + [H^+] = [HCO_3^-] + 2[CO_3^{2-}] + [OH^-] \quad (90)$$

Secondly, electrochemical reactions follow Butler-Volmer equation which depicts the relationship between current density and overpotential.

$$j = j_0 \left(\exp\left(\frac{\alpha F \theta}{RT}\right) - \exp\left(\frac{-\alpha F \theta}{RT}\right) \right) \quad (91)$$

In this equation, j is current density, j_0 is exchange current density corresponding to anode or cathode, α is the charge transfer coefficient, θ is the overpotential, R, T, F are standard gas constant, temperature, Faraday constant, respectively. j represents a current density on a certain electrode, so j_0, α, η should strictly follow the properties of the electrodes themselves. That means, when j_a (current density of anode) is calculated, j_0, α, η are all correspond to anode.

Thirdly, to maintain the constant power output, the transport of the oxidized and reduced species also needs to reach a steady state. The resultant ion flux should consider the impact of

diffusion, migration, thermal-diffusion, and convection, so the mass transport equation is given below:

$$\vec{N}_{\mathrm{i}} = -D_{\mathrm{i}}\nabla C_{\mathrm{i}} - Z_{\mathrm{i}}u_{\mathrm{i}}FC_{\mathrm{i}}\nabla\phi + C_{\mathrm{i}}\vec{u} \tag{92}$$

where $\vec{N}_{\mathrm{i}}$ is the ion flux density, composed of reaction-ion flux density and counter-ion flux density, D_{i},C_{i}, Z_{i}, u_{i} and Q_{i} are the diffusion coefficient, concentration, number of charges, ion mobility and heat of ion transport of a certain ion species, ϕ is the electrostatic potential, $\vec{u}$ is bulk vector velocity. The terms $-D_{\mathrm{i}}\nabla C_{\mathrm{i}}$, $-Z_{\mathrm{i}}u_{\mathrm{i}}FC_{\mathrm{i}}\nabla\phi$and $C_{\mathrm{i}}\vec{u}$ represent the effects by the diffusion, migration and convection, respectively. To obey the Nernst-Einstein relationship, the ion flux can be also written as below.

$$\vec{u} = \frac{D_{\mathrm{i}}FZ_{\mathrm{i}}}{RT} \tag{93}$$

Meanwhile, to satisfy the electrical neutrality condition $\sum Z_{\mathrm{i}}C_{\mathrm{i}} = 0$, ion flux can be related to current density.

$$j = F\sum_i \left(-Z_{\mathrm{i}}D_{\mathrm{i}}\nabla C_{\mathrm{i}} - Z_i^2u_{\mathrm{i}}FC_{\mathrm{i}}\nabla\phi - \frac{Z_{\mathrm{i}}Q_{\mathrm{i}}}{RT^2}D_{\mathrm{i}}C_{\mathrm{i}}\nabla T\right)\cdot\vec{n} + F\sum_i Z_{\mathrm{i}}C_{\mathrm{i}}\vec{u}\cdot\vec{n} \tag{94}$$

$\vec{n}$ is a normal unit vector perpendicular to the electrode, and the divergence of ion flux density equals to zero ($\nabla\cdot\vec{N}_{\mathrm{i}} = 0$) if the system reaches a steady state.

Lastly, for steady flow of compressible gas, the hydrogen gas flow motion in gas channel can be described by Navier–Stokes equation. Therefore, the flow field follows the governing equation below.

$$\rho(\vec{u}\cdot\nabla\vec{u}) = -\nabla p + \nabla\cdot\left(\mu(\nabla\vec{u} + (\nabla\vec{u})^T) - \frac{2}{3}\mu(\nabla\cdot\vec{u})\right) - \frac{\varepsilon v\vec{u}}{K} \tag{95}$$

In this equation, p is the pressure, ρ is the density, μ is dynamic viscosity, ε is the porosity of the porous electrode, and $\vec{I}$,and K is the coefficient of permeability. The last term in the right side is the Darcy's term to describe the momentum transport of flow in porous media. Continuity equations are solved simultaneously to satisfy Navier–Stokes equation.

$$\frac{\partial \rho}{\partial t} + \nabla \cdot (\rho \vec{u}) = 0 \tag{96}$$

Regarding to the incompressible stable flowing electrolytes, the Navier–Stokes equation is given below.

$$\rho(\vec{u} \cdot \nabla \vec{u}) = -\nabla p + \nabla \cdot \left(\mu(\nabla \vec{u} + (\nabla \vec{u})^T)\right) \tag{97}$$

To solve the equations, the parameters are calculated with the values given in **Table 6.3.**

Table 6.3. Parameters used in this model.

Parameters [units]	Value
Cell height [mm]	20
Gas channel thickness [mm]	1
Carbon paper thickness [mm]	0.2
Electrolyte channel thickness [mm]	1
Membrane thickness [mm]	0.1
Anode exchange current density [A m^{-2}]	22.387
Cathode exchange current density [A m^{-2}]	158.49
Density of hydrogen [kg m^{-3}]	0.084
Viscosity of hydrogen [Pa s]	8.8×10^{-6}
Macroscopic porosity between agglomerates [-]	0.4

Gas diffusion layer permeability [m^2]	1×10^{-13}
Membrane proton concentration [mol m^{-3}]	1990
Density of anolyte [kg m^{-3}]	1000
Viscosity of anolyte [Pa s]	0.001
Conductivity of anolyte [S m^{-1}]	29.705
Density of catholyte [kg m^{-3}]	1000
Viscosity of catholyte [Pa s]	0.001
Conductivity of catholyte [S m^{-1}]	17
Density of carbon paper [kg m^{-3}]	1.31
Conductivity of membrane [S m^{-1}]	11

The model was validated by comparing the experimental and computational peak power density in **Figure. 6.5a**. It shows a good agreement between the simulation (4.953 W m^{-2}) and experimental data (5.296 W m^{-2}). A minor shifting is due to the acceptable errors from calculation in experimental exchange current density. After model validation, parametric simulations were conducted to understand the effects of various operational parameters on pH-TRC performance. **Figure. 6.5b** and **Figure. 6.5c** provide experimental and computational power densities under various gas flow rates and electrolyte flow rates (assuming equal flow rates of anolyte and catholyte) respectively. Both experimental and computational power densities stabilize at approximately 5 W m^{-2} in **Figure. 6.5b**, as those sufficient reactants are supplied in this condition regardless of flow rate.

However, the same is not true for different electrolyte flow rates. The computational power density increases significantly from 2.53 to 4.07 W m^{-2} within the flow rate of 0.1 to 10 mL min^{-1}, subsequently rises slowly to 5 W m^{-2}. The experimental results well fit the computational results, proving the pH-TRC experience two different dominant steps with an accelerating flow rate. They are mass transfer step at low flow rate and reaction kinetic step under sufficient mass transfer. When the reaction transitions from mass transfer to reaction rate controlled, there is a correspondingly noticeable change in current density. That well explained the curve trends in **Figure. 6.5c**.

As is obvious from previous discussion, electrolyte flow rate is an important factor affecting power density. Yet it would be negligent not to consider the auxiliary input power from pump. The pump powers are given in **Figure. 6.5d** with a pump efficiency of 5%, suggesting applicable flow rates in terms of different power density generated from a pH-TRC. The mean power densities were calculated from a typical discharging case in **Figure. 6.5d**. As a gradual decrease in power density in a continuous discharging process, a cascade strategy was developed to reduce additional input energy. That is, applying high flow rate at the beginning and switching to low flow rate gradually, which helps achieve a high relative efficiency of 22.595% in this case (related to an idea efficiency of 0.27%).

Interestingly, the peak power density seldomly changes by adjusting other parameters including diffusion coefficient in gas diffusion layer etc., except for

changing the exchange current density of anode (noting here $j_0 = nFk^\circ$, where j_0 is the exchange current density, k° is the standard rate constant, a larger exchange current density corresponds to a higher electrode activity). **Figure. 6.5e** shows a stable increase in power density with increasing exchange current density of anode. As noted previously, the power density is mainly limited by the anode. Therefore, optimizing the anode reaction kinetics could be more effective than structure design. This problem may potentially be improved in three ways: First, optimize the electrode catalytic materials. Since the catalytic sites of platinum are mainly on the Pt (111) surface, it may be possible to use the electrochemical method to deposit platinum on the electrode with more catalytic sites. Second, adjust the products. The cathodic reaction rate can be possibly increased by introducing precipitation reaction relative to CO_3^{2-}(enlarging the local reactant/product concentration difference). Third, optimize the reaction conditions. We have found the anode reaction favours a higher flow rate of the anolyte. This is because the fresh anolyte can neutralize the newly generated hydrogen ions. Therefore, a flowing regenerative electrolyte with a higher pH may be helpful.

In addition to the aforementioned parameters, power production with different concentrations of supporting electrolyte is also estimated in **Figure. 6.5f**. It is supposed that sodium sulfate was added into electrolyte to reduce the internal resistance without changing the pH values of electrolytes. However, an unexpected decrease in power density is found with supporting electrolyte in **Figure. 6.5f**. In view of these observations, it is quite likely that anion adsorption at platinum electrode surfaces obstructs

HOR/HER reactions, which has been proved in references[131–134]. It is worth mentioning that, considering a higher concentration of sodium bicarbonate solution produces a larger pH difference between the anolyte and catholyte, additionally, less amount of water needs to be heated given the same amount of reactants thereby reducing the heat loss, higher concentrations are favored in this system design. Therefore, there is an optimal concentration choice limited by the solubility of both Na_2CO_3 and $NaHCO_3$. The constant concentrations of Na_2CO_3 and $NaHCO_3$ in this work is attributed to this.

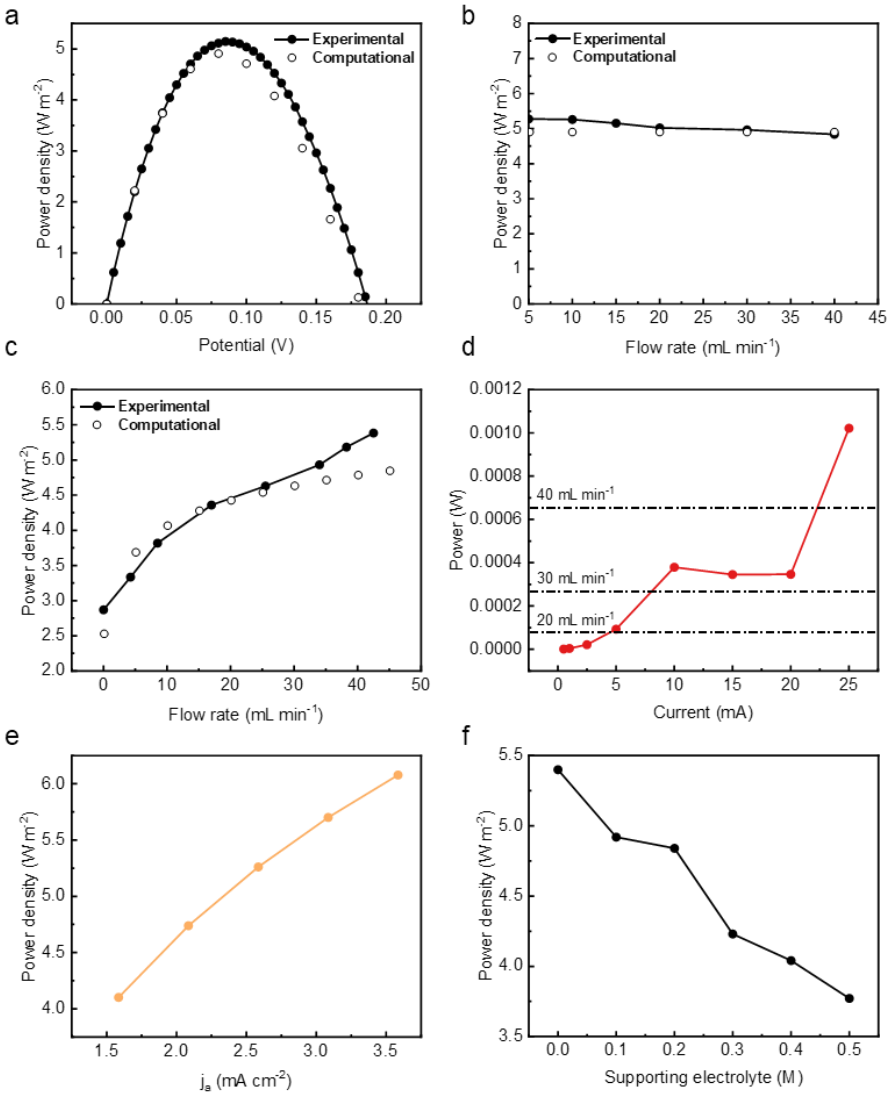

Figure 6.5. Effects of flow rate, supporting electrolyte and exchange current density of anode.

Comparison of experimental and computational power densities with **a)** various working voltage, **b)** different gas flow rate, and **c)** different electrolyte flow rate; **d)** Powers generated by a pH-TRC of 2×2 cm electrode area under different discharging current, where pumping powers under various electrolyte flow rate are plotted in dash line, suggesting a reasonable flow rate under a certain discharging current; **e)** Power density changes with exchange current densities of anode and **f)** a range of concentrations of supporting electrolyte.

6.7 PH-TRC Efficiency Calculation

The efficiency calculation is similar to that of TRCPC due to the structural similarity. Therefore, the analysis process follows the efficiency calculation in TRCPC system. Since the OCV is mainly attributed to the pH difference, assume the partial pressures of H_2 in anolyte and catholyte are the same, therefore, the OCV is determined as below.

$$E_n = (\varphi_{catholyte} - \varphi_{anolyte})_n = 0.0591 \Delta pH_n \quad (98)$$

As 0.32 M electrons are transferred in this system (**Figure. 6.4c**), the work is integrated as 1.426 kJ (1 L 0.5 M Na_2CO_3, 1 L 1 M $NaHCO_3$).

$$W_{e,ideal} = \int dW_e = \int FE_n dn = \int 0.0591 F \Delta pH_n dn = 1.426\ kJ. \quad (99)$$

In a single cell (50 mL catholyte/anolyte),

$$W_{output,ideal} = W_{e,ideal} = 71.3\ J. \quad (100)$$

The input energy E_{input} can be divided into two types. One is the auxiliary power W_p from pump to run the system, the other is the heat Q_{in} required to regenerate the electrolyte.

$$E_{input} = W_p + Q_{in} \quad (101)$$

a) auxiliary power

$$W_p = \frac{1}{2} m v^2 / \eta_{pump} \quad (102)$$

In this equation, m is the mass flow rate, v is the flow rate, and η_{pump} is the pump efficiency. The pump power can be neglected in the case of slow gas flow for the low flow rate and mass flow compared with liquid flow. The overall pump powers related to flow rates are given in **Table 6.4.**

Table 6.4. The overall pump powers (anolyte and catholyte) related to flow rates.

Flow rate mL min^{-1}	Tube radius mm	Mass rate kg s^{-1}	Flow rate m s^{-1}	η_{pump} %	Pump power W	Overall pump power W
1	1	1.80×10^{-5}	0.00531	5	5.07×10^{-9}	1.01×10^{-8}
10	1	1.80×10^{-4}	0.05308	5	5.07×10^{-6}	1.01×10^{-5}
20	1	3.60×10^{-4}	0.10616	5	4.06×10^{-5}	8.11×10^{-5}
30	1	5.40×10^{-4}	0.15924	5	1.37×10^{-4}	2.74×10^{-4}
40	1	7.20×10^{-4}	0.21231	5	3.25×10^{-4}	6.49×10^{-4}
50	1	9.00×10^{-4}	0.26539	5	6.339×10^{-4}	0.00127

Taking the cascade strategy, the overall pumping energy is 11.87181 J.

b) Input heat

The input heat can be divided into two parts. The first part Q_1 is the heat required for the decomposition reaction, which is also apply the enthalpy of 10.917 kJ mol^{-1} corresponding to the same regeneration reaction of $HCO_3^-(aq) \rightarrow \frac{1}{2}CO_3^{2-} + \frac{1}{2}\ CO_2(g) + \frac{1}{2}H_2O(l)$ in TRCPC. Therefore, for a single cell (50 mL catholyte/anolyte), Q_1 is 0.54868 kJ.

The second part Q_2 is the heat required to heat up the electrolyte from the working temperature (T_1=25°C) to the regeneration temperature (T_2=90°C). This temperature range has been evaluated in our previous work of TRCPC, and it proves the regeneration efficiency is more than 90% between cycles. The specific heat capacity of the solution is taken as 3.979 J K^{-1} g^{-1} which is similar to other sodium-based solutions. For a single cell, Q_2 is $m_{electrolyte}C_p(T_1 - T_2) \approx 25.864\ kJ$.

Thus, the input heat and input energy can be calculated as:

$$Q_{in} = Q_1 + Q_2 = 26.413\ kJ \tag{103}$$

$$E_{input} = W_p + Q_{in} \approx 26.424\ kJ. \tag{104}$$

We can see that W_p contributes little to the total energy needed in the ideal system which can be eliminated.

$$E_{input,ideal} = W_p + Q_{in} \approx Q_c \tag{105}$$

$$\eta_{exp} = \frac{W_{output,exp}}{E_{input}} = \frac{W_{e,exp}}{W_p + Q_{in}} = 0.06111\ \% \tag{106}$$

$$\eta_{ideal} = \frac{W_{output,ideal}}{E_{input}} = \frac{W_{e,ideal}}{W_p + Q_{in}} = 0.27046\ \% \tag{107}$$

$$\eta_{relative} = \frac{\eta_{exp}}{\eta_{ideal}} = 22.595\ \% \tag{108}$$

$$\eta_{Carnot} = \frac{\Delta T}{T_1 - T_2} = 17.906\ \% \tag{109}$$

$$\eta_{relative-to-Carnot} = \frac{\eta_{exp}}{\eta_{Carnot}} = 0.3\ \% \quad (110)$$

Besides, considering the engineering design of applying heat exchange to reduce heat loss, the Q_2 can be further reduced by introducing heat recuperation efficiency η_{HR}. Therefore, $Q_2 = (1 - \eta_{HR})C_p\Delta T$. Here, **Table 6.5** shows the results by applying heat exchange.

Table 6.5. The efficiency results by applying heat exchange.

η_{HX}	Q_2	E_{input}	η_{ideal}	η_{exp}	$\eta_{relative}$
0.00	25.86	26.41	0.27	0.06	22.59
0.50	12.93	13.48	0.53	0.12	22.59
0.70	3.88	4.43	1.61	0.36	22.59
1.00	0.00	0.55	12.99	2.94	22.59

6.8 Challenges and Future Perspectives of PH-TRC

Despite the high power density and long discharging time achieved, pH-TRCs are still at their early development stage with relatively low energy conversion efficiency. There are three key components/issues in a pH-TRC: pH-sensitive electrodes, thermally regenerative electrolytes, and a membrane to separate catholyte and anolyte. In this work, platinum-H_2/H^+ catalytic electrodes and $Na_2CO_3/NaHCO_3$ electrolytes were selected to replace previous consumable electrodes and to potentially integrate with CCS technologies, respectively. However, results show that the power was still limited by the relatively low anode reaction kinetics. Nevertheless, in addition to some of the improvements mentioned earlier, there are

plenty of choices of other existing redox or pseudocapacitive materials that can be used as pH-sensitive electrodes in pH-TRCs, such as manganese (IV) oxide/manganese (III) oxyhydroxide (MnO_2/MnOOH), nickel (II) hydroxide/nickel oxide hydroxide ($Ni(OH)_2$/NiOOH), nickel hexacyanoferrate (NiHCF), and polyaniline (PANI), etc. As to thermally regenerative electrolytes, potential candidates including potassium carbonate (K_2CO_3), trisodium phosphate (Na_3PO_4), and sodium acetate (CH_3COONa), *etc.*, may improve reaction kinetics by creating various pH environments Then, a proper membrane can be selected based on the electrode and electrolyte to facilitate desired ion transport. Apart from the variety of materials, cell/system structure also plays a vital role in approaching applications since the mass and heat transfer in a thermal regeneration process are mainly affected by the structure design. To sum up, as a new type of waste heat recovery platform, the current pH-TRC has plenty of room for optimization in the future from material to structural design.

6.9 Conclusions

A pH-sensitive thermally regenerative cell (pH-TRC) with circulating hydrogen was proposed and evaluated experimentally and theoretically in this work. The newly developed pH-TRC successfully converted low-grade heat into electricity with a peak power density of 5.296 W m^{-2}. More importantly, the discharging feasibility and cell scalability were experimentally confirmed with our optimization strategy of altering the electrode, changing the membrane, and applying flowing electrolytes. A proof-of-concept implement displayed an

incredibly long discharging time of hundreds of thousands of seconds, thousands of times higher than the reported discharging time in the literature [128]. Additionally, the OCV generation was analyzed based on electrode reactions. The system stability and effects of operation temperature, flow rate, and supporting electrolytes were evaluated and discussed. From these results, one can conclude that the electrolyte flow rate and reaction rate of the anode determines the discharging performance of pH-TRC, and supporting electrolytes might not be favored in electrolytes. Compared with structural improvement, electrodes with a higher rate constant are absolutely required. The significantly improved power output and discharging time paved the way for the practical application of waste-heat to electricity conversion.

CHAPTER 7 Conclusions and Outlook

7.1 Conclusions

In this thesis, the liquid-based electrochemical systems for low-grade heat harvesting were studied and summarized. In response to the existing problems in current heat-to-electricity technologies including low power densities and short lifespans, the prevalent TREC system was first studied from both thermodynamic theory and electrode design aspects due to its high efficiency and good stability. Moreover, the TREC system was optimized through a thoughtful analysis of thermopower. In addition to the traditional TREC systems, new systems of TRCPC and pH-TRC, which can also be classified as TREC, were proposed to enable board-scale implementations since traditional TREC systems were soon discovered to be insufficient for industry needs including the acceptable power density, long lifespan, stable power supply and absence of any pollution. TRCPC absorbed TRAB's concept but avoids the shortcomings of TRAB, and pH-TRC addressed the remained problems of TRCPC through a comprehensive consideration of the electrode design, reaction mechanism, system configuration, and working condition adjustments both computationally and experimentally. The research process is illustrated in the **Figure. 7.1** below. The solid-line boxes in the leftmost column depict the characteristics of each system, while the dotted-line boxes in the middle column summarize the shortcomings of each approach. The purple boxes in the rightmost column showcase the innovative aspects and landmark results of each system.

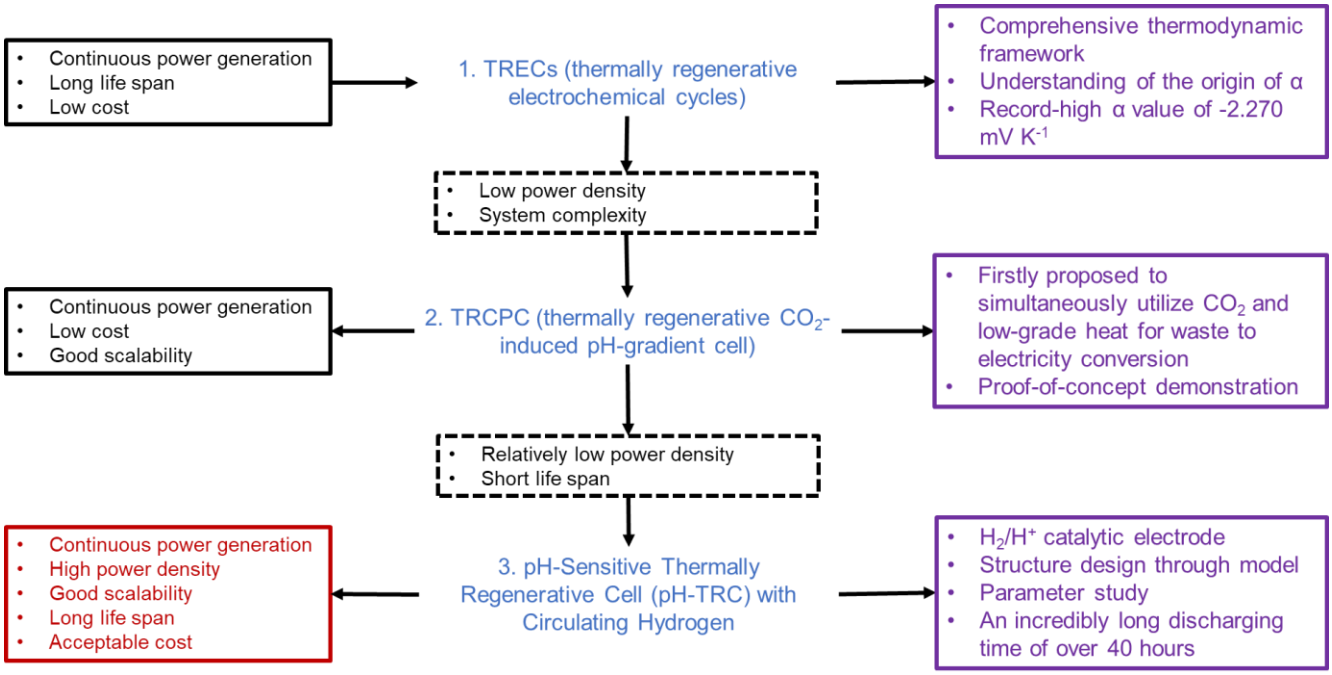

Figure 7.1. Research overview of these three works.

First, to increase the power density and efficiency, a comprehensive thermodynamic framework was proposed thereby advancing the understanding of the origin of α and electrochemical potential, which theoretically explained the deviation of thermopower change from linearity. In this work, the TREC with NiHCF cathode and Zn anode achieves a markedly high thermopower (α) of -1.575 mV K^{-1} and a heat-to-electricity efficiency of 2.41% at the temperature difference of 30 ℃ (equivalent to 25.15% of Carnot efficiency), surpassing all the existing TREC systems. For the first time, the mixed membranes with mixed pH electrolytes are introduced into the TREC systems to boost α *to* a record-high value of -2.270 mV K^{-1}.

Second, a thermally regenerative CO_2-induced pH-gradient cell (TRCPC) was proposed to simultaneously utilize CO_2 and low-grade heat for waste-to-electricity conversion. CO_2 is absorbed in one side of the symmetric electrolyte and causes a change in the pH of the cell to

induce voltage generation. After discharging, the system can be regenerated using low-grade heat while the CO_2 can then be stored and transported. Electrochemical experiments as well as materials characterizations were conducted to confirm the feasibility of the scheme. OCV was established through a pH difference in the membrane-separated electrolyte and current was provided via pseudocapacitance-behavior of $MnOOH/MnO_2$ electrode in Na_2CO_3 electrolyte. The TRCPC achieved a peak power density of 0.578 W m^{-2}. A mini proof-of-concept demonstration proved the current generated by TRCPC flowed through the resistor.

Third, an advanced pH-TRC with circulating hydrogen was improved by replacing the consumable electrode with H_2/H^+ catalytic electrode, rationally optimizing the cell design by changing the membrane, and applying flowing electrolytes. Between the H_2/H^+ catalytic electrodes, we have flowing anolyte and catholyte with different various pH values, which can be neutralized through discharging reactions and then thermally regenerated to reset the initial state. With this new design, a favorable peak power density of 5.296 W m^{-2} was obtained. More importantly, an incredibly long discharging time of over 40 hours enables the powering of a smartphone in comparison to only hundreds-of-seconds discharging time of previous TRC. So far, the performance of the advanced pH-TRC has achieved the objectives we set at the outset.

7.2 Outlook

This thesis proposed three continuously optimized liquid-based electrochemical systems including TREC, TRCPC, and pH-TRC for low-grade heat harvesting. After continuous

optimization from TREC to pH-TRC, the resultant pH-TRC shows great potential for industrial implementation due to its high power density and continuous discharge capability. To some extent, we have achieved the objectives but there remained considerable scope for improvement in terms of the balance of efficiency and power density.

With regards to traditional TREC, a higher thermopower is required needed. In our work, the record thermopower of -2.270 mV K^{-1} exceeds other works. Nevertheless, thermopower derived from single reaction entropy change does not gratify practical application. Assume a TREC with this record thermopower is applied with the temperature difference between room temperature (25℃) to the boiling temperature of a liquid system, the maximum voltage is only 0.148 V. To address this issue, the future research aspect is to combine different entropies in a system to promote the thermopower value, such as entropy changes from phase transformation and ion diffusion. Besides, considering the electrode material itself in a TREC involves in reaction at both low and high temperatures, electrode stability needs to be considered seriously and carefully. The sluggish kinetics at a low temperature and dissolution or swelling phenomenon at a high temperature hinder broadening operation temperature window.

For TRCPC and pH-TRC, the key issues at hand are slow kinetics of the anode and relatively low efficiency. Adjusting working conditions like increasing the flow rate of anolyte treats the symptoms of limited current density but the root cause is still the slow kinetics of the anode. A practical approach is to increase the Pt loading on the surface of the anode, or rationally design the reaction by introducing additional products thereby accelerating the catalytic reaction. In terms of efficiency, heat consumes the most significant part of input

energy. Especially for warming up the system during the regeneration process, water components absorb a large percentage of heat which is irrelevant to the intrinsic reaction, bringing a huge energy loss. Extra heat exchanging system supply is a good idea but is limited by recuperation efficiency. Another research direction is to lower unnecessary heat consumption, such as creating a hybrid electrolyte system with both water and organic components, which provide a reaction environment and low heat compacity, respectively.

REFERENCES

1. Lawrence Livermore National Laboratory. Esitmated U.S. Energy Use in 2019: 100.2 Quads. Preprint at https:// https://flowcharts.llnl.gov/commodities/energy (2019).

2. Haddad, C., Périlhon, C., Danlos, A., François, M. X. & Descombes, G. Some efficient solutions to recover low and medium waste heat: Competitiveness of the thermoacoustic technology. *Energy Procedia* **50**, 1056–1069 (2014).

3. Jouhara, H. *et al.* Waste heat recovery technologies and applications. *Thermal Science and Engineering Progress* **6**, 268–289 (2018).

4. Simeone, A., Luo, Y., Woolley, E., Rahimifard, S. & Boër, C. A decision support system for waste heat recovery in manufacturing. *CIRP Annals - Manufacturing Technology* **65**, 21–24 (2016).

5. Jin Bae, E., Hun Kang, Y., Jang, K. S. & Yun Cho, S. Enhancement of Thermoelectric Properties of PEDOT:PSS and Tellurium-PEDOT:PSS Hybrid Composites by Simple Chemical Treatment. *Scientific Reports* **6**, 1–10 (2016).

6. Saxena, N. *et al.* Ionic Liquids as Post-Treatment Agents for Simultaneous Improvement of Seebeck Coefficient and Electrical Conductivity in PEDOT:PSS Films. *ACS Applied Materials and Interfaces* **11**, 8060–8071 (2019).

7. Fan, Z., Du, D., Guan, X. & Ouyang, J. Polymer films with ultrahigh thermoelectric properties arising from significant seebeck coefficient enhancement by ion accumulation on surface. *Nano Energy* **51**, 481–488 (2018).

8. Poletayev, A. D., McKay, I. S., Chueh, W. C. & Majumdar, A. Continuous electrochemical heat engines. *Energy and Environmental Science* **11**, 2964–2971 (2018).

9. Bahk, J. H., Fang, H., Yazawa, K. & Shakouri, A. Flexible thermoelectric materials and device optimization for wearable energy harvesting. *Journal of Materials Chemistry C* **3**, 10362–10374 (2015).

10. Liang, J. *et al.* Flexible thermoelectrics: From silver chalcogenides to full-inorganic devices. *Energy and Environmental Science* **12**, 2983–2990 (2019).

11. Wang, W., Shu, G., Tian, H., Huo, D. & Zhu, X. A bimetallic thermally-regenerative ammonia-based flow battery for low-grade waste heat recovery. *Journal of Power Sources* **424**, 184–192 (2019).

12. Zeb, K. *et al.* A survey on waste heat recovery: Electric power generation and potential prospects within Pakistan. *Renewable and Sustainable Energy Reviews* **75**, 1142–1155 (2017).

13. Lu, X. & Morelli, D. T. Natural mineral tetrahedrite as a direct source of thermoelectric materials. *Physical Chemistry Chemical Physics* **15**, 5762–5766 (2013).

14. Davids, P. S. *et al.* Electrical power generation from moderate-temperature radiative thermal sources. *Science (New York, N.Y.)* **1345**, 1341–1345 (2020).

15. Salazar, P. F., Kumar, S. & Cola, B. A. Design and optimization of thermo-electrochemical cells. *Journal of Applied Electrochemistry* **44**, 325–336 (2014).

16. Cheng-Gong Han, Xin Qian，Qikai Li, Biao Deng, Yongbin Zhu, Zhijia Han, Wenqing Zhang, Weichao Wang, Shien-Ping Feng, Gang Chen, W. L. Giant thermopower of ionic gelatin near room temperature. *Science* **5045**, 1–13 (2020).

17. Kim, J. H. *et al.* Iron (II/III) perchlorate electrolytes for electrochemically harvesting low-grade thermal energy. *Scientific Reports* **9**, 1–8 (2019).

18. Duan, J. *et al.* Aqueous thermogavanic cells with a high Seebeck coefficient for low-grade heat harvest. *Nature Communications* **9**, 1–8 (2018).

19. Yu, B. *et al.* Thermosensitive crystallization–boosted liquid thermocells for low-grade heat harvesting. *Science* **346**, eabd6749 (2020).

20. Yang, P. *et al.* Wearable Thermocells Based on Gel Electrolytes for the Utilization of Body Heat. *Angewandte Chemie - International Edition* **55**, 12050–12053 (2016).

21. Jin, L., Greene, G. W., MacFarlane, D. R. & Pringle, J. M. Redox-Active Quasi-Solid-State Electrolytes for Thermal Energy Harvesting. *ACS Energy Letters* 5 (2016).

22. Lei, Z., Gao, W. & Wu, P. Double-network thermocells with extraordinary toughness and boosted power density for continuous heat harvesting. *Joule* **5**, 2211–2222 (2021).

23. Zhou, H., Yamada, T. & Kimizuka, N. Supramolecular Thermo-Electrochemical Cells: Enhanced Thermoelectric Performance by Host−Guest Complexation and Salt- Induced Crystallization. *J. Am. Chem. Soc.* 6 (2016).

24. Laux, E. *et al.* Aspects of Protonic Ionic Liquid as Electrolyte in Thermoelectric Generators. *Journal of Electronic Materials* **45**, 3383–3389 (2016).

25. Duan, J. P-N conversion in thermogalvanic cells induced by thermo-sensitive nanogels for body heat harvesting. *Nano Energy* 7 (2019).

26. High-thermopower polarized electrolytes enabled by methylcellulose for low-grade heat harvesting. *SCIENCE ADVANCES* 11 (2022).

27. Anari, E. H. B. *et al.* Substituted ferrocenes and iodine as synergistic thermoelectrochemical heat harvesting redox couples in ionic liquids. *Chemical Communications* **52**, 745–748 (2016).

28. Al-Masri, D., Dupont, M., Yunis, R., MacFarlane, D. R. & Pringle, J. M. The electrochemistry and performance of cobalt-based redox couples for thermoelectrochemical cells. *Electrochimica Acta* **269**, 714–723 (2018).

29. Taheri, A., MacFarlane, D. R., Pozo-Gonzalo, C. & Pringle, J. M. Application of a water-soluble cobalt redox couple in free-standing cellulose films for thermal energy harvesting. *Electrochimica Acta* **297**, 669–675 (2019).

30. Burmistrov, I., Kovyneva, N., Gorshkov, N., Gorokhovsky, A. & Durakov, A. Development of new electrode materials for thermo-electrochemical cells for waste heat harvesting. *Reinforced Plastics* **29**, 42–48 (2019).

31. Pennelli, G. Review of nanostructured devices for thermoelectric applications. *Beilstein Journal of Nanotechnology* **5**, 1268–1284 (2014).

32. Abraham, T. J. *et al.* Towards ionic liquid-based thermoelectrochemical cells for the harvesting of thermal energy. *Electrochimica Acta* **113**, 87–93 (2013).

33. Liu, W., Jie, Q., Kim, H. S. & Ren, Z. Current progress and future challenges in thermoelectric power generation: From materials to devices. *Acta Materialia* **87**, 357–376 (2015).

34. Hu, R. *et al.* Harvesting waste thermal energy using a carbon-nanotube-based thermo-electrochemical cell. *Nano Letters* **10**, 838–846 (2010).

35. Quickenden, T. I. A Review of Power Generation in Aqueous Thermogalvanic Cells. *Journal of The Electrochemical Society* **142**, 3985 (1995).

36. Zhang, L. *et al.* High Power Density Electrochemical Thermocells for Inexpensively Harvesting Low-Grade Thermal Energy. *Advanced Materials* **29**, 1–7 (2017).

37. Abraham, T. J., MacFarlane, D. R. & Pringle, J. M. Seebeck coefficients in ionic liquids -prospects for thermo-electrochemical cells. *Chemical Communications* **47**, 6260–6262 (2011).

38. Sosnowska, A. *et al.* Towards the Application of Structure–Property Relationship Modeling in Materials Science: Predicting the Seebeck Coefficient for Ionic Liquid/Redox Couple Systems. *ChemPhysChem* 1591–1600 (2016) doi:10.1002/cphc.201600080.

39. He, J., Al-Masri, D., MacFarlane, D. R. & Pringle, J. M. Temperature dependence of the electrode potential of a cobalt-based redox couple in ionic liquid electrolytes for thermal energy harvesting. *Faraday Discussions* **190**, 205–218 (2016).

40. Kang, T. J. *et al.* Electrical power from nanotube and graphene electrochemical thermal energy harvesters. *Advanced Functional Materials* **22**, 477–489 (2012).

41. Huang, B. *et al.* Non-covalent interactions in electrochemical reactions and implications in clean energy applications. *Physical Chemistry Chemical Physics* **20**, 15680–15686 (2018).

42. Lazar, M. A., Al-Masri, D., Macfarlane, D. R. & Pringle, J. M. Enhanced thermal energy harvesting performance of a cobalt redox couple in ionic liquid-solvent mixtures. *Physical Chemistry Chemical Physics* **18**, 1404–1410 (2016).

43. Kim, J. H. & Kang, T. J. Diffusion and Current Generation in Porous Electrodes for Thermo-electrochemical Cells. *ACS Applied Materials and Interfaces* **11**, 28894–28899 (2019).

44. Im, H. *et al.* High-efficiency electrochemical thermal energy harvester using carbon nanotube aerogel sheet electrodes. *Nature Communications* **7**, 1–9 (2016).

45. Romano, M. S. *et al.* Carbon nanotube-reduced graphene oxide composites for thermal energy harvesting applications. *Advanced Materials* **25**, 6602–6606 (2013).

46. Gao, C., Lee, S. W. & Yang, Y. Thermally Regenerative Electrochemical Cycle for Low-Grade Heat Harvesting. *ACS Energy Letters* **2**, 2326–2334 (2017).

47. Lee, S. W. *et al.* An electrochemical system for efficiently harvesting low-grade heat energy. *Nature Communications* **5**, 1–6 (2014).

48. Yang, Y. *et al.* Membrane-free battery for harvesting low-grade thermal energy. *Nano Letters* **14**, 6578–6583 (2014).

49. Chen, R., Deng, S., Xu, W. & Zhao, L. A graphic analysis method of electrochemical systems for low-grade heat harvesting from a perspective of thermodynamic cycles. *Energy* **191**, 116547 (2020).

50. Rahimi, M. *et al.* Emerging electrochemical and membrane-based systems to convert low-grade heat to electricity. *Energy and Environmental Science* **11**, 276–285 (2018).

51. Yang, Y. *et al.* Charging-free electrochemical system for harvesting low-grade thermal energy. *Proceedings of the National Academy of Sciences of the United States of America* **111**, 17011–17016 (2014).

52. Ding, Y. *et al.* Simultaneous energy harvesting and storage: Via solar-driven regenerative electrochemical cycles. *Energy and Environmental Science* **12**, 3370–3379 (2019).

53. Holeschovsky, U. B. Analysis of flooded flow fuel cells and thermogalvanic generators. (1994).

54. Romano, M. S. *et al.* Carbon Nanotube - Reduced Graphene Oxide Composites for Thermal Energy Harvesting Applications. *Adv. Mater.* **25**, 6602–6606 (2013).

55. Luo, X. *et al.* Power generation by coupling reverse electrodialysis and ammonium bicarbonate: Implication for recovery of waste heat. *Electrochemistry Communications* **19**, 25–28 (2012).

56. Kwon, K., Park, B. H., Kim, D. H. & Kim, D. Parametric study of reverse electrodialysis using ammonium bicarbonate solution for low-grade waste heat recovery. *Energy Conversion and Management* **103**, 104–110 (2015).

57. Zhu, X., He, W. & Logan, B. E. Influence of solution concentration and salt types on the performance of reverse electrodialysis cells. *Journal of Membrane Science* **494**, 154–160 (2015).

58. Kim, D. H., Park, B. H., Kwon, K., Li, L. & Kim, D. Modeling of power generation with thermolytic reverse electrodialysis for low-grade waste heat recovery. *Applied Energy* **189**, 201–210 (2017).

59. Altaee, A., Palenzuela, P., Zaragoza, G. & AlAnezi, A. A. Single and dual stage closed-loop pressure retarded osmosis for power generation: Feasibility and performance. *Applied Energy* **191**, 328–345 (2017).

60. Anastasio, D. D., Arena, J. T., Cole, E. A. & McCutcheon, J. R. Impact of temperature on power density in closed-loop pressure retarded osmosis for grid storage. *Journal of Membrane Science* **479**, 240–245 (2015).

61. Zhang, F., Liu, J., Yang, W. & Logan, B. E. A thermally regenerative ammonia-based battery for efficient harvesting of low-grade thermal energy as electrical power. *Energy and Environmental Science* **8**, 343–349 (2015).

62. Rahimi, M. *et al.* Improved electrical power production of thermally regenerative batteries using a poly(phenylene oxide) based anion exchange membrane. *Journal of Power Sources* **342**, 956–963 (2017).

63. Straub, A. P., Yip, N. Y., Lin, S., Lee, J. & Elimelech, M. Harvesting low-grade heat energy using thermo-osmotic vapour transport through nanoporous membranes. *Nature Energy* **1**, (2016).

64. Straub, A. P. & Elimelech, M. Energy Efficiency and Performance Limiting Effects in Thermo-Osmotic Energy Conversion from Low-Grade Heat. *Environmental Science and Technology* **51**, 12925–12937 (2017).

65. Zhang, X., Pan, Y., Cai, L., Zhao, Y. & Chen, J. Using electrochemical cycles to efficiently exploit the waste heat from a proton exchange membrane fuel cell. *Energy Conversion and Management* **144**, 217–223 (2017).

66. Zhang, X. *et al.* Exploiting the waste heat from an alkaline fuel cell via electrochemical cycles. *Energy* **142**, 983–990 (2018).

67. Long, R., Li, B., Liu, Z. & Liu, W. Performance analysis of a thermally regenerative electrochemical cycle for harvesting waste heat. *Energy* **87**, 463–469 (2015).

68. Shapira, B., Cohen, I., Penki, T. R., Avraham, E. & Aurbach, D. Energy extraction and water treatment in one system: The idea of using a desalination battery in a cooling tower. *Journal of Power Sources* **378**, 146–152 (2018).

69. Pasta, M., Wessells, C. D., Cui, Y. & La Mantia, F. A desalination battery. *Nano Letters* **12**, 839–843 (2012).

70. Ghaffour, N. *et al.* Renewable energy-driven innovative energy-efficient desalination technologies. *Applied Energy* **136**, 1155–1165 (2014).

71. Jiang, J. *et al.* A CoHCF system with enhanced energy conversion efficiency for low-grade heat harvesting. *Journal of Materials Chemistry A* **7**, 23862–23867 (2019).

72. Liu, Y., Gao, C., Sim, S., Kim, M. & Lee, S. W. Lithium Manganese Oxide in an Aqueous Electrochemical System for Low-Grade Thermal Energy Harvesting. *Chemistry of Materials* **31**, 4379–4384 (2019).

73. Linford, P. A., Xu, L., Huang, B., Shao-Horn, Y. & Thompson, C. V. Multi-cell thermogalvanic systems for harvesting energy from cyclic temperature changes. *Journal of Power Sources* **399**, 429–435 (2018).

74. Wang, Y., Cai, L., Peng, W., Zhou, Y. & Chen, J. Maximal continuous power output and parametric optimum design of an electrochemical system driven by low-grade heat. *Energy Conversion and Management* **138**, 156–161 (2017).

75. Guo, J. *et al.* Continuous power output criteria and optimum operation strategies of an upgraded thermally regenerative electrochemical cycles system. *Energy Conversion and Management* **180**, 654–664 (2019).

76. Li, L. *et al.* A stable vanadium redox-flow battery with high energy density for large-scale energy storage. *Advanced Energy Materials* **1**, 394–400 (2011).

77. Eapen, D. E., Choudhury, S. R. & Rengaswamy, R. Low-grade heat recovery for power generation through electrochemical route: Vanadium Redox Flow Battery, a case study. *Applied Surface Science* **474**, 262–268 (2019).

78. Reynard, D., Dennison, C. R., Battistel, A. & Girault, H. H. Efficiency improvement of an all-vanadium redox flow battery by harvesting low-grade heat. *Journal of Power Sources* **390**, 30–37 (2018).

79. Chow, T. T. A review on photovoltaic/thermal hybrid solar technology. *Applied Energy* **87**, 365–379 (2010).

80. Skyllas-Kazacos, M., Cao, L., Kazacos, M., Kausar, N. & Mousa, A. Vanadium Electrolyte Studies for the Vanadium Redox Battery—A Review. *ChemSusChem* **9**, 1521–1543 (2016).

81. Zhang, C., Zhao, T. S., Xu, Q., An, L. & Zhao, G. Effects of operating temperature on the performance of vanadium redox flow batteries. *Applied Energy* **155**, 349–353 (2015).

82. Zhang, H., Lek, D. G., Huang, S., Lee, Y. M. & Wang, Q. Efficient Low-Grade Heat Conversion and Storage with an Activity-Regulated Redox Flow Cell via a Thermally Regenerative Electrochemical Cycle. *Advanced Materials* **34**, 2202266 (2022).

83. Peljo, P., Lloyd, D., Doan, N., Majaneva, M. & Kontturi, K. Towards a thermally regenerative all-copper redox flow battery. *Physical Chemistry Chemical Physics* **16**, 2831–2835 (2014).

84. Rahimi, M., D'Angelo, A., Gorski, C. A., Scialdone, O. & Logan, B. E. Electrical power production from low-grade waste heat using a thermally regenerative ethylenediamine battery. *Journal of Power Sources* **351**, 45–50 (2017).

85. Rahimi, M., Kim, T., Gorski, C. A. & Logan, B. E. MWA thermally regenerative ammonia battery with carbon-silver electrodes for converting low-grade waste heat to electricity. *Journal of Power Sources* **373**, 95–102 (2018).

86. Zhu, X., Rahimi, M., Gorski, C. A. & Logan, B. A Thermally-Regenerative Ammonia-Based Flow Battery for Electrical Energy Recovery from Waste Heat. *ChemSusChem* **9**, 873–879 (2016).

87. Wang, W. *et al.* A bimetallic thermally regenerative ammonia-based battery for high power density and efficiently harvesting low-grade thermal energy. *Journal of Materials Chemistry A* **7**, 5991–6000 (2019).

88. Wang, W., Shu, G., Tian, H. & Zhu, X. A numerical model for a thermally-regenerative ammonia-based flow battery using for low-grade waste heat recovery. *Journal of Power Sources* **388**, 32–44 (2018).

89. Zhang, F., LaBarge, N., Yang, W., Liu, J. & Logan, B. E. Enhancing Low-Grade Thermal Energy Recovery in a Thermally Regenerative Ammonia Battery Using Elevated Temperatures. *ChemSusChem* **8**, 1043–1048 (2015).

90. Sales, B. B. *et al.* Extraction of Energy from Small Thermal Differences near Room Temperature Using Capacitive Membrane Technology. *Environmental Science and Technology Letters* **1**, 356–360 (2014).

91. Härtel, A., Janssen, M., Weingarth, D., Presser, V. & Van Roij, R. Heat-to-current conversion of low-grade heat from a thermocapacitive cycle by supercapacitors. *Energy and Environmental Science* **8**, 2396–2401 (2015).

92. Wang, X. *et al.* Direct thermal charging cell for converting low-grade heat to electricity. *Nature Communications* **10**, 1–8 (2019).

93. Phillip, W. A. Thermal-energy conversion: Under pressure. *Nature Energy* **1**, 10–11 (2016).

94. Xie, G. *et al.* Skin-Inspired Low-Grade Heat Energy Harvesting Using Directed Ionic Flow through Conical Nanochannels. *Advanced Energy Materials* **8**, 1–6 (2018).

95. Liu, G., Chen, T., Xu, J., Li, G. & Wang, K. Solar evaporation for simultaneous steam and power generation. *Journal of Materials Chemistry A* **8**, 513–531 (2020).

96. Cheng, Q. *et al.* Photorechargeable High Voltage Redox Battery Enabled by Ta3N5 and GaN/Si Dual-Photoelectrode. *Advanced Materials* **29**, 1–8 (2017).

97. Yang, Y. *et al.* Flexible hybrid energy cell for simultaneously harvesting thermal, mechanical, and solar energies. *ACS Nano* **7**, 785–790 (2013).

98. Gao, C. *et al.* Engineering the Electrochemical Temperature Coefficient for Efficient Low-Grade Heat Harvesting. *Adv. Funct. Mater.* **28**, 1803129 (2018).

99. Wang, Z. *et al.* Stability improvement of Prussian blue in nonacidic solutions via an electrochemical post-treatment method and the shape evolution of Prussian blue from nanospheres to nanocubes. *Analyst* **139**, 1127 (2014).

100. Zhong, C. *et al.* Decoupling electrolytes towards stable and high-energy rechargeable aqueous zinc–manganese dioxide batteries. *Nat Energy* **5**, 440–449 (2020).

101. Starzak, M. & Mathlouthi, M. Cluster composition of liquid water derived from laser-Raman spectra and molecular simulation data. *Food Chemistry* **82**, 3–22 (2003).

102. Water specific heat capacity as a function of temperature. https://syeilendrapramuditya.wordpress.com/tag/water-specific-heat-capacity/.

103. Ben Mabrouk, K., Kauffmann, T. H., Aroui, H. & Fontana, M. D. Raman study of cation effect on sulfate vibration modes in solid state and in aqueous solutions: Raman study of cation effect on sulfate vibration modes. *J. Raman Spectrosc.* **44**, 1603–1608 (2013).

104. Marcus, Y. Thermodynamics of ion hydration and its interpretation in terms of a common model. *Pure and Applied Chemistry* **59**, 1093–1101 (1987).

105. Chemical Design Institute of the Ministry of Petrochemical Industry. *Nitrogen Fertilizer Process Design Manual Physical and Chemical Data*. (Chemical Industry Press, 1977).

106. Water - Specific Heat. https://www.engineeringtoolbox.com/specific-heat-capacity-water-d_660.html.

107. Rumpf, B. & Maurer, G. Solubility of ammonia in aqueous solutions of sodium sulfate and ammonium sulfate at temperatures from 333.15 K to 433.15 K and pressures up to 3 MPa. *Ind. Eng. Chem. Res.* **32**, 1780–1789 (1993).

108. Majzlan, J. *et al.* Thermodynamic Properties and Phase Equilibria of the Secondary Copper Minerals Libethenite, Olivenite, Pseudomalachite, Kröhnkite, Cyanochroite, and Devilline. *Can Mineral* **53**, 937–960 (2015).

109. Water - Heat of Vaporization. *Engineering ToolBox* https://www.engineeringtoolbox.com/water-properties-d_1573.html.

110. Nikitina, V. A., Vassiliev, S. Y. & Stevenson, K. J. Metal-Ion Coupled Electron Transfer Kinetics in Intercalation-Based Transition Metal Oxides. *Adv. Energy Mater.* **10**, 1903933 (2020).

111. Ao, H. *et al.* Rechargeable aqueous hybrid ion batteries: developments and prospects. *J. Mater. Chem. A* **7**, 18708–18734 (2019).

112. Poletayev, A. D., McKay, I. S., Chueh, W. C. & Majumdar, A. Continuous electrochemical heat engines. *Energy Environ. Sci.* **11**, 2964–2971 (2018).

113. Wang, X. *et al.* Direct thermal charging cell for converting low-grade heat to electricity. *Nat Commun* **10**, 4151 (2019).

114. Rahimi, M. *et al.* Carbon Dioxide Capture Using an Electrochemically Driven Proton Concentration Process. *Cell Reports Physical Science* **1**, 100033 (2020).

115. Grimekis, D., Giannoulidis, S., Manou, K., Panopoulos, K. D. & Karellas, S. Experimental investigation of CO2 solubility and its absorption rate into promoted aqueous potassium carbonate solutions at elevated temperatures. *International Journal of Greenhouse Gas Control* **81**, 83–92 (2019).

116. Mumford, K. A. *et al.* Post-combustion Capture of CO_2: Results from the Solvent Absorption Capture Plant at Hazelwood Power Station Using Potassium Carbonate Solvent. *Energy Fuels* **26**, 138–146 (2012).

117. Kim, T., Logan, B. E. & Gorski, C. A. A pH-Gradient Flow Cell for Converting Waste CO_2 into Electricity. *Environ. Sci. Technol. Lett.* **4**, 49–53 (2017).

118. Center for global development. *CGD ranks CO2 emissions from power plants worldwide*. https://www.eurekalert.org/pub_releases/2007-11/cfgd-crc111207.php.

119. Kanoh, H., Tang, W., Makita, Y. & Ooi, K. Electrochemical Intercalation of Alkali-Metal Ions into Birnessite-Type Manganese Oxide in Aqueous Solution. *Langmuir* **13**, 6845–6849 (1997).

120. Marković, M. M. & Milonjić, S. K. Heat capacities of sodium carbonate-sodium bicarbonate aqueous solution mixtures. *Thermochimica Acta* **257**, 111–115 (1995).

121. Magalhães, M. C. F., Königsberger, E., May, P. M. & Hefter, G. Heat Capacities of Concentrated Aqueous Solutions of Sodium Sulfate, Sodium Carbonate, and Sodium Hydroxide at 25 °C. *J. Chem. Eng. Data* **47**, 590–598 (2002).

122. Yang, Y. *et al.* Membrane-Free Battery for Harvesting Low-Grade Thermal Energy. *Nano Lett.* **14**, 6578–6583 (2014).

123. Lee, S. W. *et al.* An electrochemical system for efficiently harvesting low-grade heat energy. *Nat Commun* **5**, 3942 (2014).

124. Cheng, C. *et al.* Insights into the Thermopower of Thermally Regenerative Electrochemical Cycle for Low-grade Heat Harvesting. *ACS Energy Lett.* 329–336 (2020) doi:10.1021/acsenergylett.0c02322.

125. Zhang, F., Liu, J., Yang, W. & Logan, B. E. A thermally regenerative ammonia-based battery for efficient harvesting of low-grade thermal energy as electrical power. *Energy Environ. Sci.* **8**, 343–349 (2015).

126. Wang, W. *et al.* A bimetallic thermally regenerative ammonia-based battery for high power density and efficiently harvesting low-grade thermal energy. *J. Mater. Chem. A* **7**, 5991–6000 (2019).

127. Zhu, X., Rahimi, M., Gorski, C. A. & Logan, B. A Thermally-Regenerative Ammonia-Based Flow Battery for Electrical Energy Recovery from Waste Heat. *ChemSusChem* **9**, 873–879 (2016).

128. Cheng, C. *et al.* Thermally Regenerative CO_2 -Induced pH-Gradient Cell for Waste-to-Energy Conversion. *ACS Energy Lett.* **6**, 3221–3227 (2021).

129. Shim, J.-G., Lee, D. W., Lee, J. H. & Kwak, N.-S. Experimental study on capture of carbon dioxide and production of sodium bicarbonate from sodium hydroxide. *Environmental Engineering Research* **21**, 297–303 (2016).

130. Liu, L., Liu, Y. & Liu, C. Enhancing the Understanding of Hydrogen Evolution and Oxidation Reactions on Pt(111) through Ab Initio Simulation of Electrode/Electrolyte Kinetics. *J. Am. Chem. Soc.* **142**, 4985–4989 (2020).

131. Nakata, K. *et al.* Surface-Enhanced Infrared Absorption Spectroscopic Studies of Adsorbed Nitrate, Nitric Oxide, and Related Compounds 2: Nitrate Ion Adsorption at a Platinum Electrode. *Langmuir* **24**, 4358–4363 (2008).

132. Cheng, R. & Shi, M. Sulfate-induced electrochemical instability in the transpassive region during the electrooxidation of Na2S on Pt. *J Solid State Electrochem* **23**, 1523–1531 (2019).

133. Dalbeck, R. & Vielstich, W. Ex situ analysis of sulfate adsorption on platinum via thermal desorption spectroscopy in ultra high vacuum. *Electrochimica Acta* **40**, 2687–2688 (1995).

134. Gossenberger, F., Juarez, F. & Groß, A. Sulfate, Bisulfate, and Hydrogen Co-adsorption on Pt(111) and Au(111) in an Electrochemical Environment. *Front. Chem.* **8**, 634 (2020).